Title
K~-PROTON INTERACTIONS NEAR 400 Mev/c

Permalink
https://escholarship.org/uc/item/3g267039

Author
Watson, Mason B.

Publication Date
1962-09-01

UCRL 10175

University of California

Ernest O. Lawrence Radiation Laboratory

K^--PROTON INTERACTIONS NEAR 400 MeV/c

Berkeley, California

TECHNICAL INFORMATION DIVISION

Lawrence Radiation Laboratory

Berkeley

Only Loan Cy Available

Assigned to INFORMATION DIVISION

Please return as soon as convenient we have only loan cy. of this

Route to	Noted
P. Bastien /	FEB 18 1963
L. Auerbach, request	APR 22 1963 ✓
S. Fung ✓	JUN 16 1964
J. Meisner	✓
J. Kadyk (request)	NOV 23 1966

Please return this document to the Information Division. Do not send it to the next person on the list.

Library & Documents

50-135

Please do not remove this page.

RL-254-1

UCRL-10175
UC-34 Physics
TID-4500 (17th Ed.)

Research and Development

UNIVERSITY OF CALIFORNIA

Lawrence Radiation Laboratory
Berkeley, California

Contract No. W-7405-eng-48

K^--PROTON INTERACTIONS NEAR 400 Mev/c

Mason B. Watson

(Ph. D. Thesis)

September 1962

K^--PROTON INTERACTIONS NEAR 400 Mev/c

Contents

Abstract v
I. Introduction 1

II. Experimental Procedure

- A. Beam 2
- B. Scanning 7
- C. Sketching and Measuring 11
- D. Event Reconstruction 11
- E. Remeasruements and Hand Analysis 11

III. Event Analysis

- A. τ Decays and Path Length 12
- B. Elastic Scattering; $K^- + p \rightarrow K^- + p$ 16
- C. $\Sigma^{\pm}$ Production; $K^- + p \rightarrow \Sigma^+ + \pi^-$; $\Sigma^- + \pi^+$ 26
- D. 0-Prong V Events; $K^- + p \rightarrow \overline{K}^0 + n$; $\Sigma^0 + \pi^0$; $\Lambda + \pi^0$; $\Lambda + \pi^0$; $\Lambda + \pi^0 + \pi^0$ 28
- E. 2-Prong V Events; $K^- + p \rightarrow \Lambda + \pi^+ + \pi^+$ 47

IV. Interpreting the Results

- A. Resonance Hypothesis 55
- B. The KPΣ Parity 69
- C. Parameter Determination by the Computer 71
- D. Discussion 82
  - 1. The Solutions 82
  - 2. Yang Ambiguities 88
  - 3. The $J = 5/2$ Possibility 90
  - 4. The Y_1^* Cusp Explanation 91

V. Acknowledgments 94

Appendices

- I. Distributions of χ^2 and the Pull Quantities for Event Reconstruction 95
- II. Equations for General Duke 102

References 104

K^--PROTON INTERACTIONS NEAR 400 Mev/c

Mason B. Watson

Lawrence Radiation Laboratory, University of California
Berkeley, California

September, 1962

ABSTRACT

Elastic and charge-exchange scattering as well as hyperon production by K^- mesons on protons are reported for a range of momenta near 400 Mev/c. Differential and total cross sections for all channels from 200 Mev/c to 513 Mev/c are examined. For $\Sigma^+\pi^-$, $\Sigma^0\pi^0$, and $\Lambda\pi^0$ production, polarization measurements are also available. A resonant state of mass 1520 Mev (390 Mev/c $\bar{K}$ momentum) was found with components $\bar{K}N$, $\Sigma\pi$, and $\Lambda\pi\pi$. The resonance is found to have a full width, Γ, of approximately 15 Mev, spin 3/2, isotopic spin 0, and parity that of the $\bar{K}N$ $D_{3/2}$ state. By use of the polarization arising from the resonant $D_{3/2}$- amplitude—s-wave interference the $KP\Sigma$ parity is determined to be odd. The data between 350 and 450 Mev/c are fitted to a model based on a Breit-Wigner resonant amplitude and zero-effective-range nonresonant amplitudes. Two solutions differing principally in the p waves are found. The s-wave parameters are found to agree quite well with the Humphrey-Ross values except for the relative phase in the $\Sigma\pi$ channel.

Table A. Summary. Cross sections for the different K^- momenta (in Mev/c) for $K^- + p$ reactions.

	Cross sections (mb)						
Reaction products	P_K = 293±42	350±31	387±30	392±30	390[a]±30	434±26	513±20
$K^- + p$	48.2±4.2	34.0±3.2	31.9±2.5	34.0±3.0	32.7±1.8	30.6±3.4	26.5±3.3
$K^0 + n$	8.0±1.2	5.1±1.1	8.1±1.0	10.0±1.0	8.8±0.7	6.0±1.2	3.6±0.6
$\Sigma^+ + \pi^-$	13.6±1.4	10.6±1.4	11.4±1.0	14.0±1.4	12.5±0.8	8.2±0.9	7.5±1.1
$\Sigma^- + \pi^+$	10.0±1.1	6.9±1.0	6.0±0.6	8.3±0.9	6.9±0.5	6.1±0.7	4.9±0.8
$\Sigma^0 + \pi^0$[b]	5.2±0.9	6.3±1.4	6.9±0.9	6.4±1.0	6.7±0.6	4.9±1.3	1.7±0.3
$\Lambda + \pi^0$	5.2±0.9	4.5±1.0	2.9±0.5	3.3±0.6	3.1±0.3	3.2±0.7	1.6±0.4
$\Lambda + \pi^0 + \pi^0$[c]	0.3±0.2	1.9±0.6	1.2±0.4	1.8±0.3	1.5±0.2	0.8±0.4	1.1±0.3
$\Lambda + \pi^+ + \pi^-$	0.15±0.10	0.9±0.3	1.2±0.3	2.4±0.4	1.6±0.2	1.5±0.4	2.0±0.4
$\Sigma^0 + \pi^+ + \pi^-$	0 ±0.02	0 ±0.09	0.08±0.05	0.06±0.06	0.07±0.06	0 ±0.08	0.3±0.15
$\Sigma^+ + \pi^- + \pi^0$	0 ±0.05	0.06±0.06	0.09±0.05	0.21±0.10	0.11±0.04	0.18±0.11	0.20±0.12
$\Sigma^- + \pi^+ + \pi^0$	0.05±0.05	0 ±0.06	0.03±0.03	0.17±0.09	0.12±0.05	0 ±0.06	0.14±0.10
Total	90.7±4.9	70.2±4.2	69.6±3.2	80.6±4.0	73.8±2.3	61.5±4.1	49.5±3.7
$(\Sigma\pi)_{I=0}$	15.6±2.7	18.9±4.2	20.7±2.7	19.2±3.0	20.1±1.8	14.7±3.9	5.1±0.9
$(\Sigma\pi)_{I=1}$	13.2±2.5	4.9±3.3	3.6±2.2	9.5±2.6	6.0±1.4	4.5±2.8	9.0±1.5
$\pi\lambda\!\!\!^{-}{}^2$	35.7	25.6	21.4	20.8	20.9	17.3	13.0

a. Combined runs 387 and 392 Mev/c.

b. Derived from $\sigma(\Sigma^0\pi^0) = \sigma(\Sigma^0\pi^0 + \Lambda\pi^0\pi^0) - \frac{1}{2}\sigma(\Lambda\pi^+\pi^-)$.

c. Derived from phase-space considerations; as they stand they violate charge independence when compared with $\Lambda\pi^+\pi^-$.

I. INTRODUCTION

Below 300 Mev/c, K^--proton interactions are strongly dominated by s waves. Above 300 Mev/c, higher partial waves begin to exhibit themselves in spectacular fashion. Previous to this experiment in 1959 about 140 interactions at 400 Mev/c in the Alvarez 15-inch liquid hydrogen bubble chamber were analyzed.[1] These interactions were mostly elastic scatterings in which a large $\cos^2\theta$ term was found in the angular distribution for the first time. Poor statistics prevented any conclusions about the other channels beyond their total cross sections. With this background and by use of the same Alvarez liquid hydrogen bubble chamber, a general exploratory experiment was carried out at the Bevatron beginning on October of 1960. A new highly enriched beam of K^- mesons was constructed which could produce K^- momenta from 0 to 850 Mev/c. Exposures to K^- laboratory momenta at about 300, 350, 400, 440, and 510 Mev/c form the source of the data to be presented here. In this energy region the interactions observed were

$$
\begin{aligned}
K^- + P &\to K^- + P, \\
&\to \bar{K}^0 + N, \\
&\to \Sigma^+ + \pi^- \text{ and } \Sigma^+ + \pi^- + \pi^0, \\
&\to \Sigma^- + \pi^+ \text{ and } \Sigma^- + \pi^+ + \pi^0, \\
&\to \Sigma^0 + \pi^0 \text{ and } \Sigma^0 + \pi^0 + \pi^0, \\
&\to \Lambda + \pi^0 \text{ and } \Lambda + \pi^0 + \pi^0, \\
&\to \Lambda + \pi^+ + \pi^-.
\end{aligned}
$$

Section II is devoted to a brief description of the experimental procedures characteristic of all interactions. Section III treats the problems and results associated with each of the channels individually, and in Section IV the picture as a whole is examined. It is shown that at a K^--proton center-of-mass energy of 1520 Mev (approx 390 Mev/c laboratory momentum) there exists a resonance with quantum numbers corresponding to the K^-p, $D_{3/2}$, $I = 0$ state. Furthermore, by using the existence of this state, a strong argument for odd $KP\Sigma$ relative parity results. The reader who is interested in results only should skip to Section III for the figures and captions, then, to all of Section IV.

II. EXPERIMENTAL PROCEDURE

A. Beam

As this report deals only with part of a larger experiment done under other conditions, the beam was not designed solely for the momentum intervals considered here. Flexibility was one of the chief considerations in design of the magnet system. This system has been discussed previously and is described only briefly here.[2]

The K^- mesons were obtained with the maximum-energy proton beam of the Bevatron striking a copper target. The beam was taken off the target in the forward direction at 0°, where the π^-/k^- ratio was approximately 500 to 1. Once the beam was outside the Bevatron magnet structure, the elements shown in Fig. 1 were employed to select a narrow momentum interval while separating the K^- from the π^- background.

To accomplish this separation two stages of electrostatic separation were required. Crossed electric and magnetic fields were adjusted so that the K^- mesons were undeflected while the π^- underwent a vertical deflection. The deflection of the π^- image at the first mass-resolving slit (S1) was about $\frac{1}{2}$ in. from the K^- image. At that point the K^- were directed through a 1/8×2-1/4-in. opening into the second stage while the π^- buried themselves in the lead walls of the slit. The success of this method depends critically on the separation of the π^- and K^- images, which is limited by the electric and magnetic fields obtainable in the separators.

This experiment was the first to utilize the heated-glass-cathode technique due to Dr. Joseph J. Murray. This enabled us to reach a 50% higher electric field gradient than was possible with previous separators. These cathodes are discussed in detail elsewhere.[3] During normal operation both of the 10-foot separators held 450 kv across parallel plates with a 2-in. gap, yielding a gradient of approximately 90 kv/cm. The two separators were identical.

At the first slit the beam momentum was 800 Mev/c with a spread of ±1% coherently focused across the slit in the horizontal plane. A beryllium wedge was placed in the beam so that the high-momentum side traversed the thick end while the low-momentum side was only slightly slowed by the pointed end. After wedging, the momentum spread was reduced to $\pm\frac{1}{2}$%. The second stage was then essentially free of chromatic aberrations.

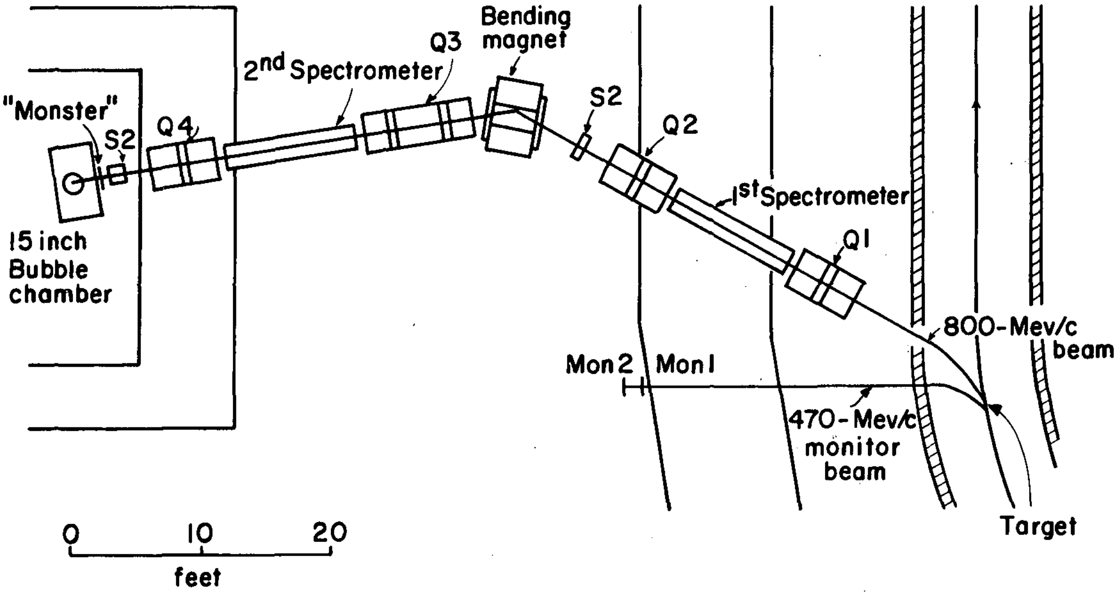

MU-26753

Fig. 1. 800-Mev/c K^- beam at the Berkeley Bevatron (October 1960—January 1961).

There were two main causes of K^--meson loss. The mean decay distance of K^- at 800 Mev/c is 19.5 ft, while the beam length from target to bubble chamber was some 75 ft, or 3.85 mean lives. Thus, only 2.1% of the K^- starting at the target lived long enough to reach the bubble chamber. The length of the beam was determined by the Bevatron crane limits and not by the magnet elements. The π^- also decayed but, having a longer lifetime and higher velocity, survived to a greater extent. Even those that decayed contributed to a μ^- background.

The second cause of K^- loss was through absorption in the copper absorber, which served to degrade the incident momentum. This loss depended on the amount of absorber but varied between a factor of 4 and 5. This degrading also increased the relative momentum spread as the central momentum decreased. As shown in Fig. 2, the spreads are consistent with the initial 800 Mev/c ± 1/2% determined during the "tuneup" period.

There are three factors worth special mention which tended to minimize π^- and μ^- background. The narrow momentum spread in the second stage minimized chromatic aberrations which would have allowed π^- to creep into the K^- image. The first stage may have suffered significantly from these aberrations, since the momentum spread was actually some 8 to 10% just before the first mass-resolving slit.

A second point was the strategic positioning of the bending magnet. This magnet, which bent the beam through 38°, also acted as a momentum analyzer preceding the second stage. Most of the off-momentum background that succeeded in passing through the first slit was not channeled down the second stage, but was lost on the collimators that preceded the second spectrometer or on the walls of the vacuum system.

The third and perhaps most novel point was shifting the final K^- image off center of the second spectrometer gap. This shift makes it impossible for pions scattered off the spectrometer plates to enter the K image. This is not obvious, but refer to Fig. 3. The lens Q (a quadrupole doublet) takes all rays entering from the right with a given angle and focuses them at corresponding points on its focal plane. The distance between the π and K images is the π^--K^- separation previously stated as 1/2 in. By varying the magnetic field only, both of these images move vertically and maintain their separation. If an unscattered pion normally is deflected through an angle θ_π, then a pion scattering off the

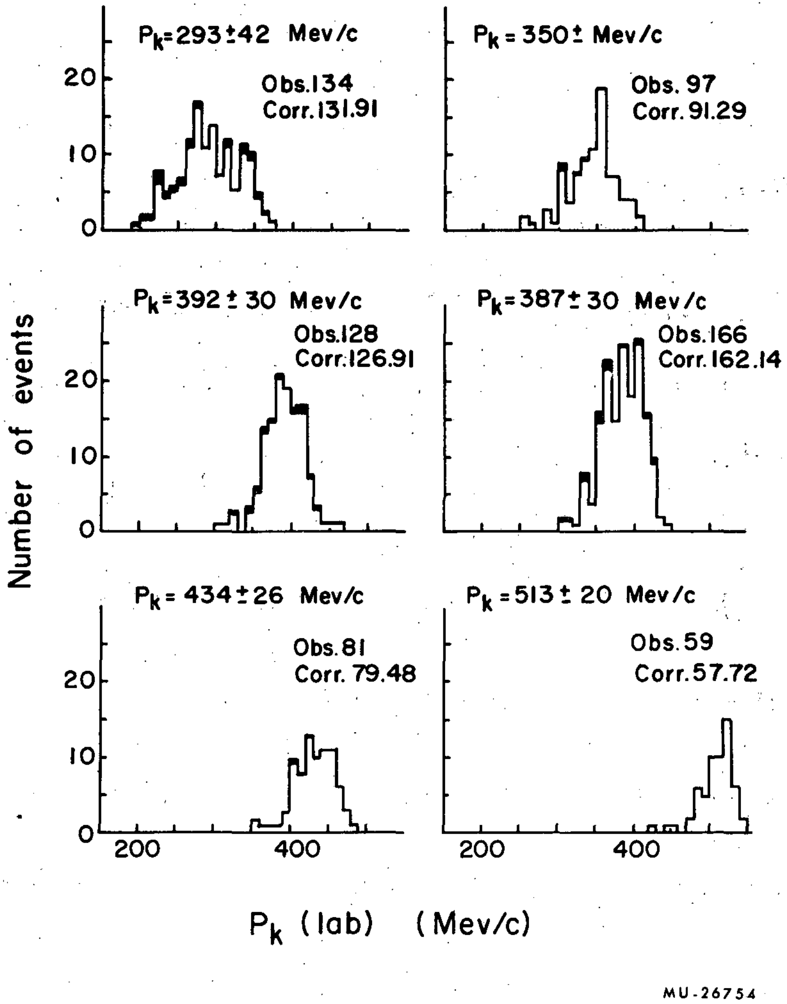

Fig. 2. Momentum spread of the incident K^- for τ decays at the six exposure settings. The shaded areas are the relativistic correction $(P_{bin}/P_{central})$ to give the relative number of K^- at P_{bin}.

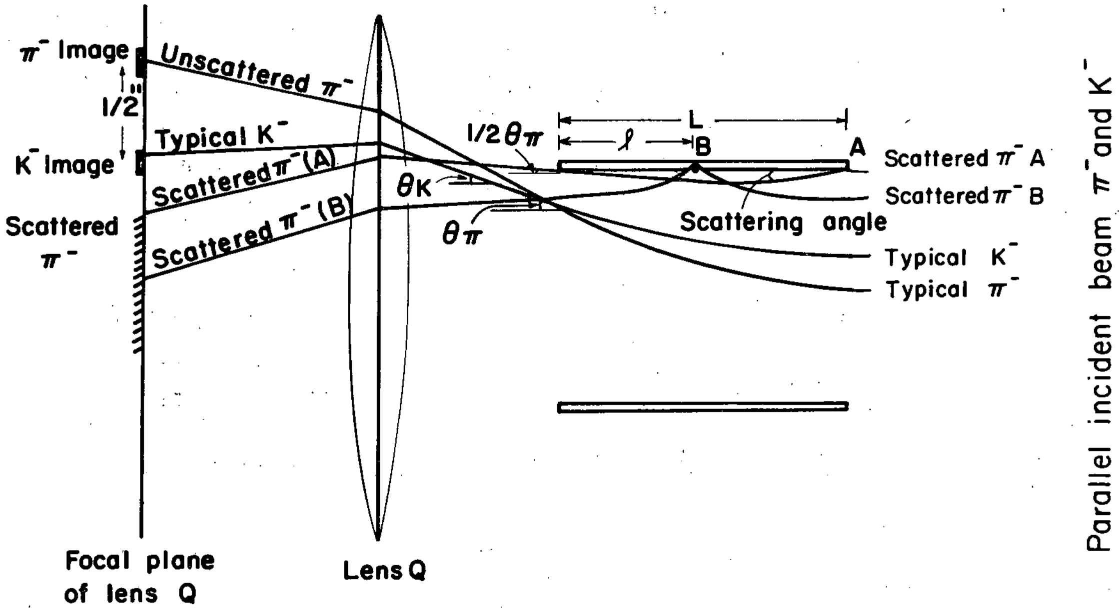

MU-26755

Fig. 3. Ray diagram demonstrating that scattered pions could not enter the off-center K^- image at the second slit.

plate must enter the lens Q with an angle less than or equal to $\frac{1}{2}\theta_{\pi}$. Note that scattered ray A, which scatters at the entrance edge and barely missed the exit edge of the plate, has this maximum exit angle.

A second scattering would have occurred if the scattering angle had been less. A larger scattering angle would certainly have resulted in a smaller final angle. If the scattering occurs further down the plate, as ray B, for example, the angle of bend after scattering is reduced, since there is less magnetic field to be traversed. The remaining angle of bend is $(\ell/L)\,\theta_{\pi}$. The portion of spectrometer plate that must be missed to avoid a second scattering is reduced by the same factor (ℓ/L). The problem is the same as that for ray A, except all quantities are scaled down by a factor ℓ/L.

At 800 Mev/c the K flux was 15 K^- per 10^{11} protons striking the target. Typically, during production running, there were about five K^- entering the chamber on each picture. There were approximately one or two background tracks, half of which were π^-. The π^- contamination was determined from π^--p scatterings observed in the chamber. Since π^- are not slowed down at the same rate as K^- mesons, the π^- had a systematically higher momentum. The difference in K^- and π^- mean momenta ranged from 100 Mev/c at 510 Mev/c for the K^- up to 200 Mev/c at 300 Mev/c K^- momentum. The actual mean K^- momenta for the various exposures were 292, 350, 387, 392, 434, and 513 Mev/c. The two exposures at 387 and 392 are combined on occasion as they differed by such a small amount.

B. Scanning

The film was scanned for interactions and decays by five scanner technicians. These people were chosen from a group of about eleven on the basis of satisfactory previous performance on similar film. Of the 193 rolls of film, 84 were second-scanned. Seven rolls were also second-scanned by myself, taking great pains to reach 100% efficiency. This effort took about 2 to 3 times as long per roll (365 pictures) as usual, requiring a typical scanning time per roll of 12 to 14 hours.

When an event was found it was classified according to the number of prongs leaving the production vertex. All V's that could have been associated and all subsequent decays were recorded. There were nine possible combinations, consisting of

0 prong
0-prong V
1 prong
2 prong
2-prong + decay
2-prong - decay
2-prong V
3 prong
4 prong.

The efficiency for detection of an event varies, of course, with the type of event and its position in the chamber. To eliminate poorly illuminated areas in the chamber a "fiducial volume" was chosen which provided a margin on all sides. All events found, both inside and outside the volume, were recorded.

The chamber as seen on the scanning projector was divided into four regions as shown in Fig. 4. For each event found, an identification both by prong number and region was recorded. The efficiency for finding events in the Z region was found to be much lower, and in many cases events were unmeasurable even though found. Accordingly, these events were discarded.

The efficiency for finding events by a single scan was measured in two ways. Scanning results of the seven rolls, which were thoroughly scanned by myself, were compared with the normal scan results. Table I shows this comparison;

Table I. Difference between normal scan and thorough scan in CNF region of chamber Comparison based on seven rolls.

Event Type	0	0V	1	2	2±	2V	3
Thorough scan %	95	100	99.7	100	100	100	100
No. Events missed	4	0	2	0	0	0	0
Normal scan %	94	100	95	97.9	100	100	100
No. events missed	5	0	34	6[a]	0	0	0
No. events found	83	46	662	290	103	9	39

[a] Three of these would have been disregarded under the acceptance criteria.

the two scans combined were assumed to be 100% efficient.

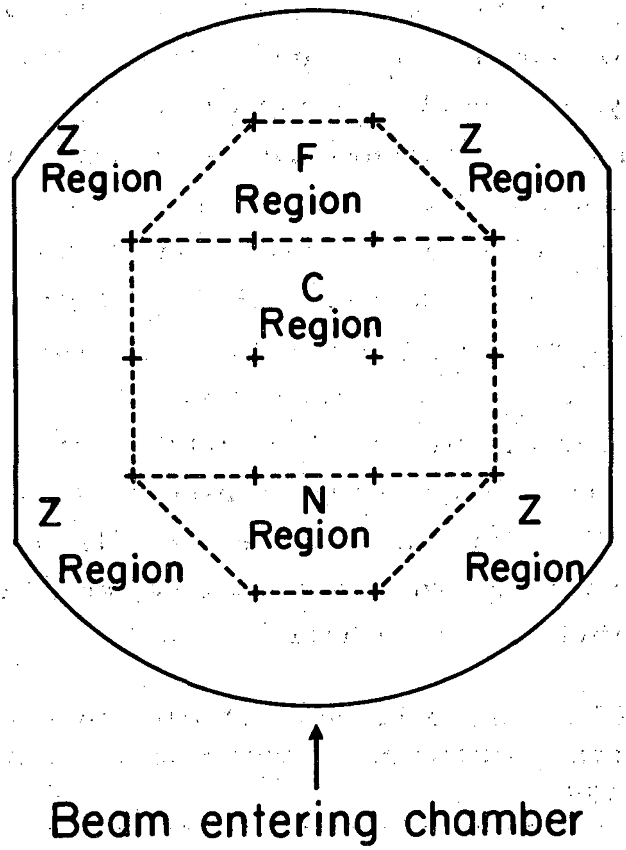

MU-26756

Fig. 4. Fiducial volume designations as seen on the scanning projector. The + marks are on the top of the glass.

The 0-prong and 1-prong events were not used, and can be neglected. Three of the six 2-prongs missed were found to have very short recoils. These were all found to have cosines of the scattering angle greater than 0.9, and would have been eliminated under the acceptance criteria for K-p scatterings. Since these efficiencies are so high for the chosen fiducial volume, it seems reasonable to assume that two scans of the normal type would approximate 100%. The comparison of the results of the two normal-type scans on 42 rolls for 0-prong V, 2-prong, 2-prong ± decay, 2-prong V, and 3-prong events are shown in Table II.

Table II includes as missed events those misrecorded as 1-prongs, or incorrectly placed in the Z region, since such events were never examined and were effectively lost. The efficiency for detecting all the event types studied was extremely high. It is highly unlikely that the efficiency for 3-prong detection was actually lower than for 2-prongs. Since the number of missed events was so small, the lower efficiency calculated for 3-prongs was probably just a statistical fluctuation. No corrections for scanning losses were made in computing the cross sections, since all the efficiencies were essentially the same. The path length, which was computed from the number of τ decays, was subject to the same inefficiency as the interactions.

Table II. CNF region double normal scan comparison of 42 rolls.

	Event Type	V	2	2±	2V	3
1st scan only	% Efficiency	98.3	97.1	99.2	100	97.0
	Events missed Satisfying acceptance criteria	1	19	1(3)[a]	0	4
1st and 2nd scan	Total events found	235	662	376	30	133

[a] If two zero-length Σ's missed as two prongs are included.

C. Sketching and Measuring

A sketch was made for each event selected to be measured. This sketch served to specify to the measurer which two of the four pictures of each frame presented the best stereo pair. On the sketch card a record of the date of measurement, measurement number, and the measurer's initials was also kept.

Once sketched, the event was measured by using one of the "Franckensteins." These machines are essentially projection microscopes which digitize in Cartesian coordinates several points along each track of the event in the photograph. These coordinates are punched on IBM cards along with appropriate reference points and event-identifying information. The cards served as input to the event-reconstruction computer programs.

D. Event Reconstruction

Each event was reconstructed, track by track in space, from the digitized input cards by the IBM 7090 program PACKAGE. This was the standard program generally in use by the Alvarez Group for event reconstruction. After reconstruction, the same program subjected the measured variables on each track to the constraints of momentum and energy conservation for the entire event. The measured quantities were adjusted to give the best fit satisfying the constraints, as measured by a χ^2 calculated by the program. In most cases each event was subjected to several different interpretations. Usually, the χ^2 value would unambiguously select one interpretation. Appendix I discusses the χ^2 distributions and examines the validity of the fitting procedure.

A more detailed discussion of the PACKAGE program and its predecessors PANG and KICK is presented elsewhere.[4] The output of PACKAGE was in the form of a binary magnetic tape which served as input to a series of short Fortran EXAMIN routines. These calculated and organized the pertinent physical quantities not directly measured.

E. Remeasurements and Hand Analysis

When an event failed to satisfy appropriate acceptance criteria the sketch was resubmitted for measurement. The remeasured event then proceeded through the system from that point on. The acceptance criteria for each event type are discussed later. After repeated failure to get through the system the event was analyzed by hand.

III. EVENT ANALYSIS

A. τ Decays and Path Length

Although τ decays are not interactions of K^- mesons, these events were examined to determine the incoming flux of K^-. This type of decay is very spectacular in the bubble chamber, the incident track terminating in a 3-prong star of decay pions. Figure 5 shows a typical event. Tables I and II support the belief that the scanning efficiency for these events was very high. In addition to the ease of detection, the τ decay can be well measured, since the tracks of the decay pions are usually long and have a reasonable curvature. The incident-K^- momentum determined from these events had a typical uncertainty of ±5 Mev/c. The K^--momentum spectra from τ decays found in each of the momentum intervals examined are shown in Fig. 2. By use of a K^- lifetime of 1.224×10^{-8} sec and a branching ratio of 5.77%,[5] the flux of K^- at each interval is easily determined by simply counting the number of τ decays. The momentum spread of all incoming K's is identical to the decay spectrum after correction for time dilation. The shaded areas show the results of this correction, which is simply weighing the number of τ's in each bin by a factor $(P_{bin}/P_{central})$.

At each momentum interval the shape of the spectrum is as expected, approximately Gaussian with a long low-momentum tail. All interactions and τ decays whose momenta were determined by fitting to be 100 Mev/c below the nominal central momentum for each interval were discarded. Such events were usually not part of the low-momentum tail, but resulted from the "irrational" part of the beam. They usually entered the chamber at odd angles to the "rational" beam and often resulted in very-low-momentum or stopping K^- interactions. The source of these K's was probably large-angle scatterings in the absorber or final mass-resolving slit.

Once the τ decays for each momentum interval were measured, the knowledge of the central momentum and spread so determined was used in fitting all other types of events. This was done by averaging the known central incident momentum weighted by its spread with the measured incident momentum weighted by its error. Actually, each event was fitted both with and without this "beam averaging," permitting truly off momentum events to be recognized. The beam-averaging procedure

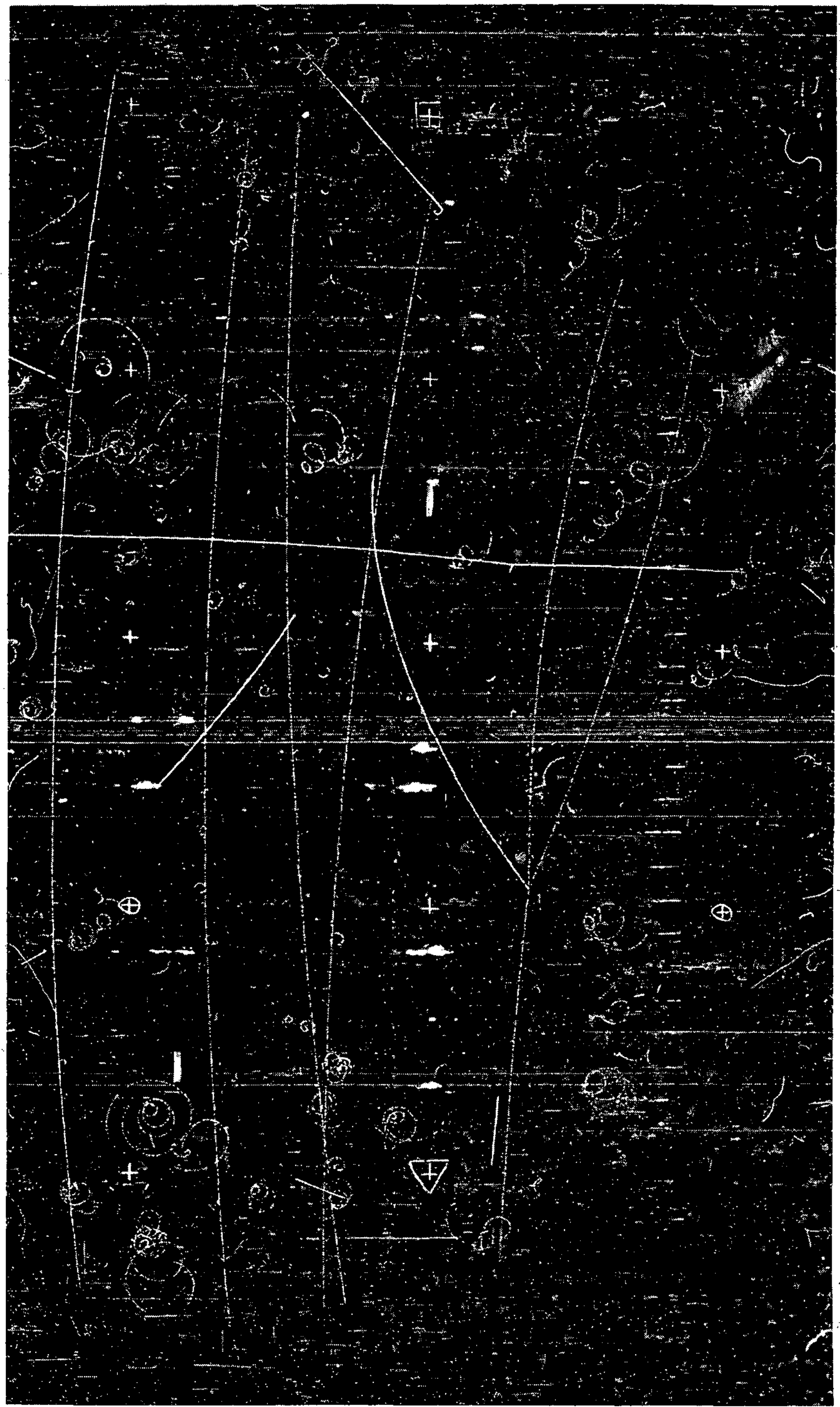

ZN-3095

Fig. 5. A typical 3-prong τ decay.

allowed a tighter determination of the incident momentum than possible by direct measurement only. When the incident track was very short or hidden by other tracks, direct measurement often gave absurd values.

In addition to being used for determining the cross sections, angular distributions, and polarizations at 293, 350, 387, 392, 434, and 513 Mev/c, the data were merged and re-examined in detail. All events, excluding those from the 513-Mev/c interval, were mixed and subdivided into 10- or 20-Mev/c bins. The τ -decay momentum spectra show the extent of the overlap between adjoining intervals. (The 513-Mev/c interval shows little overlap and is removed from the region most important to the conclusions of Section IV.)

The tails of the τ -decay momentum spectra show large fluctuations, as expected when so few events are involved. The errors assigned to the number of τ's in these intervals are appropriately very large. Cross sections calculated in such intervals would have had very large errors, since both the τ decays and the number of events were few. Knowledge of the beam characteristics, however, has been ignored by such a procedure. Accordingly, the exposure at each momentum was fitted to a curve which may be described as a long-tailed Gaussian. The form of the curve was suggested by naively neglecting straggling. The distribution of residual ranges then should be

$$N(R)\, dR \approx A \exp\left[-(R - R_0)^2/\Delta R_0\right] dr.$$

Now, using $R \approx p^{\alpha}$ suggests a suitable empirical form,

$$N(p)\, dp \approx A \exp\left\{- B\left[(P/C)^{\alpha} - 1\right]^2\right\} dp.$$

The normalization A, central momentum C, and "width" B were the variables of the fit. Since the form of the curve was certainly not rigorous, α was also allowed to vary. The curve obtained is only the "best smooth curve" through the data. The net effect of this procedure was to correlate the number of events in each bin to all other bins and hence reduce the statistical error. The errors for A,B,C, and α were estimated by evaluating the second derivatives of the χ^2 function at minimum. The error on the number of τ decays in each bin was then evaluated by using the full error matrix of A, B, C, and α. The curves shown on Fig. 6 are the fits obtained for the exposure at each momentum.

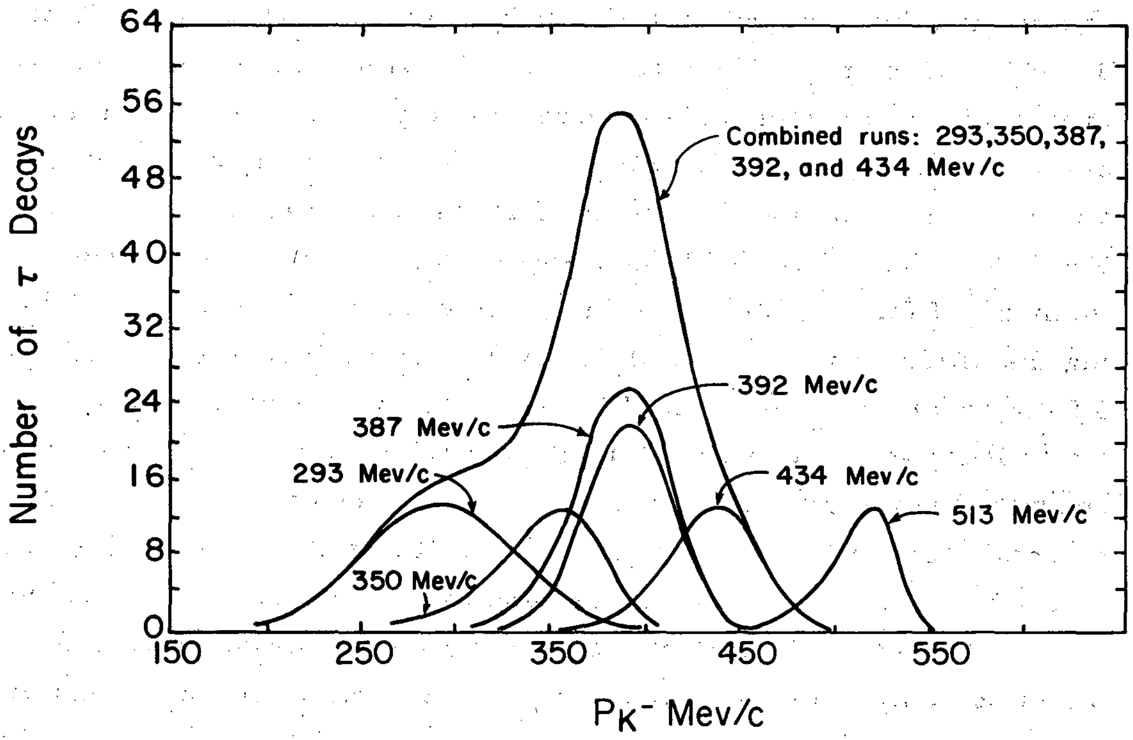

MU-26757

Fig. 6. "Best smooth curves" for the τ decay K¯ momentum spectra. The top curve is the sum of the curves for 293, 350, 387, 392, and 434 Mev/c.

B. Elastic Scattering: $K^- + p \rightarrow K^- + p$

Elastic scatterings represent roughly one-half of all interactions. Those chosen for analysis were found entirely in the "2-prong" events. Obviously, for small-angle scatterings in which the recoil protons carry off little momentum there is some minimum angle beyond which the protons are no longer visible. Such an event would be classified as a "1-prong" and lost among the thousands of K^- decays. Long before the recoil becomes completely invisible, the efficiency for picking up the proton stub drops considerably. Rather than attempting to evaluate the detection efficiency, which varies rapidly with scattering angle, all events with cosines of the scattering angle greater than 0.9 in the center-of-mass were eliminated. Figure 7 shows the length of the recoil proton versus K^- momentum for center-of-mass scattering cosines of 0.9 and 0.95. The 0.9 cutoff should guarantee a high scanning efficiency. A uniform cutoff for all momentum intervals was desirable to simplify merging the different runs. For the higher momentum intervals the 0.9 cutoff may seem too stringent. The pion contamination in the beam, however, leads to π^--proton scatterings which at forward angles cannot be separated from K^--proton scatterings. For cosines less than 0.9 this ambiguity essentially disappears. Thus, 0.9 was chosen both to eliminate short-recoil scanning losses and the π^--p scattering contamination.

If the plane of an elastic scattering were vertical the camera eye might see only the edge of the plane. Thus, we might expect a scanning bias against detecting scatterings in which the plane of scattering is nearly vertical. There are two factors tending to reduce the effect of this bias. The bubble chamber has four camera "eyes." Whereas one camera might view only the "edge" of the plane, the event should be clearly seen in one of the other views. Also, the magnetic field in the chamber deflects the scattered K^- and protons in opposite directions. Therefore, even an edge-on view usually appears V-shaped. Small-angle scatterings with short recoils and little momentum loss by the K^- would be the most likely to be missed. Figure 8 shows the distribution of events for various orientations of the plane of scattering. This distribution should be isotropic. The cos θ = 0.9 scattering cutoff is stringent enough to eliminate this source of trouble.

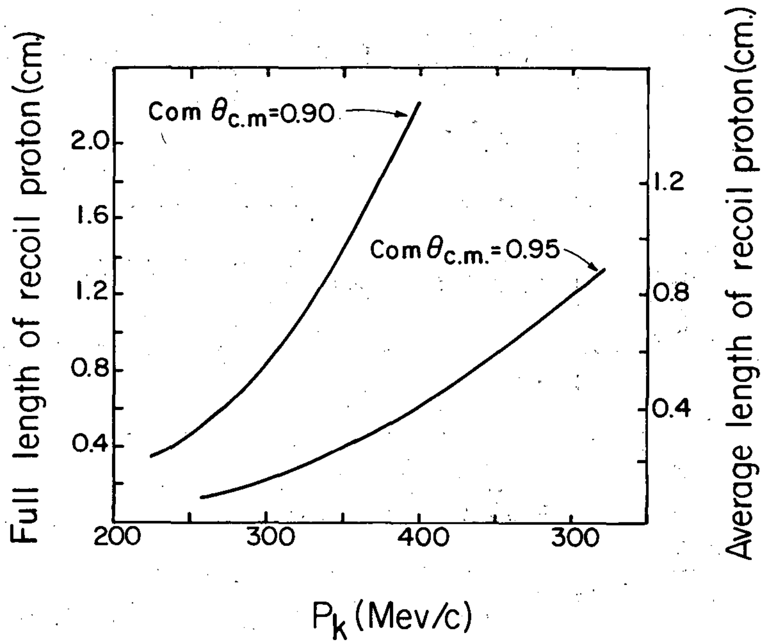

MU-26758

Fig. 7. Length and average projected length of the recoil proton in elastic scatters for fixed c.m. scattering angles. The cos $\theta_{KK'}$ = 0.9 cutoff was adopted.

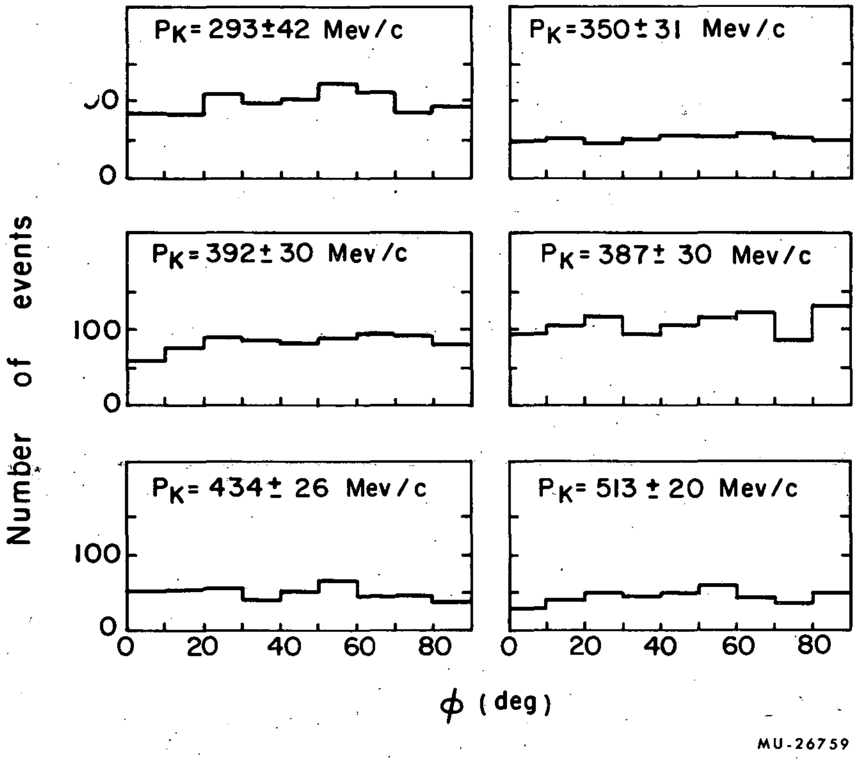

Fig. 8. Distribution of elastic scatterings versus the angle ϕ, where

$$\cos\phi = \frac{(\vec{K}_{in}\times\vec{K}_{out})\cdot(\vec{K}_{in}\times\hat{z}_{axis})}{|\vec{K}_{in}\times\vec{K}_{out}|\ \ |\vec{K}_{in}\times\hat{z}_{axis}|}\ .$$

$\vec{K}_{in}$ and $\vec{K}_{out}$ are vectors in the incident and outgoing K directions and the z axis is vertical; $\phi = 0^{\circ}$ for a vertical scattering plane. The distributions are folded about 90°, 180°, and 270°.

Figure 9 shows the distribution of errors for the incident-K^- momentum obtained by fitting. The strange double peaks can be explained as follows. For small angles the recoil-proton momenta are well defined, since the protons stop in the chamber. For very large angles the scattered K^- stop. Since a momentum from range measurement is much more accurate than momentum via curvature, both very forward and very backward scatterings should yield tighter fits. An exact correspondence between stopping tracks and the first peak was, in fact, found. Based on these distributions the incident-momentum resolution is precise enough to justify division of the data into 20-Mev/c bins. Such a division is discussed in Section IV.

Figures 10 through 12 show the angular distributions for each of the momentum settings individually. These distributions were fitted by a least-squares procedure to a polynomial of the form

$$\frac{d\pi}{d\Omega} = A_0 + A_1 \cos \theta_{kk}' + A_2 \cos^2 \theta_{kk}' + \ldots + A_n \cos^n \theta_{kk}' .$$

The results of these fits for orders $n = 0$ to $n = 4$ are displayed in Table III. At 293 Mev/c the flat $n = 0$ fit is sufficient, whereas for the higher intervals terms up to $\cos^2 \theta_{kk}'$ seem to be both necessary and sufficient to fit the data. The $n = 2$ curves were integrated to estimate the number of scatterings at all cosines and hence the cross sections for elastic scattering. The cross sections determined in this way are shown in Fig. 13.

The optical theorem relates the imaginary part of the forward scattering amplitude to the total cross section. The square of the imaginary part gives a lower limit to the differential cross section in the forward direction. The square of this imaginary part is shown for each distribution in Figs. 10 through 12. The square of the real part of the forward scattering amplitude is the difference between the observed angular distribution at zero degrees and the square of the imaginary part. Table IV displays the real and imaginary parts for the various momentum exposers.

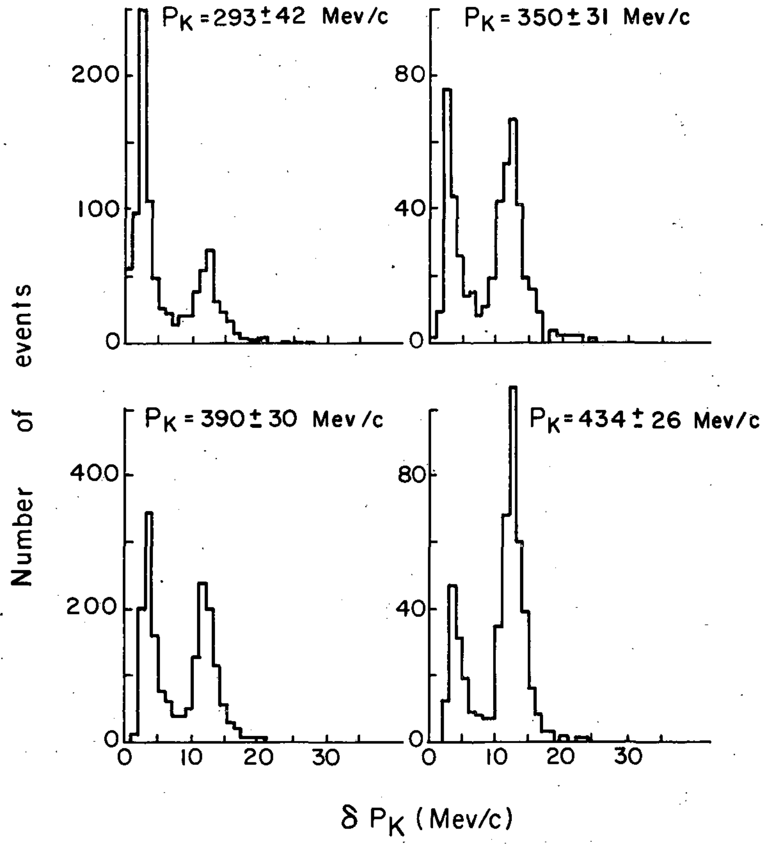

MU-26760

Fig. 9. Incident-K^- fitted momentum error for elastic scatterings. The double peaks are due to the different accuracies attainable in the momentum determinations of the scattered particles for stopping and leaving tracks.

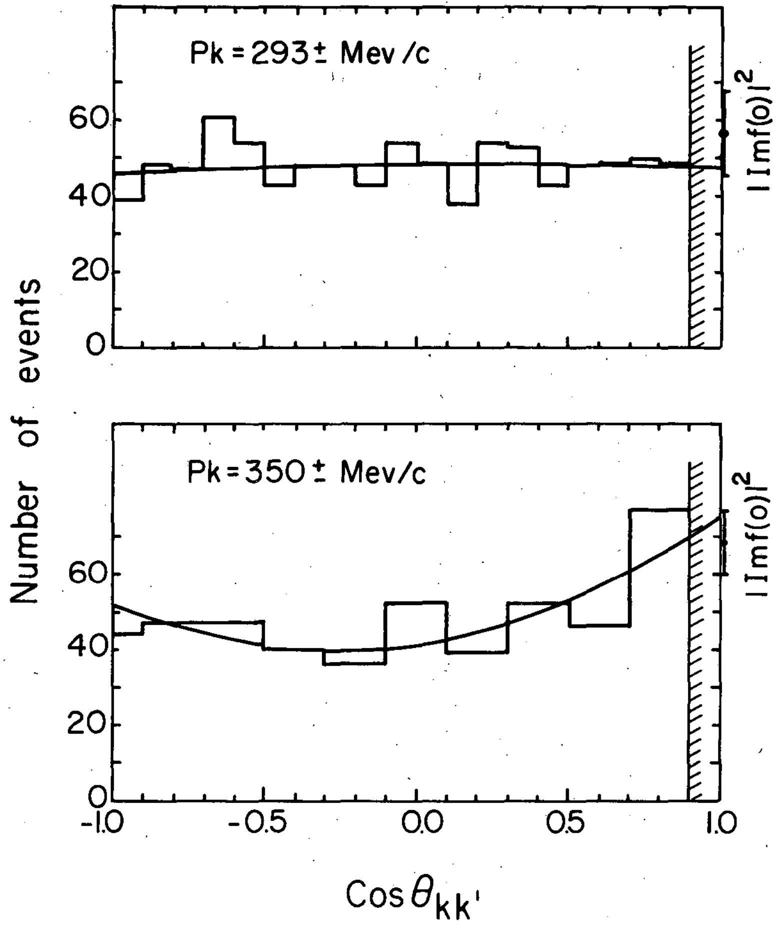

MU-26761

Fig. 10. Angular distribution for elastic scattering, $K^- + p \rightarrow K^- + p$, for the 293- and 350-Mev /c runs.

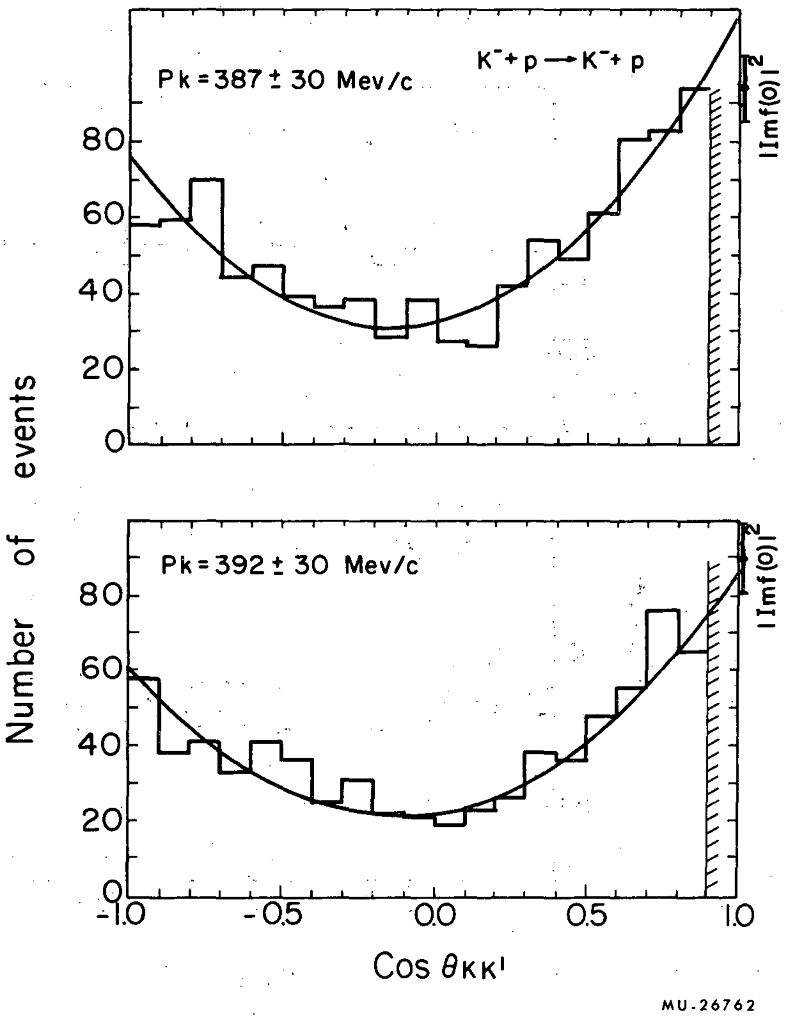

Fig. 11. Angular distribution for elastic scattering, $K^- + p \rightarrow K^- + p$, for the 387- and 392-Mev /c runs.

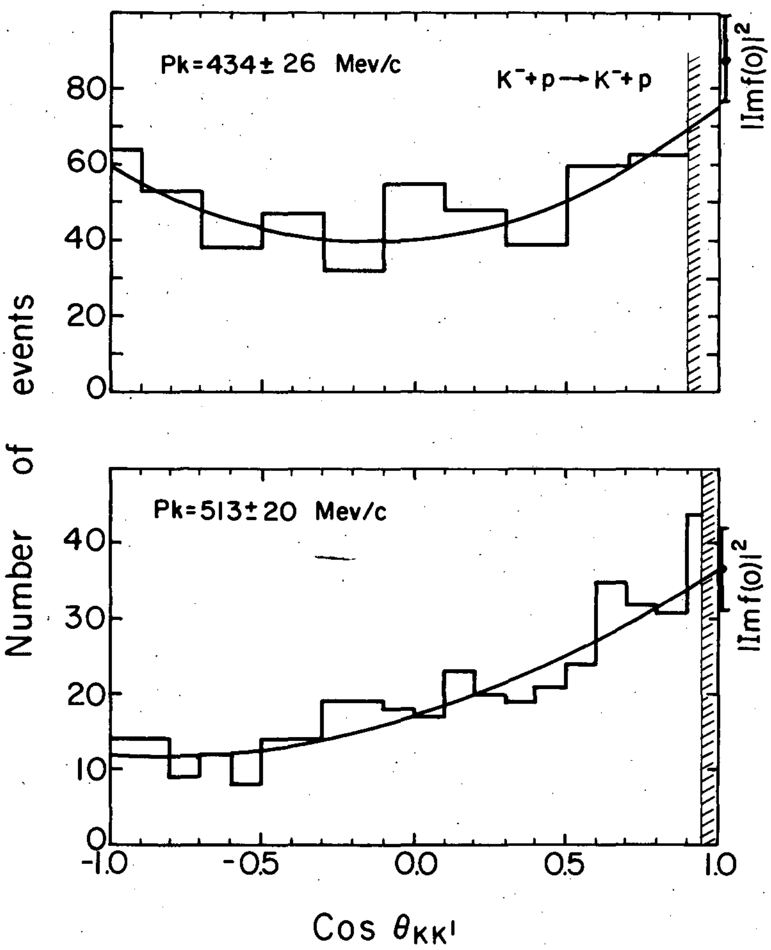

MU-26763

Fig. 12. Angular distribution for elastic scattering, $K^- + p \rightarrow K^- + p$, for the 434- and 513-Mev/c runs.

Table III. K^--P Elastic scattering: least-squares fits to angular distributions.

Momentum interval (MeV/c) and cross section (mb)	Order of Fit	A coeff	B coeff	C coeff	D coeff	E coeff	χ^2	expected χ^2
293 ± 42	0	47.7 ± 1.6					11.8	18
σ = 48.2 ± 4.2	1	47.8 ± 1.6	1.0 ± 2.9				11.7	17
	2	48.1 ± 2.4	0.9 ± 3.0	-1.2 ± 5.8			11.6	16
	3	47.7 ± 2.4	-6.3 ± 7.2	1.1 ± 6.2	13.4 ± 12.3		10.5	15
	4	45.7 ± 3.0	-4.0 ± 7.5	24.3 ± 21.0	7.0 ± 13.5	-30.7 ± 26.5	9.1	14
350 ± 31	0	46.2 ± 2.2					18.8	9
σ = 34.0 ± 3.2	1	47.0 ± 2.2	8.1 ± 4.3				15.3	8
	2	41.1 ± 3.2	11.7 ± 4.5	22.6 ± 8.8			8.7	7
	3	40.1 ± 3.3	0.3 ± 10.1	28.1 ± 9.8	23.5 ± 18.7		7.1	6
	4	41.6 ± 4.0	-2.3 ± 10.9	9.8 ± 30.0	30.9 ± 22.0	26.4 ± 40.9	6.7	5
387 ± 30	0	44.8 ± 1.5					122.3	18
σ = 31.9 ± 2.5	1	45.6 ± 1.6	8.2 ± 3.3				116.2	17
	2	32.2 ± 2.1	18.6 ± 3.4	62.6 ± 6.4			19.2	16
	3	31.4 ± 2.1	6.2 ± 7.2	67.8 ± 6.9	26.2 ± 13.2		15.3	15
	4	29.3 ± 2.5	1.1 ± 7.7	99.7 ± 20.8	14.1 ± 15.2	-46.2 ± 28.3	12.6	14
392 ± 30	0	31.4 ± 1.1					107.8	18
σ = 34.0 ± 3.0	1	31.4 ± 1.1	2.1 ± 2.7				107.2	17
	2	22.0 ± 1.5	12.3 ± 2.9	51.4 ± 5.4			17.4	16
	3	22.3 ± 1.5	3.3 ± 5.5	54.0 ± 5.6	20.5 ± 10.6		13.7	15
	4	21.2 ± 1.9	4.9 ± 5.8	68.9 ± 17.9	16.1 ± 11.8	-21.5 ± 24.6	12.9	14
434 ± 26	0	46.9 ± 2.2					21.7	9
σ = 30.6 ± 3.4	1	47.3 ± 2.2	5.1 ± 4.3				20.4	8
	2	40.2 ± 3.2	8.1 ± 4.4	27.3 ± 9.0			11.3	7
	3	40.6 ± 3.3	14.0 ± 10.1	25.2 ± 9.6	-12.1 ± 18.9		10.8	6
	4	43.2 ± 4.1	10.1 ± 10.7	-6.8 ± 30.6	-1.9 ± 21.0	45.6 ± 41.3	9.6	5
513 ± 20	0	16.4 ± 0.9					49.8	18
σ = 26.5 ± 3.3	1	19.0 ± 1.0	11.0 ± 1.8				12.7	17
	2	17.2 ± 1.4	12.5 ± 2.0	6.8 ± 3.8			9.5	16
	3	17.4 ± 1.5	14.3 ± 4.2	5.9 ± 4.3	-3.8 ± 7.6		9.2	15
	4	18.9 ± 1.8	10.8 ± 4.8	-11.3 ± 12.5	4.0 ± 9.2	24.0 ± 16.3	7.1	14

(Units are number of events per bin for 10 or 20 bins.)

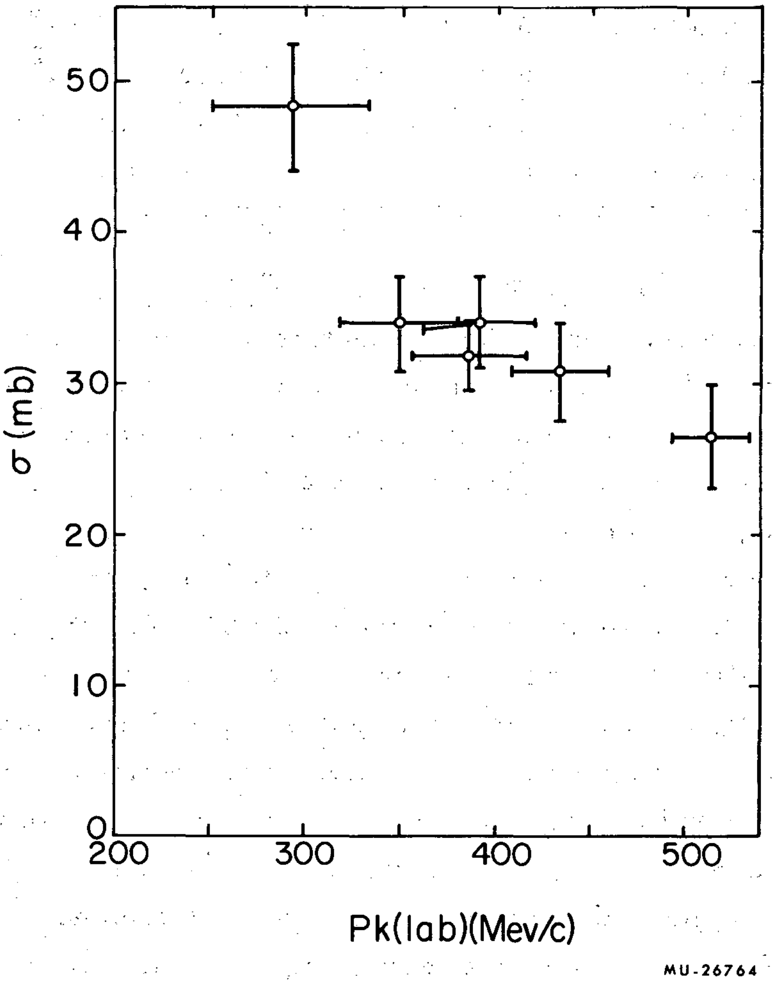

Fig. 13. $K^- + p \rightarrow K^- + p$ elastic scattering cross section. Each point is averaged over the natural spread of the beam at that momentum as indicated in Fig. 2.

Table IV. Real and imaginary parts of the forward elastic scattering amplitude.

Momentum exposer	F^2	I^2	R^2
293 ± 42 Mev/c	$0.38 \pm 0.06\ f^2$	$0.46 \pm 0.05\ f^2$	$-0.08 \pm 0.06\ f^2$
350 ± 31 Mev/c	$0.42 \pm 0.07\ f^2$	$0.38 \pm 0.05\ f^2$	$0.04 \pm 0.07\ f^2$
387 ± 30 Mev/c	$0.54 \pm 0.05\ f^2$	$0.40 \pm 0.04\ f^2$	$0.14 \pm 0.05\ f^2$
392 ± 30 Mev/c	$0.59 \pm 0.07\ f^2$	$0.62 \pm 0.06\ f^2$	$-0.03 \pm 0.07\ f^2$
434 ± 26 Mev/c	$0.38 \pm 0.06\ f^2$	$0.44 \pm 0.06\ f^2$	$-0.06 \pm 0.06\ f^2$
513 ± 20 Mev/c	$0.40 \pm 0.11\ f^2$	$0.38 \pm 0.06\ f^2$	$0.02 \pm 0.11\ f^2$

C. $\Sigma^{\pm}$ Production: $K^- + p \rightarrow \Sigma^+ + \pi^-$ or $\Sigma^- + \pi^+$

A brief look at the kinematics of sigma-hyperon production for the range of K^--meson lab. momenta discussed here reveals a disturbing fact. Sigmas of both signs produced in the backwards direction have such low lab. momenta that they stop and hence decay or interact before making a visible track. Such an event would be recorded as a 2-prong event or possibly even a 1-prong V ($K^- + p \rightarrow \Sigma^- + \pi^+$; $\Sigma^- + p \rightarrow \Lambda + n$; $\Lambda \rightarrow p + \pi^-$).

The protonic decay mode of the Σ^+ may appear very similar to an elastic scattering if the production-pion ionization is not examined carefully or if the track is dipping steeply. In the examination of 2-prong events, during the search for elastic scatterings, a group of events was found in which ionization and curvature indicated the outgoing tracks were a π^- and a proton. Furthermore, events in which the outgoing tracks appeared to be π^+ and π^- were also found. Neither of these groups satisfied the elastic-scattering requirement that the incident and outgoing tracks be coplanar. These events may be interpreted as charged sigmas productions in which the Σ went backwards and could not leave a visible track, or else decayed so quickly after production that no track was visible. This hypothesis was tested by the computer programs for all 2-prong events.

A perhaps surprisingly unique identification of invisible Σ's was achieved. In each case the incoming K^- and one of the outgoing tracks was used in fitting to the Σ-production hypothesis.

Energy and momentum conservation require four constraints to be satisfied in the fit. Since the Σ was not seen, three of the constraining equations were used to calculate the Σ-production characteristics (its vector momentum, for example). This left the production fit once overdetermined. The Σ so determined and the third observed track were fitted to the Σ-decay hypothesis. This fit was also once overdetermined. As a result of this chain of reasoning the invisible Σ's usually satisfied the following criteria. First, they would fail to fit either K^-p or π^-p elastic scattering; and second, both the Σ-production and subsequent Σ-decay hypotheses gave consistent fits with the data. There seemed to be only two ambiguous cases. Occasionally π^-p scatterings would fit both invisible Σ^+ production with a subsequent protonic decay of the Σ^+. These events, however, would invariably show anomalously high incident momenta. A scanning table examination of the incoming track's ionization would usually differentiate between these two possibilities.

For those events in which two final-state pions were observed, the second typical ambiguity arose. Both Σ^+'s produced in the very forward directions and Σ^-'s produced in the very backward directions would fit, and visa versa. Since a Σ produced in the forward direction has a momentum of the order of 800 Mev/c, it is very unlikely that it would decay before leaving a discernible track. Accordingly, all events of this type were classified according to that type which required a backwardly produced Σ.

The fraction of Σ's that were truly invisible was very small, and the treatment of these events as described above should be as good as or better than trying to compensate for losses by assigning various weights to selected events. The examination of the 2-prong events for Σ production resulted in detecting many extremely short but visible Σ's which otherwise would have been lost. Furthermore, forwardly produced Σ^+'s of considerable range, decaying via the protonic mode, were also found classified among the 2-prongs owing to the very small Σ^+-proton projected angle. Indeed, at 513 Mev/c K^- momentum the maximum Σ^+-p angle kinematically possible is only 19° for Σ's produced directly forward.

There is one further effect that should be mentioned. Any Σ^- hyperon, once produced, may interact with another proton according to the reactions

$$\Sigma^- + p \rightarrow \Sigma^0 + n \rightarrow \Lambda + \gamma + n,$$

$$\Sigma^- + p \rightarrow \Lambda + n.$$

In either case the Λ produced decays, 2/3 of the time, into a visible proton and π^-. The other 1/3 of the time only invisible neutrals result.

In order to estimate the number of Σ^- absorptions the percentage of Σ^- that would stop and interact was calculated. The possibility of in-flight absorption was neglected. On the basis of the number of decays observed in any angular region, the corresponding number of absorptions may be estimated. Since the number of events considered is so small, large statistical fluctuations are not surprising. Table V shows the comparison of absorptions observed and absorptions estimated. Although large fluctuations do occur for the individual intervals, for the combination of all intervals agreement is quite satisfactory. Both the total number of absorptions and the division into visible and invisible and Λ^- decay modes agree with the estimates extremely well.

There are several checks for overall consistency for identifying the $\Sigma^{\pm}$. Figure 14 shows the distribution of observed times from production to decay compared with the known lifetimes. Table VI shows the comparison of the pionic and protonic decay frequencies for the various momentum intervals. This ratio is known to be 0.51 ± 0.02.[6]

Figure 15 shows the distribution of errors on the incident-K^- momentum for $\Sigma^{\pm}$. Although there is a slight variation with production angle, the resolution seems sufficient to warrant division into 20-Mev/c bins. As we will see, the overall consistency of the results supports this assertion.

The angular distributions for each momentum setting are shown in Figs. 16 and 17. Again, a least-squares fit to powers of cos θ was made to various orders. Tables VII and VIII display the results of these fits. The curves drawn on Figs. 16 and 17 are the fits of order n = 2. Just as with the elastic scatterings, $\cos^2\theta$ is both necessary and sufficient to fit the data.

No significant depopulation or overpopulation can be found in the backwards Σ directions due to the "zero-length" sigmas. This further confirms the identification of these events. Since no corrections were needed, the observed numbers of events were used to calculate the

Table V. Observed and predicted Σ^- interactions for backwards Σ's

Momentum exposure interval (Mev/c)	Production cosine interval-cos $\theta_{K^-\pi^+}$	%Σ^- that should decay	Decays observed	Observed absorptions (visible + invisible Λ's)	Expected absorptions
293	1.0 to 0.9	44	4	3 (3 + 0)	5
	0.9 to 0.8	83	11	0 (0 + 0)	2
	0.8 to 0.7	96	14	2 (2 + 0)	0
350	1.0 to 0.9	57	1	4 (3 + 1)	1
	0.9 to 0.8	94	6	0 (0 + 0)	0
390	1.0 to 0.9	62	17	8 (3 + 5)	10
	0.9 to 0.8	98	24	3 (3 + 0)	0
434	1.0 to 0.9	73	14	2 (1 + 1)	5
	0.9 to 0.8	99	9	0 (0 + 0)	0
513	1.0 to 0.9	85	9	2 (1 + 1)	1
	0.9 to 0.8	100	6	0 (0 + 0)	0
Totals				24 (16 - 8)	24 (16 - 8)

Table VI. Decay branching ratios of Σ^+ hyperons, and the Σ^+ and Σ^- production ratios

	Momentum interval (Mev/c)						
	293 ± 42	350 ± 31	387 ± 30	392 ± 30	434 ± 26	513 ± 20	Total
Σ_0^+ ($\Sigma^+ \rightarrow p + \pi^0$)	146	78	188	158	68	67	705
Σ_+^+ ($\Sigma^+ \rightarrow n + \pi^+$)	126	86	190	169	66	44	681
$\Sigma_0^+/(\Sigma_+^+ + \Sigma_0^+)$	0.54	0.48	0.50	0.48	0.51	0.60	0.508
$\Sigma_0^+ + \Sigma_+^+$	272	164	378	327	134	111	1386
Σ^- all kinds	199	106	219	194	99	72	889
$(\Sigma_0^+ + \Sigma_+^+)/\Sigma^-$	1.37	1.55	1.73	1.69	1.35	1.54	1.56

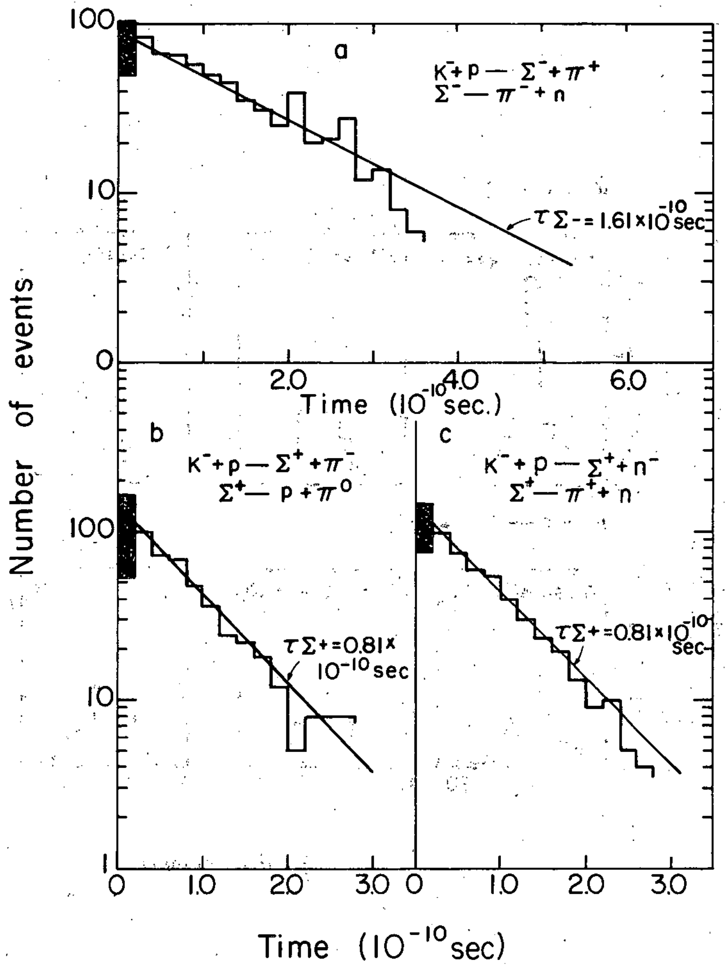

MU-26765

Fig. 14. Observed distribution of times from production to decay for Σ hyperons. The lines are drawn with a slope determined by the known lifetimes. The vertical positioning is from an eye-ball fit. The shaded areas represent the 2-prong events identified as Σ's.

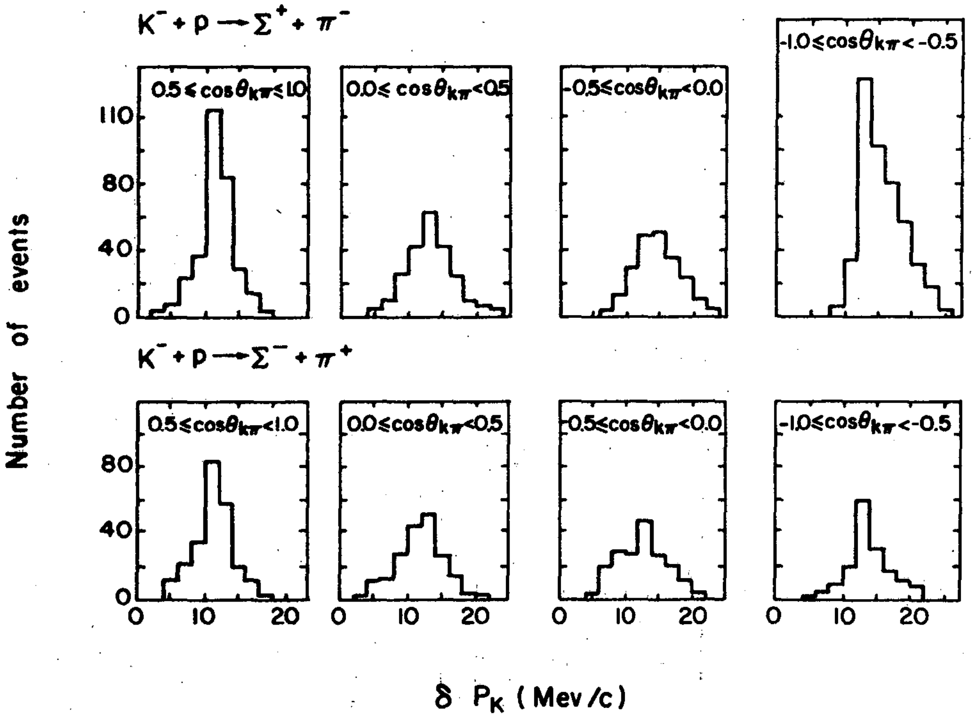

MU-26766

Fig. 15. Incident-K^- fitted momentum error for $\Sigma^{\pm}$ hyperon production.

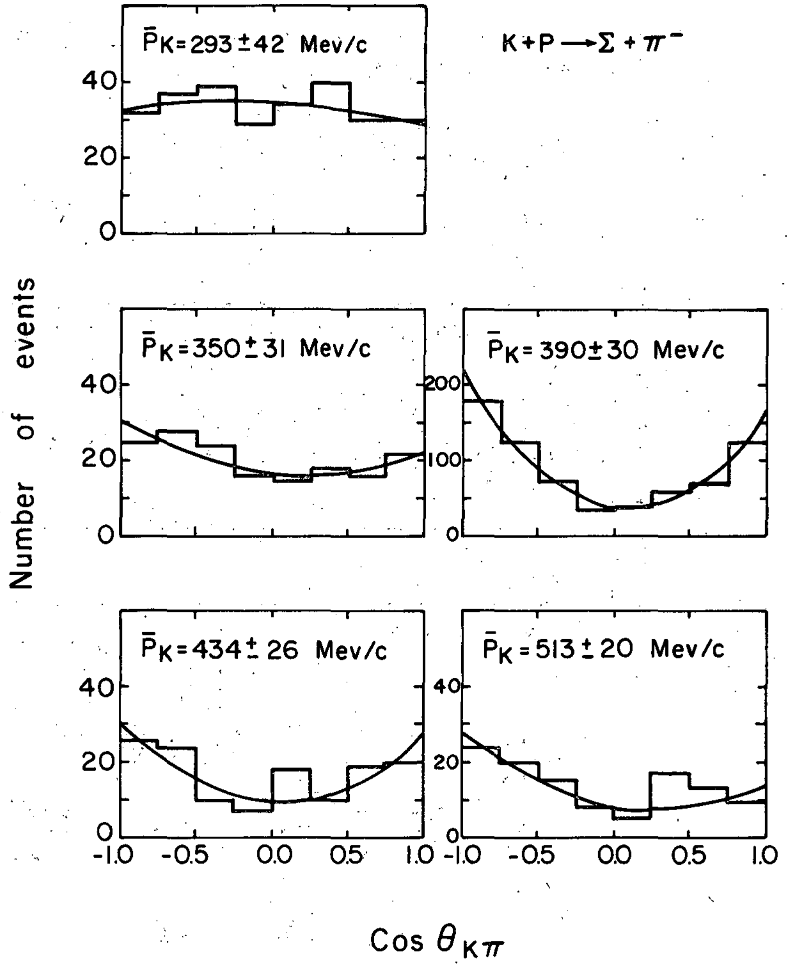

MU-26767

Fig. 16. Angular distributions for the reaction $K^- + p \rightarrow \Sigma^+ + \pi^-$. The curves are fits to $\frac{d\sigma}{d\Omega} = A + B \cos\theta_{K\pi} + C \cos^2\theta_{K\pi}$.

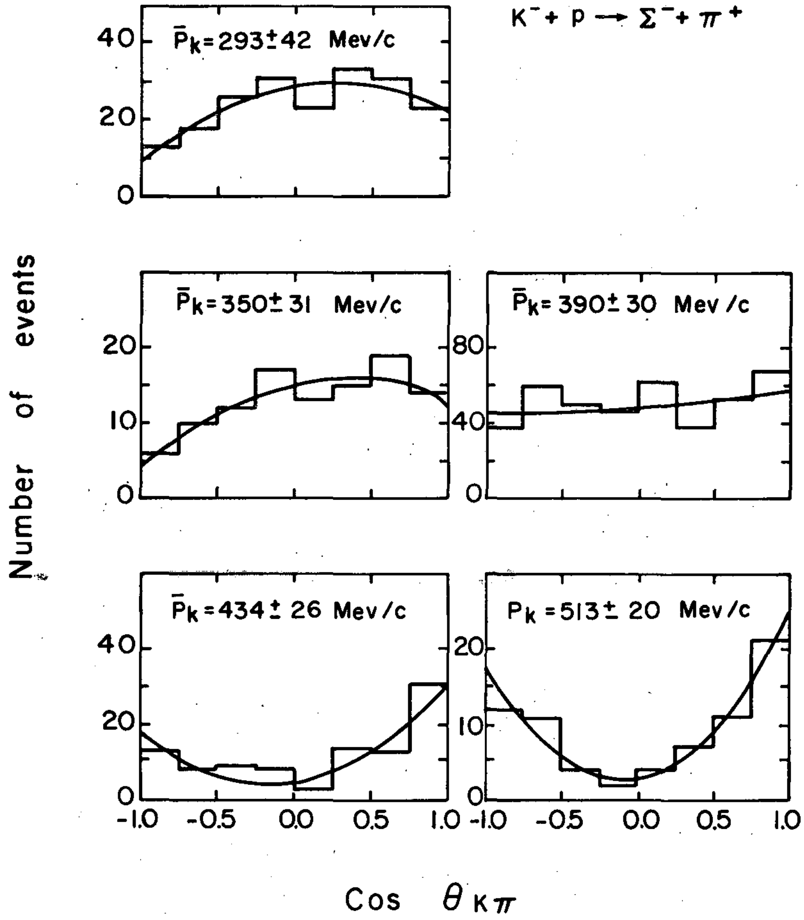

MU-26768

Fig. 17. Angular distributions for the reaction $K^- + p \rightarrow \Sigma^- + \pi^+$. The curves are fits to $\frac{d\sigma}{d\Omega} = A + B \cos \theta_{K\pi} + C \cos^2\theta_{K\pi}$.

Table VII. $\Sigma^+\pi^-$ Least-squares fits to the angular distributions

Momentum interval (MeV/c) and cross section (mb)	Order of Fit	A coeff	B coeff	C coeff	D coeff	E coeff	χ^2	expected χ^2
293 ± 42,	0	33.4 ± 2.0					3.8	7
σ = 13.6 ± 1.4	1	33.5 ± 2.0	-2.0 ± 3.5				3.1	6
	2	34.8 ± 3.1	-2.0 ± 3.5	-4.0 ± 7.0			3.1	5
	3	34.8 ± 3.1	-2.0 ± 9.8	-4.1 ± 7.0	.006 ± 15.4		3.1	4
	4	33.1 ± 3.9	-2.4 ± 9.8	15.7 ± 28.3	0.6 ± 15.4	-24.5 ± 34.4	2.6	3
350 ± 31,	0	19.5 ± 1.6					7.9	7
σ = 10.6 ± 1.4	1	19.8 ± 1.6	-4.5 ± 2.9				5.5	6
	2	17.0 ± 2.2	-4.8 ± 2.9	9.6 ± 5.6			2.6	5
	3	17.2 ± 2.3	-11.4 ± 7.4	9.4 ± 5.6	11.8 ± 12.1		1.6	4
	4	16.0 ± 2.8	-12.2 ± 7.5	25.2 ± 21.5	12.9 ± 12.2	-20.4 ± 26.9	1.0	3
387 ± 30,	0	34.9 ± 2.1					98.8	7
σ = 11.4 ± 1.0	1	36.0 ± 2.1	-14.3 ± 4.7				89.5	6
	2	20.0 ± 2.7	-21.5 ± 4.8	81.3 ± 8.8			4.7	5
	3	20.0 ± 2.8	-23.0 ± 10.0	81.2 ± 8.8	3.0 ± 18.3		4.6	4
	4	20.0 ± 3.3	-22.9 ± 10.3	80.9 ± 29.8	3.0 ± 18.6	0.5 ± 39.6	4.6	3
392 ± 30,	0	30.9 ± 2.0					80.0	7
σ = 14.0 ± 1.4	1	31.0 ± 2.0	-5.0 ± 4.4				78.7	6
	2	17.5 ± 2.5	-10.5 ± 4.5	69.4 ± 8.1			4.9	5
	3	17.4 ± 2.5	2.5 ± 9.6	70.4 ± 8.1	-26.1± 17.1		2.6	4
	4	15.7 ± 3.0	1.7 ± 9.7	100.0 ± 28.1	-24.4± 17.2	-41.0 ± 37.3	1.4	3
434 ± 26,	0	13.8 ± 1.3					23.9	7
σ = 8.2 ± 0.9	1	13.8 ± 1.3	-0.6 ± 2.7				23.8	6
	2	9.1 ± 1.8	-1.9 ± 2.7	20.0 ± 5.1			8.5	5
	3	9.2 ± 1.8	3.4 ± 6.0	20.0 ± 5.1	-10.4± 10.3		7.5	4
	4	8.4 ± 2.3	3.0 ± 6.0	31.2 ± 19.8	-9.6± 10.4	-14.6 ± 24.9	7.2	3
513 ± 20,	0	11.0 ± 1.2					23.3	7
σ = 7.5 ± 1.1	1	11.6 ± 1.2	-5.1 ± 2.4				18.6	6
	2	8.6 ± 1.6	-7.3 ± 2.5	12.4 ± 4.2			9.8	5
	3	8.3 ± 1.6	-0.8 ± 6.2	13.7 ± 4.3	-11.4± 9.9		8.4	4
	4	6.2 ± 1.8	-2.0 ± 6.2	50.3 ± 16.8	-8.4±10.0	-48.8 ± 21.6	3.3	3

(Units are number of events per bin for 8 bins.

Table VIII. $\Sigma^-\pi^+$ Least-squares fits to the angular distributions

Momentum interval (MeV/c) and cross section (mb)	Order of fit	A coeff	B coeff	C coeff	D coeff	E coeff	χ^2	expected χ^2
293 ± 42, σ = 10.0 ± 1.1	0	22.7 ± 1.7					17.1	7
	1	23.8 ± 1.7	7.9 ± 2.8				8.8	6
	2	28.8 ± 2.8	6.9 ± 2.8	-13.3 ± 5.7			3.4	5
	3	28.9 ± 2.8	8.9 ± 8.3	-13.4 ± 5.7	-3.3 ± 12.6		3.3	4
	4	27.5 ± 3.6	9.9 ± 8.4	1.0 ± 24.7	-4.8 ± 12.8	-17.6 ± 29.3	2.9	3
350 ± 31, σ = 6.9 ± 1.0	0	11.8 ± 1.2					11.4	7
	1	12.8 ± 1.3	5.6 ± 2.0				3.6	6
	2	15.0 ± 2.0	4.9 ± 2.1	-5.8 ± 4.1			1.6	5
	3	14.9 ± 2.0	4.3 ± 5.9	-5.8 ± 4.2	1.0 ± 9.0		1.6	4
	4	14.1 ± 2.6	4.9 ± 6.1	2.8 ± 18.6	.01± 9.3	-10.3 ± 22.0	1.4	3
387 ± 30, σ = 6.0 ± 0.6	0	25.2 ± 1.8					17.3	7
	1	25.8 ± 1.8	6.6 ± 3.0				12.5	6
	2	27.6 ± 2.8	5.9 ± 3.1	-5.2 ± 6.1			11.7	5
	3	27.6 ± 2.8	-17.6 ± 8.6	-2.0 ± 6.2	39.5 ± 13.5		6.3	4
	4	25.5 ± 3.6	-18.0 ± 8.6	22.4 ± 26.6	39.3 ± 13.5	-30.3 ± 32.1	2.4	3
392 ± 30, σ = 8.3 ± 0.9	0	23.0 ± 1.7					9.6	7
	1	23.1 ± 1.7	1.4 ± 3.1				9.4	6
	2	20.6 ± 2.5	1.7 ± 3.1	8.1 ± 6.2			7.7	5
	3	20.6 ± 2.5	-2.9 ± 7.5	8.4 ± 6.2	8.5 ± 12.4		7.2	4
	4	22.4 ± 3.4	-2.8 ± 7.5	-11.1 ± 25.2	8.5 ± 12.4	24.4 ± 30.5	6.6	3
434 ± 26, σ = 6.1 ± 0.7	0	8.4 ± 1.0					31.8	7
	1	8.6 ± 1.0	2.5 ± 2.3				30.5	6
	2	4.7 ± 1.3	5.8 ± 2.4	20.0 ± 4.3			9.3	5
	3	4.7 ± 1.3	-2.1 ± 5.2	20.9 ± 4.4	16.1 ± 9.4		6.4	4
	4	5.0 ± 1.6	-2.6 ± 5.4	15.7 ± 14.4	17.2 ± 9.8	7.5 ± 19.6	6.2	3
513 ± 20, σ = 4.9 ± 0.8	0	5.5 ± 0.8					28.1	7
	1	5.7 ± 0.8	2.4 ± 2.0				26.7	6
	2	2.7 ± 1.0	3.5 ± 2.1	18.5 ± 3.7			1.6	5
	3	2.6 ± 1.0	2.3 ± 4.2	18.8 ± 3.8	2.5 ± 7.8		1.6	4
	4	2.3 ± 1.2	2.5 ± 4.2	24.8 ± 12.7	2.1 ± 7.8	-8.4 ± 17.1	1.3	3

(Units are number of events per bin for 8 bins.)

$\Sigma^{\pm}$-production cross sections for each momentum exposure. The values found are shown in the summary Table A(page vii).

The polarization of the Σ^+ hyperons was observed through the up-down asymmetry of the protons in the decay $\Sigma^+ \rightarrow p + \pi^0$. A normal to the Σ-production plane was defined by the unit vector $\hat{n} = \vec{K}_K \times \vec{K}_\pi / |\vec{K}_K \times \vec{K}_\pi|$, where $\vec{K}_K$ and $\vec{K}_\pi$ are unit vectors in the K^- and π^- directions. The angle ϕ is the angle between $\hat{n}$ and the proton direction $\vec{K}_p$;

$$\cos\phi = \vec{K}_p \cdot \hat{n} \,.$$

The distribution of events versus the pion-production angle θ and the proton angle ϕ may be written

$$\frac{d^2\sigma}{d\cos\theta \, d\cos\phi} = A + B\cos\theta + C\cos^2\theta + \alpha_0 \cos\phi\,(D\sin\theta + E\sin\theta\cos\theta).$$

For the other decay modes, $\Sigma^+ \rightarrow \pi^+ + n$ and $\Sigma^- \rightarrow \pi^- + n$, the asymmetry parameters α_+ and α_- are too small to allow a polarization measurement. Beall et al. have found the value $\alpha_0 = -0.75 \pm .17$ for this parameter in the $\Sigma^+ \rightarrow p + \pi^0$ decay.[7] To measure the coefficients D and E, the average of $\cos\phi$ is calculated:

$$\overline{(\cos\phi)}_\theta = \frac{I(\theta)\int \cos\phi\,(1 + \alpha\,P(\theta)\cos\phi)\,d\cos\phi}{I(\theta)\int (1 + \alpha\,P(\theta)\cos\phi)\,d\cos\phi} \,.$$

Here $I(\theta)$ and $P(\theta)$ are the usual angular distribution and polarization as functions of the production angle θ.

The average of $\cos\phi$ for all production angles measures D only, since the average of $\sin\theta\cos\theta$ vanishes. The E coefficient was measured by subtracting the average of $\cos\phi$ for $\cos\theta$ between -0.95 and -0.30 from the average of $\cos\phi$ for $\cos\theta$ from 0.30 to 0.95. That is

$$\overline{(\cos\phi)}_{E\ \text{term}} = \frac{\begin{bmatrix}\Sigma\cos\phi \\ 0.3 \leq \cos\theta \leq .95\end{bmatrix} - \begin{bmatrix}\Sigma\cos\phi \\ -0.95 \leq \cos\theta \leq -0.3\end{bmatrix}}{\text{Number of events}} \,.$$

The $\sin\theta$ term averages to zero in this case. The interval from 0.95 to 0.30 was chosen to eliminate regions where the polarization is known to be low but where scanning and measuring difficulties are greatest. Including these regions does not alter the results significantly.

D. 0-Prong V Events: $K^- + p \rightarrow \overline{K^0} + n$; $\Sigma^0 + \pi^0$; $\Lambda + \pi^0$; $\Lambda + \pi^0 + \pi^0$

During the many months of event analysis, a logical division of the labor separated the 0-prong V events from the other channels. The analysis of these events presents many difficult and unique problems. Most of this work was done by Dr. Massimiliano Ferro-Luzzi. The author does not intend to claim credit for this work, and hence the following discussion is for completeness only.

There are several interactions leading to the 0-prong V topology. As listed above they are

$$
\begin{array}{l}
K^- + p \rightarrow \overline{K^0} + n;\ \overline{K^0} \rightarrow K_1 \rightarrow \pi^+ + \pi^- , \\
\qquad \left.\begin{array}{l} \rightarrow \Sigma^0 + \pi^0 \\ \rightarrow \Sigma^0 + \pi^0 + \pi^0 \end{array}\right\} \Sigma^0 \rightarrow \Lambda + \gamma;\ \Lambda \rightarrow p + \pi^- \\
\qquad \left.\begin{array}{l} \rightarrow \Lambda + \pi^0 \\ \rightarrow \Lambda + \pi^0 + \pi^0 \end{array}\right\} \Lambda \rightarrow p + \pi^- .
\end{array}
$$

The $\Sigma^0 \pi^0 \pi^0$ cross sections are so small at the energies considered that these events were completely neglected. Although each of the interactions listed leads to the same topological appearance, the $\overline{K^0}n$ events may be easily identified at the scanning table. The π^+ produced in the decay can be distinguished from the protons of a Λ decay because of its lighter ionization. Since measurements on these pions are usually very precise, these events produced fairly tight computer fits. The average fitted K^- momentum error was 4 Mev/c. Nevertheless, in order to obtain detailed cross sections, a computer program was employed which constructed an ideogram of events versus momentum. Each event was assumed to have 1 unit of area under a Gaussian curve which was centered at the fitted momentum and whose width was the fitted error. By this procedure the cross sections to be shown in Section IV were calculated in 10- and 20-Mev/c intervals over the resonance region. No finer division was made, since only a limited number of events was available. The summary Table A displays the average $\overline{K^0}n$ cross section for each of the beam-momentum exposures.

The $\Sigma^0\pi^0$, $\Lambda\pi^0$, and $\Lambda\pi^0\pi^0$ events were easily separated from the $\overline{K^0}n$ events by the presence of the proton in the decay. The separation of one type from another was not so simple. The separation was based on the "missing mass" distribution. The measured incoming K^- momentum was beam-averaged as described in Section A. No events whose measured momentum was 1.5 standard deviations away from the nominal beam momentum were used in the separation. Once the separation was accomplished on the selected events, the entire sample was divided in the same relative fraction. The Λ momentum and energy were determined by the computer program. The square of the missing mass of the unobserved particle or particles was computed by using the expression

$$\mu^2 = (E_{KP} - E_{\Lambda})^2 - (\vec{P}_K - \vec{P}_{\Lambda})^2 ,$$

where μ^2 is the missing mass squared; E_{KP} and E_{Λ} are the K^--p and Λ energies; and $\vec{P}_K$ and $\vec{P}_{\Lambda}$ are the K^- and Λ momenta.

For the $\Lambda\pi^0$ channel μ^2 is uniquely the square of the π^0 mass. These events produce a peak centered around $(M_{\pi^0})^2$ with a roughly Gaussian distribution due to measurement errors. For the $\Lambda\pi^0\pi^0$ events the two π^0 mesons do not have a "unique mass," since they may have a wide range of relative energies. Thus, μ^2 is a distribution which begins at $(2M_{\pi^0})^2$ where the pions are at rest relative to each other. It extends up to a maximum value determined by the total energy available.

For the $\Sigma^0\pi^0$ events μ^2 also has a continuous distribution. The measured V is the Λ resulting from the decay of the $\Sigma^0(\Sigma^0 \rightarrow \Lambda + \gamma)$. Here μ^2 varies because the Λ has different momentum and energy depending on the angle of its decay relative to the Σ^0 direction. The shape of the $\Lambda\pi^0\pi^0$ spectrum might be expected to follow phase-space predictions. The $\Sigma^0\pi^0$ spectrum can be shown to be rectangular.

Figures 18 through 22 show the distribution of μ^2 at each momentum interval, along with the allowed limits for each type of interaction.

The $\Lambda\pi^0$ peak may be reconstructed on the high side by requiring symmetry with the low side. The $\Lambda\pi^0\pi^0$ distribution extends beyond the $\Sigma^0\pi^0$ distribution, which provides a handle for this division. If the $\Lambda\pi^0\pi^0$ events are distributed according to phase-space predictions such a curve may be normalized to those events beyond the $\Sigma^0\pi^0$ limit. All the remaining events are then attributed to the $\Sigma^0\pi^0$ channel. This process was carried out at each of the momentum intervals.

At each of the momentum intervals the $\Lambda^0\pi^0\pi^0$ cross sections obtained in this way were found to violate charge independence when compared with the $\Lambda\pi^+\pi^-$ cross sections. For $\Lambda\pi\pi$ production from the I = 0 state the ratio of the $\Lambda\pi^0\pi^0$ to $\Lambda\pi^+\pi^-$ cross sections is 1/2. From the I = 1 state only $\Lambda\pi^+\pi^-$ can be made. Thus, the maximum allowable cross section for $\Lambda\pi^0\pi^0$ is one-half the $\Lambda\pi^+\pi^-$ cross section. Table VI shows these cross sections.

This violation can probably be attributed to a relatively few poorly measured $\Sigma^0\pi^0$ events which fall below the $\Sigma^0\pi^0$ limit and are thus misidentified as $\Lambda\pi^0\pi^0$. Nevertheless, the persistence of the violation at all momenta indicates that the $\Lambda\pi\pi$ channel proceeds predominantly through the I = 0 state. In order to better estimate the $\Sigma^0\pi^0$ cross section, the $\Lambda\pi^0\pi^0$ cross section subtracted was assumed to be $1/2\ \sigma(\Lambda\pi^+\pi^-)$. The $\Lambda\pi^0\pi^0$ phase-space curves on Figs. 19 through 23 are normalized in this manner.

Since neither the Σ^0 nor the π^0 are seen directly or indirectly in the $\Sigma^0\pi^0$ channel, the angular distribution and polarizations are considerably less reliable than in the other channels. The Σ^0 has a typical momentum of 265 Mev/c in the K^-p center of mass. Hence the Λ resulting from the decay may be expected to deviate from the Σ^0 direction by at most 70/265 radian or approx 15°. All the angular distributions and polarizations recorded for $\Sigma^0\pi^0$ assume the Λ and Σ^0 directions are identical and are thus slightly smeared out. The polarization of the Σ^0 is deduced from the Λ polarization. The relationship is

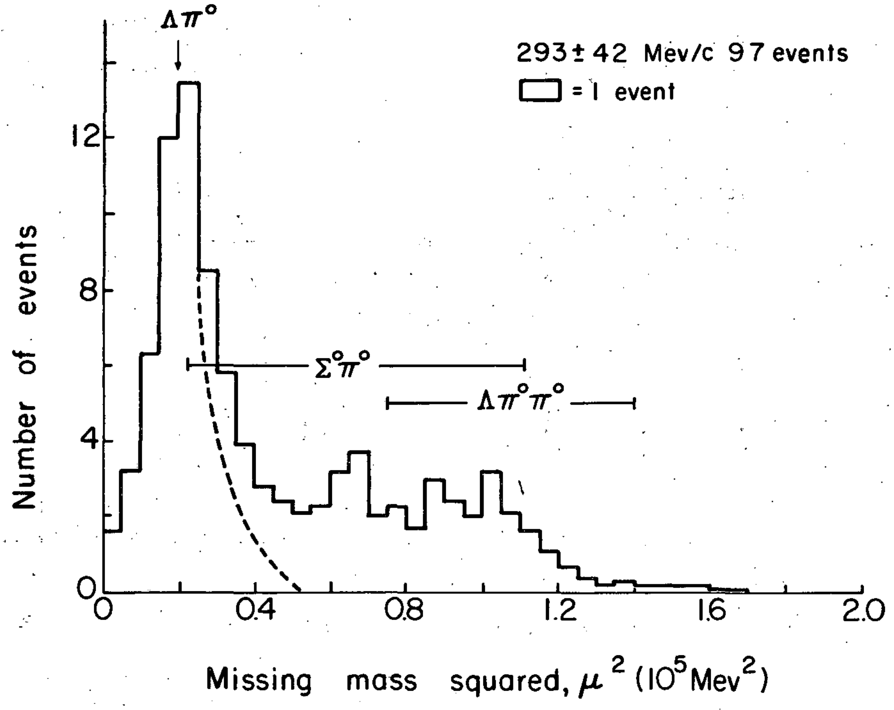

MU-26769

Fig. 18. Missing-mass-squared ideogram at 293 Mev /c K^- momentum for the O-prong V events with an identified Λ. Only events with measured K^- less than 63 Mev /c away from 293 Mev/c were accepted.

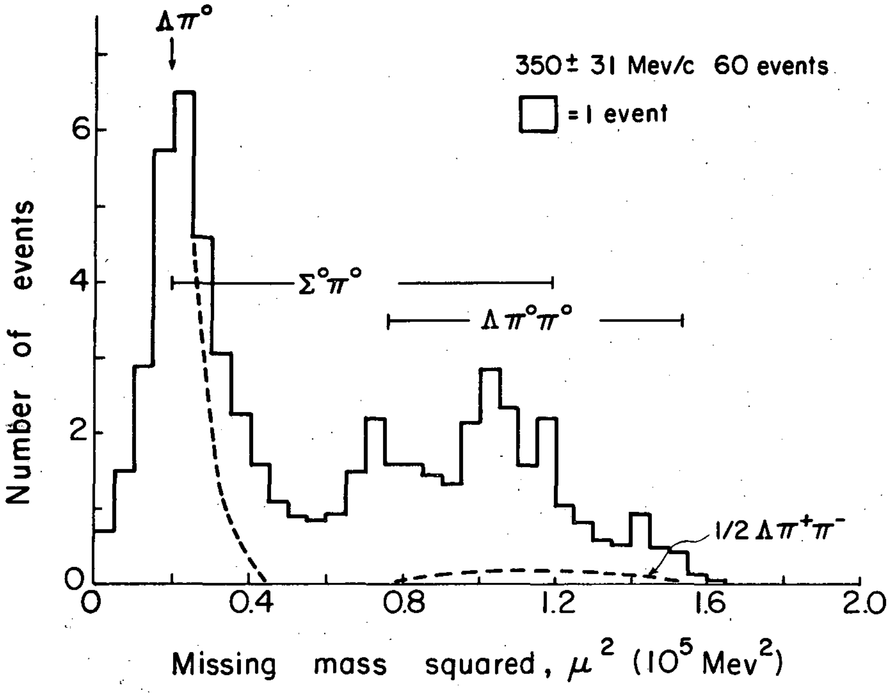

MU-26770

Fig. 19. Missing-mass-squared ideogram at 350 K^- momentum for the O-prong V events. Only events with measured K^- momenta less than 45 Mev /c away from 350 Mev /c were accepted.

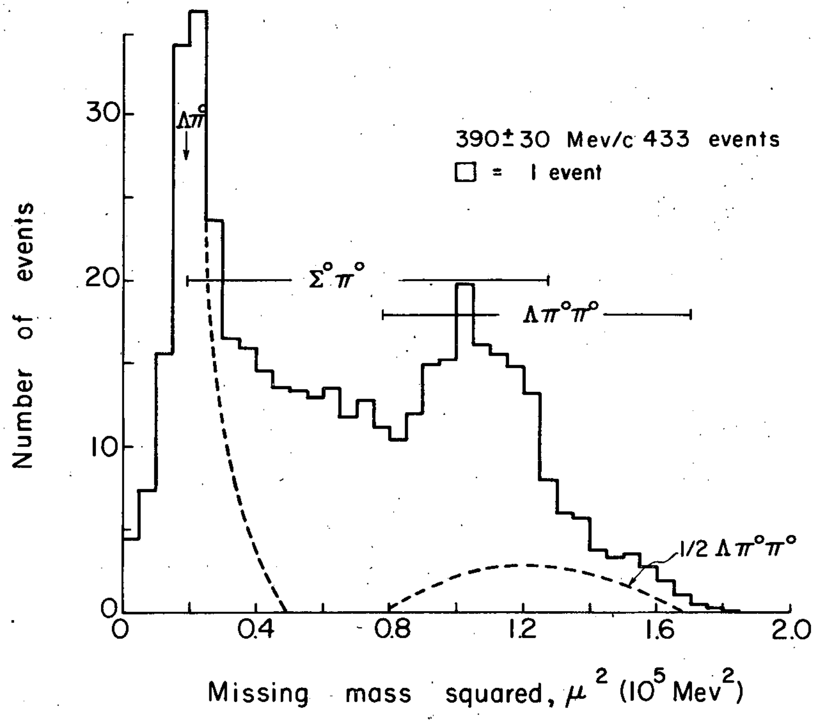

MU-26771

Fig. 20. Missing-mass-squared ideogram at 390 Mev/c K^- momentum for the O-prong V events. Only those events with measured K^- momentum less than 45 Mev/c away from 392 Mev/c were accepted.

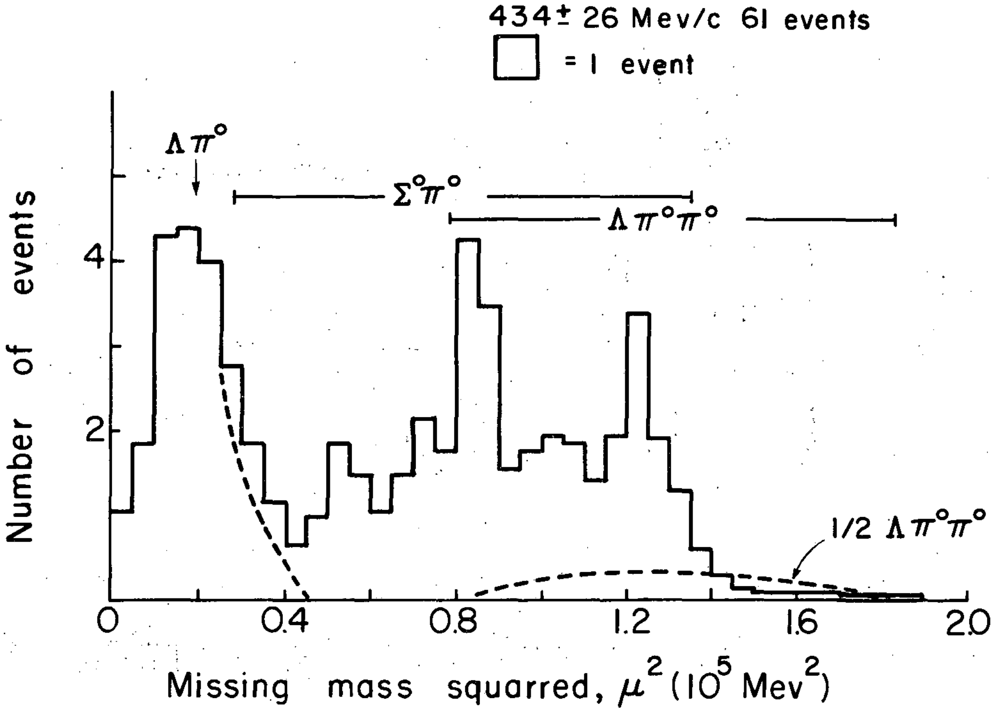

MU-26772

Fig. 21. Missing-mass-squared ideogram at 434 Mev /c K^- momentum for the 0-prong V events. Only those events with measured K^- momentum less than 30 Mev /c away from 434 Mev /c were accepted.

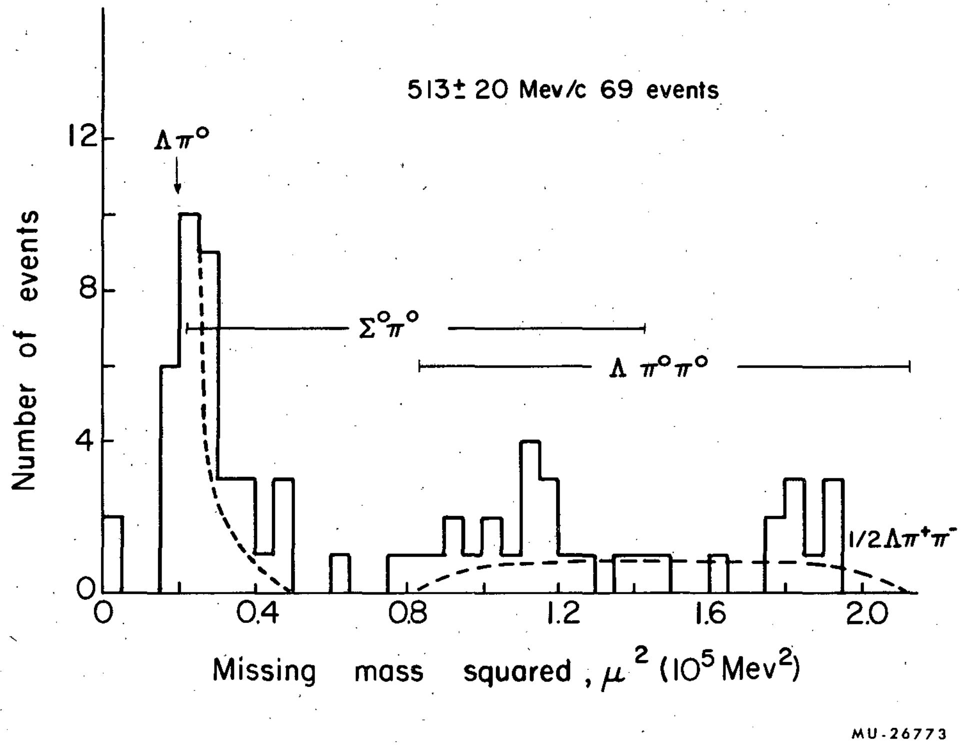

Fig. 22. Missing-mass-squared histogram at 513 Mev/c K^- momentum for the O-prong V events. Only those events with measured K^- momentum less than 30 Mev/c away from 510 Mev/c were accepted.

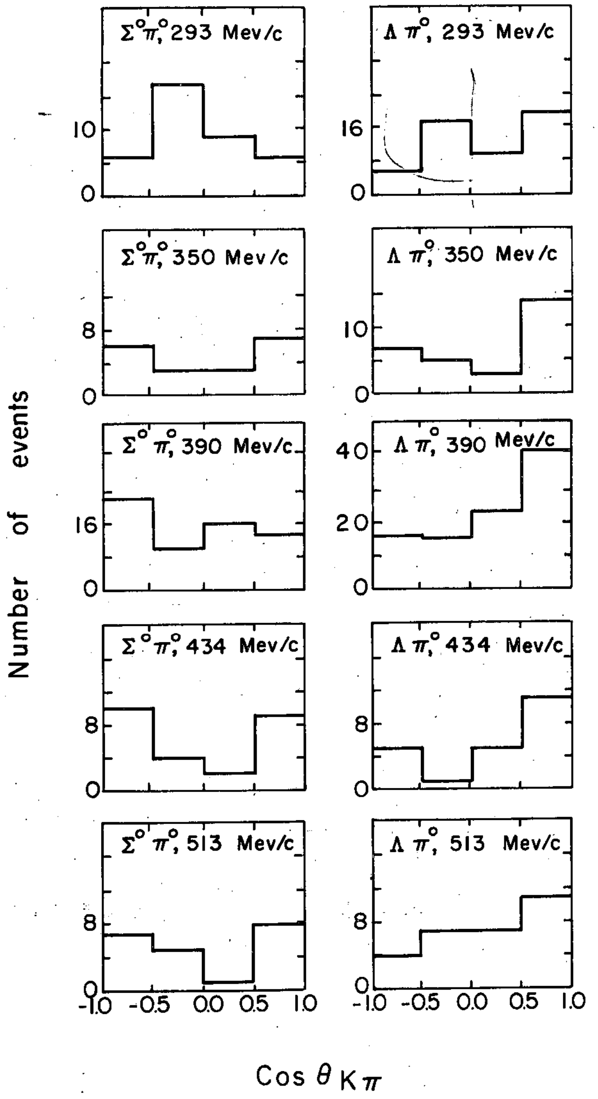

MU-26774

Fig. 23. Angular distributions of $\Sigma^0\pi^0$ and $\Lambda\pi^0$ events. For the $\Sigma^0\pi^0$ events the Σ^0 was assumed to go in the Λ direction in the K^-p center of mass.

$a_\Lambda P_\Lambda = -(1/3) a_\Lambda P_{\Sigma^0}$. Measurement of the Σ^0 polarization is very difficult since the polarization is reduced by the 1/3 factor, in addition to the angle uncertainty. The angular distributions for $\Sigma^0 \pi^0$ and $\Lambda\pi^0$ are shown in Fig. 23.

E. 2-Prong V Events: $K^- + p \rightarrow \Lambda + \pi^+ + \pi^-$

As with the 0-prong V events, the 2-prong V's were analyzed by Dr. Ferro-Luzzi, and this discussion is included for completeness. This class of events, like the τ decay, is usually quite spectacular in the bubble chamber. Since all tracks are measurable directly, such as the π^+ and π^-, or indirectly like the Λ, the computer fit for each event was subject to four constraints. These fits are quite tight, with the average K^- momentum error after fitting only 7 Mev/c. Table IX shows the average cross section for each of the beam momentum settings. To obtain the cross sections in 10-Mev/c bins (discussed in Section IV), all events were fed into the Guassian error ideogram routing used for the $\overline{K^0}n$ events.

For each two $\Lambda\pi^+\pi^-$ events observed there should be one event in which the Λ decays via the neutral mode and is not seen. Such events will be 2-prongs. All 2-prongs were subjected to this hypothesis during the fitting procedure. Since both final-state tracks are pions, candidates for these events may easily be separated from K^-p and π^-p scatterings. Table IX also shows the cross sections obtained from those events in which the Λ decay was not seen. The most troublesome ambiguity in this class of events is the very short Σ^+ or Σ^- productions with subsequent pionic decay. The consistency of the two $\Lambda\pi^+\pi^-$ cross sections (from visible and invisible Λ's) and the lifetime curves for Σ^+ and Σ^- support the assignment and division of 2-prong events into these channels.

Figure 24 shows a Dalitz plot of events in the 390-Mev/c runs. The other intervals have too few events to show any effect that might be present. If the distribution of pion energies were to follow phase-space predictions this plot would be isotropic. The points are certainly consistent with this hypothesis. In addition to the Dalitz plot the effective-

Table IX. Λ-π^+-π^- cross sections from visible and invisible Λ-decay events

Momentum interval (Mev/c)	293 ± 42	350 ± 31	390 ± 30	434 ± 26	513 ± 20
$\sigma(\Lambda\pi^+\pi^-)$; $\Lambda \rightarrow p + \pi^-$ (mb)	0.15 ± 0.10	0.9 ± 0.3	1.6 ± 0.2	1.5 ± 0.4	2.0 ± 0.4
$\sigma(\Lambda\pi^+\pi^-)$; $\Lambda \rightarrow n + \pi^0$ (mb)	--	0.9 ± 0.3	1.3 ± 0.2	0.7 ± 0.3	1.9 ± 0.5

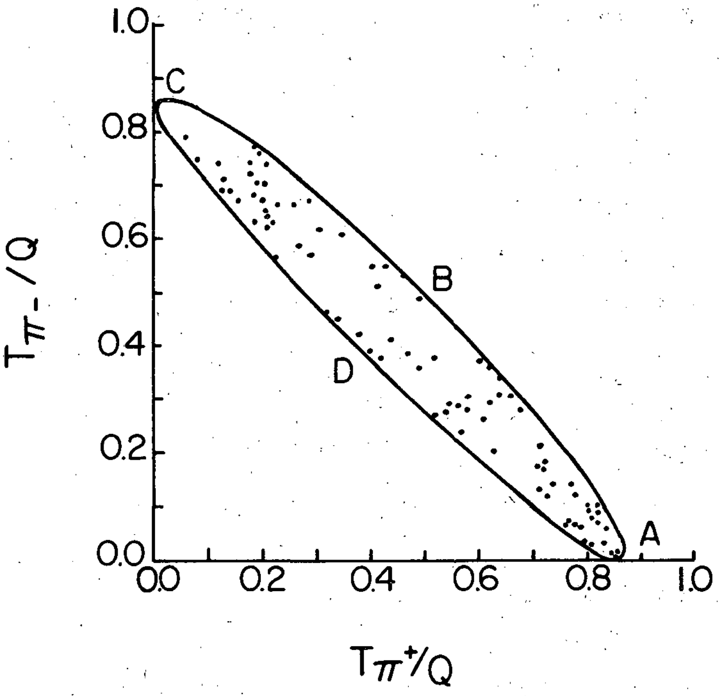

MU-26775

Fig. 24. Dalitz plot of $\Lambda\pi^+\pi^-$ events from the combined 387- and 392-Mev /c runs. 87 events.

mass-squared for several distributions was examined. Figure 25 shows the effective-mass-squared of the $\pi^+\pi^-$ system and the equivalent c.m. kinetic energy distribution of the Λ. These distributions would indicate any deviation from phase-space predictions due to $\pi\pi$ correlations. No such effect is evident. Figure 26 shows the distribution of T_{π^+}/Q and T_{π^-}/Q, where the kinetic energy of each π is divided by the total energy available to normalize out the incident momentum spread. Such a plot should indicate $\pi\Lambda$ correlations such as Y_1^* production.

Although it is tempting to dismiss these distributions as being in accord with phase-space predictions, this is probably not quite correct. As mentioned in Section III-D, the $\Lambda\pi\pi$ channel proceeds largely from the K^-p $I = 0$ $D_{3/2}$ state. Consider the two-pion system and the angular momentum state of the Λ relative to this system. Bose statistics require the $\pi\pi$ system to be an S or a D state, since the $I = 0$ state is symmetric. If odd $Kp\Lambda$ parity is assumed the Λ-$(\pi^+\pi^-)$ state is then $P_{3/2}$ for the $(\pi^+\pi^-)$ S state and $P_{1/2}$ or $P_{3/2}$ for the $(\pi^+\pi^-)$ D state. The Λ-$(\pi^+\pi^-)$ state must be a P state. High Λ energies will be favored. If the $Kp\Lambda$ parity were even the Λ-$(\pi^+\pi^-)$ state would have to be a D state, favoring high Λ energies even further.

Figure 27 shows the angular distribution of the Λ in the K^-p center of mass. For pure $P_{3/2}$ (or $D_{3/2}$) this distribution should be $1+3\cos^2\theta$. There are two explanations for the missing high-energy Λ enhancement. First, such an effect may indeed be present, but a substantial background from other K^-p states obscures the picture. Second, there may be still another effect present enhancing the low-energy Λ's. On Fig. 25b the dashed curve represents an artist's conception of the p-wave T_Λ distribution. The alternate dash-dot curve at low Λ energies represents a $\pi^+\pi^-$ interaction in the $I = 0$, S, or D state. Evidence for such a state at approximately this energy has recently been found.[8] In either case the net effect is to reproduce a phase-space-like distribution. The use of a phase-space curve in the $\Sigma^0\pi^0$ - $\Lambda\pi^0\pi^0$ separation of Section III-D is then justified.

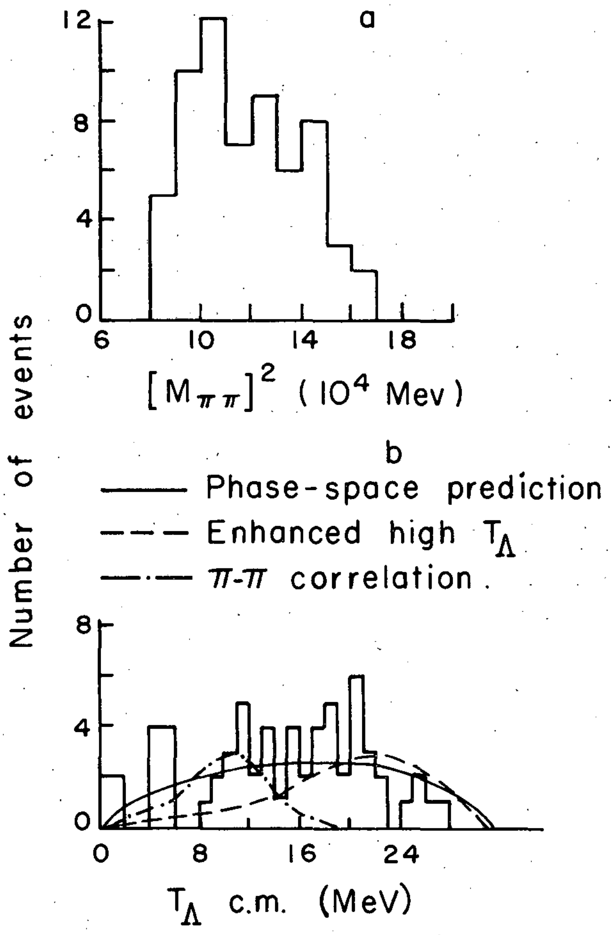

MU-27009

Fig. 25. a. Effective mass squared of the π^+ and π^- from the $\Lambda\pi^+\pi^-$ events in the 387- and 392-Mev/c runs.

b. Distributions of the center-of-mass kinetic energy of the Λ for the $\Lambda\pi^+\pi^-$ events in the 387- and 392-Mev/c runs.

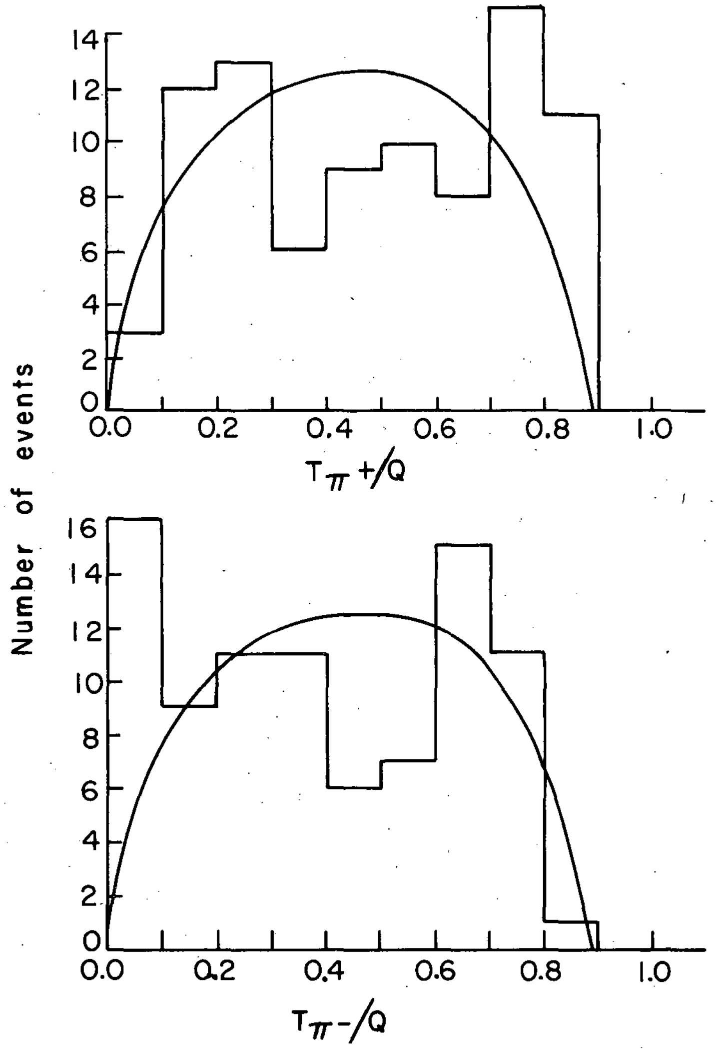

MU-27008

Fig. 26. Distributions of the center-of-mass kinetic energy of the π^+ and π^- for the $\Lambda\pi^+\pi^-$ events in the 387- and 392-Mev/c runs. These are projections on the axes of the Dalitz plot shown in Fig. 24.

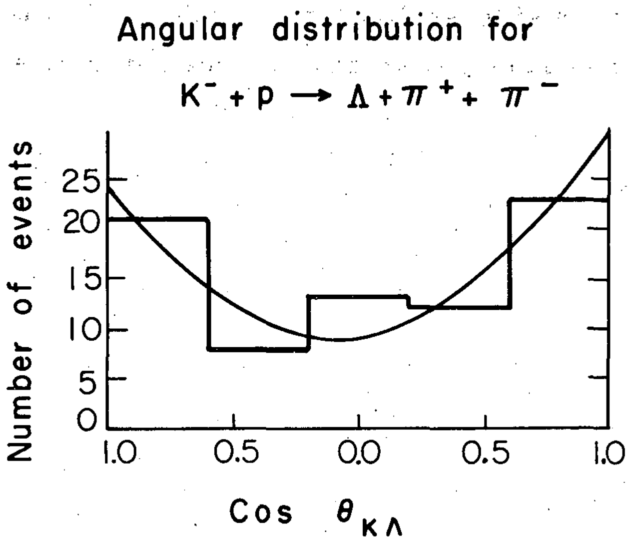

MU-27016

Fig. 27. Angular distribution of the Λ's for the $K^- + p \rightarrow \Lambda + \pi^+ + \pi^-$ events in the 387- and 392-Mev/c runs. The curve shown is the least-squares fit:

$$\frac{d\sigma}{d\Omega} = (9.0 \pm 2.3) + (2.9 \pm 3.3) \cos\theta_{K\Lambda} + (18.5 \pm 6.9) \cos^2\theta_{K\Lambda} .$$

The χ^2 for this fit was 2.7 where 2 was the expected value.

At this point the question of Y_1^* production might be considered. The threshold for Y_1^* production is 410 Mev/c K^- laboratory momentum, which is nearly in the center of the region considered here. We might ask how many of the events can be attributed to Y_1^* production. On the Dalitz plot the Y_1^* will appear as bands parallel to the axes at points A and C. Near threshold the simple band structure should not yet be distorted by interference effects. The data do not prohibit or demand Y_1^* production. The question of Y_1^* production in this region and at higher energies is considered in detail in the Ph. D. thesis of J. Peter Berge.[9] The reader is referred to that source for further discussion.

IV. INTERPRETING THE RESULTS

A. Resonance Hypothesis

In Section III the emphasis is on results and possible biases for each of the different channels. The results were averaged over the natural momentum spread of the six momentum exposures making up the experiment. In the discussions of each channel the determination of the incident K^- momentum was indicated to be sufficiently precise to merit a more detailed examination of the momentum dependence of the data. In most cases 20-Mev/c momentum divisions were justified provided there were enough events to still give reasonable statistics. Near 390 Mev/c the $\Lambda\pi^+\pi^-$ and $\overline{K}^0$ n events were further subdivided into 10-Mev/c bins. Both these types of events are so well determined that an even finer division would be justified were there a sufficient number of events. Figures 28 through 32 show the cross sections derived from the combined data as a function of K^- lab momentum.

It is obvious from these curves and also from Table A that some sort of anomaly occurs near 400 Mev/c. Not only are significant bumps found in the $\overline{K}^0$n, $\Sigma^+\pi^-$, $\Sigma^-\pi^+$, and $\Lambda\pi^+\pi^-$ channels, but a marked variation in the differential cross sections for K^-p also occurs. An explanation of the effects seen is hypothesized to be a resonant state near 400 Mev/c K^- momentum. This resonant state would have components of Kp, $\Sigma\pi$, and $\Lambda\pi\pi$. Production of this state would enhance each of these channels in proportion to the respective decay branching ratio. The principal task in the following discussion is to determine the properties of both this state and the nonresonant states that make up the background upon which the resonance is superimposed.

Some of the properties of the resonant state may be crudely determined without further analysis. Each of the bumps in the different cross-section curves is centered at approximately 390 Mev/c lab momentum. The center-of-mass energy at that point and hence the mass of the resonant state is approx 1520 Mev/c. The width of the bumps is about 40 Mev/c, which implies an energy half-width of approx 10 Mev for the resonance.

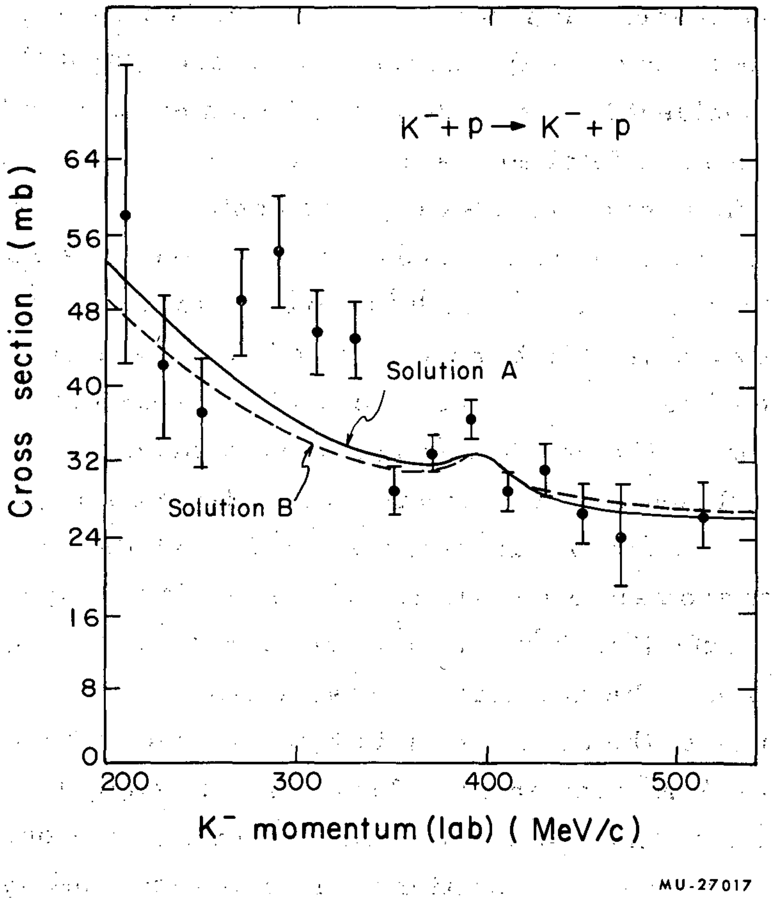

Fig. 28. K⁻ + p → K⁻ + p elastic cross section versus K⁻ laboratory momentum. The points are from the merged 293- through 434-Mev /c runs. The curves are solutions A and B of Section IV-C.

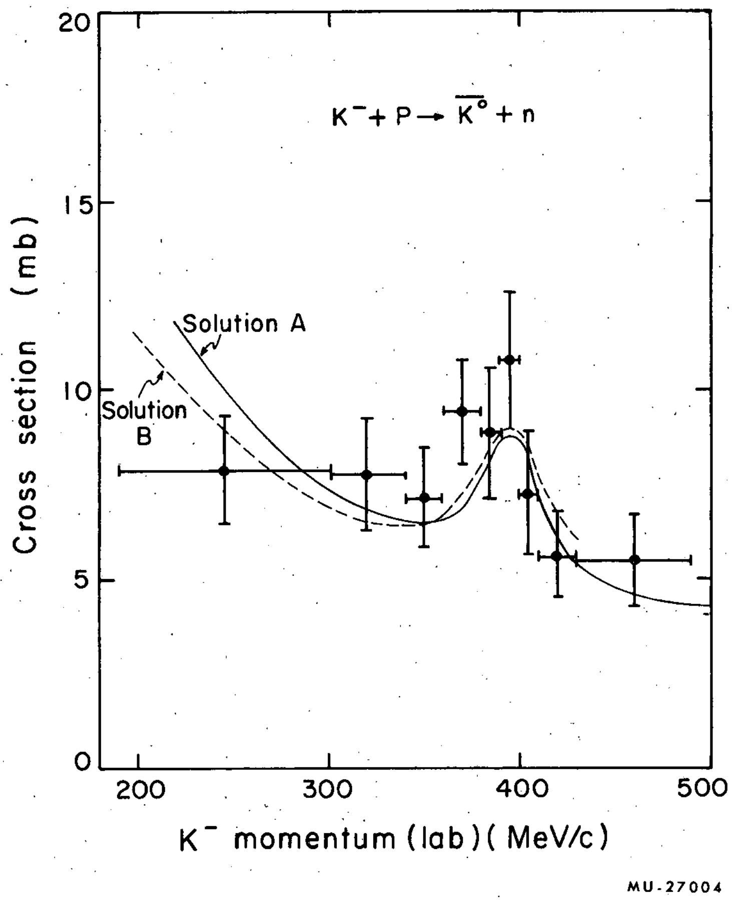

Fig. 29. $K^- + p \rightarrow \overline{K^0} + n$ charge-exchange cross section versus K^- laboratory momentum. The points are from the merged 293- through 434-Mev /c runs. The curves are solutions A and B of Section IV-C.

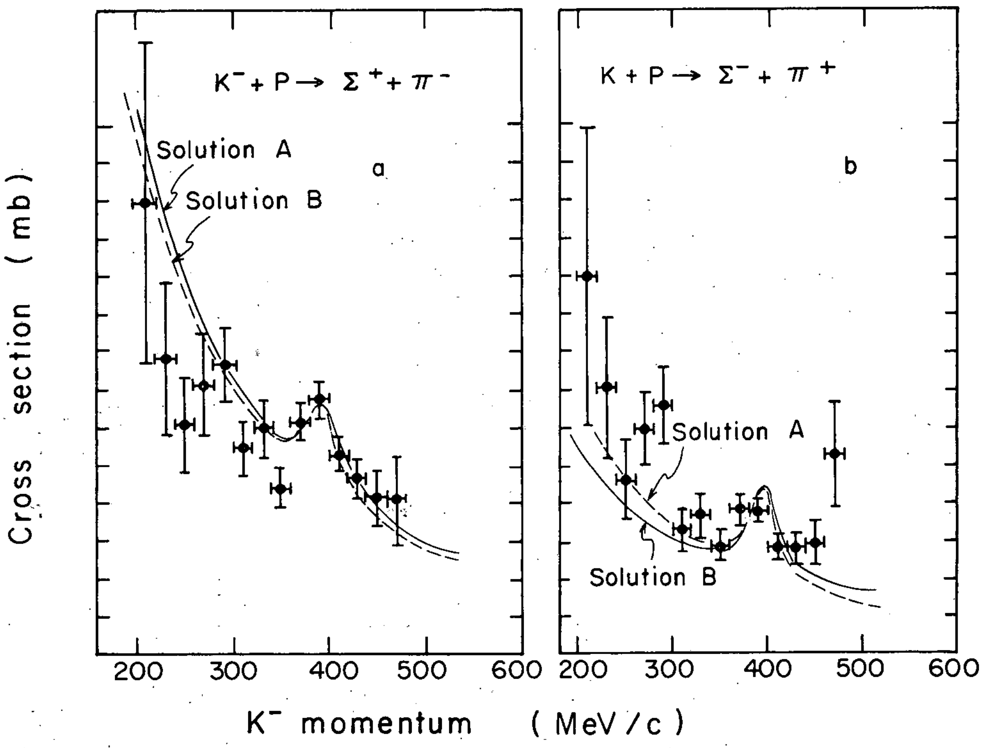

MU-27019

Fig. 30. $K^- + p \rightarrow \Sigma^+ + \pi^-$ and $K^- + p \rightarrow \Sigma^- + \pi^+$ cross sections versus K^- laboratory momentum. The points are from the merged 293- through 434-Mev/c runs. The curves are solutions A and B of Section IV-C.

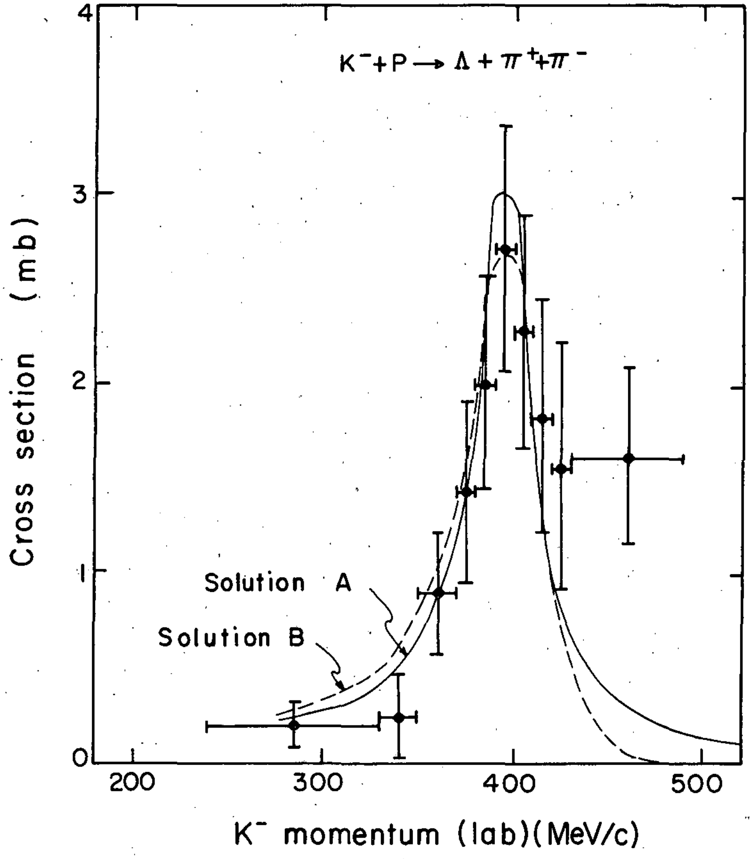

MU-27020

Fig. 31. $K^- + p \rightarrow \Lambda + \pi^+ + \pi^-$ cross sections versus K^- laboratory momentum. The points are from the merged 293- through 470-Mev/c runs. The curves are solutions A and B of Section IV-C.

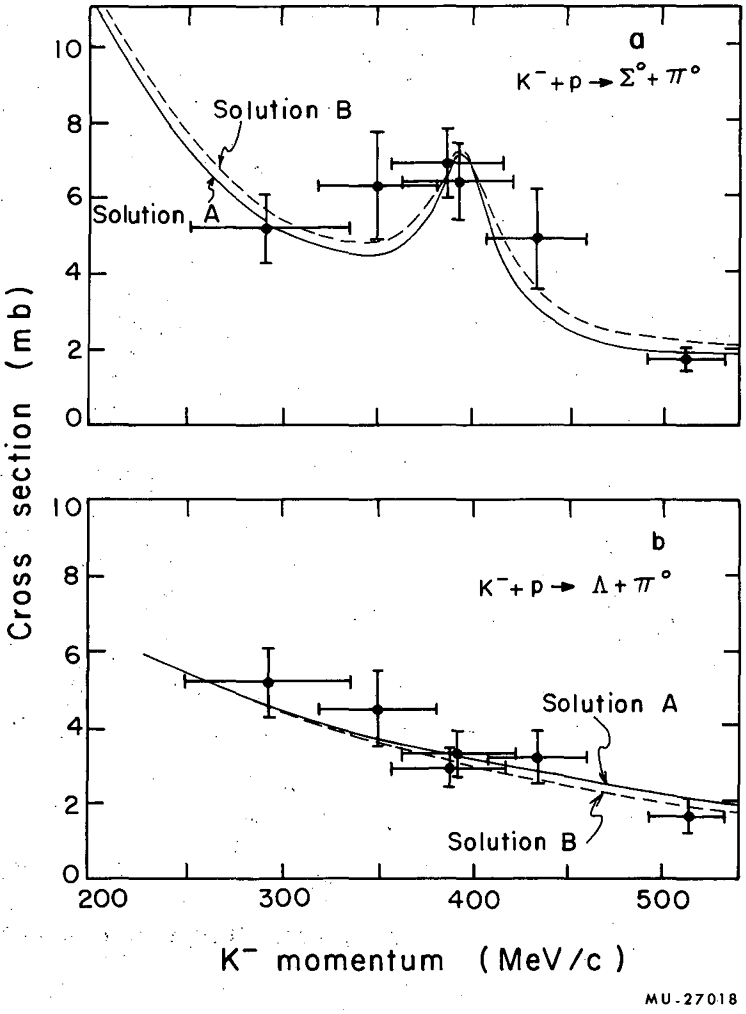

Fig. 32. $K^- + p \rightarrow \Sigma^0 + \pi^0$ and $K^- + p \rightarrow \Lambda + \pi^0$ cross sections versus K^- laboratory momentum. The points are averaged over the natural momentum spread of each runs. The Σ^0 was assumed to go in the Λ direction in the K^-p center of mass. The curves are solutions A and B of Section IV-C.

To determine the resonant isotopic spin the $\Sigma^0\pi^0$ and $\Lambda\pi^0$ channels should be examined. The $\Sigma^0\pi^0$ is entirely $I = 0$, while the $\Lambda\pi^0$ is entirely $I = 1$. Neither of these channels can be accurately subdivided into small momentum intervals. The incident K^- momentum was determined almost completely by a direct curvature measurement which does not allow such a division. More importantly, the difficult separation problem does not allow an accurate separation into $\Sigma^0\pi^0$ or $\Lambda\pi^0$ event by event. This separation was made within each of the momentum settings on a selected sample of events (Section III-D) and the relative fractions were applied to the whole sample.

For the $\Sigma^0\pi^0$ events the cross sections are certainly consistent with a peaking which appears more as a shelf on the falling nonresonant cross section. No deviation at all from a smooth fall in the $\Lambda\pi^0$ cross section is seen (Fig. 32). As indicated previously, the $\Lambda\pi\pi$ channel proceeds largely through the $I = 0$ state and the $\Lambda\pi^+\pi^-$ show a very sharp peak. If the I spin were 1 the $\Lambda\pi^0\pi^0$ channel (pure $I = 0$) would not be fed through the resonant state. The population of this channel might then be attributed to a misinterpretation of $\Sigma^0\pi^0$ events. But this would further peak the $\Sigma^0\pi^0$ cross section, which is pure $I = 0$. The isotopic spin is then $I = 0$.

Additional support for $I = 0$ appears in the differential cross sections for $\Lambda\pi^0$ and $\Sigma^0\pi^0$. Figure 23 shows the definite presence of $\cos^2\theta$ terms changing with momentum for $\Sigma^0\pi^0$, while $\Lambda\pi^0$ is quite consistent with little or no $\cos^2\theta$ terms up to 513 Mev/c.

The analysis of the angular distributions indicates the spin of the resonant state. Tables III, VII, and VIII show no indication that powers of $\cos\theta$ higher than 2 are required to fit the differential cross sections. This indicates a resonant spin of $J = 3/2$. Higher J would be revealed by the presence of higher-power terms of $\cos\theta$ in at least one of the distributions. Lower J would not produce the large $\cos^2\theta$ terms observed. Spin 3/2 is strongly indicated. The $J = 5/2$ possibility is discussed more completely later.

The only quantum number still to be determined is the parity. The parity of the resonant state may be defined by the K^-p state that feeds it. To determine the K^-p orbital angular momentum state, the nonresonant states must also be examined. The interference between the resonant state and background state or states should show up in the angular distribution, although not in the total cross sections. Figures 33 and 34 show the coefficients A, B, C for the angular distributions in the elastic-scattering and charge-exchange channels. A, B, and C are defined by the expression

$$\frac{d\sigma}{d\Omega} = \frac{\pi \lambda\!\!\!^{-}{}^2}{4\pi}[A + B \cos\theta + C \cos^2\theta] .$$

In both channels A dips while C peaks near the resonant energy. This would occur if the K^-p resonant state were to interfere with a nonresonant state of the same parity. Of course, there may be more than one nonresonant state. The different sizes of the peaks in the K^-p and $\overline{K}^0n$ channels also indicate that an interference phenomenon is responsible. The K^-p peak is roughly twice the $\overline{K}^0n$ peak, which would be very difficult to reproduce with a single resonant amplitude. The s-wave contributions in K^-p and $\overline{K}^0n$ are well known to differ considerably, and an s-wave interference could easily account for the difference in size of the peaks.

The B coefficient arises from interference between states of opposite parity. Since this term is relatively small, one nonresonant state (with the same parity as the resonant state) is probably dominant, with a small admixture of an opposite-parity state.

At lower momenta, up to 250 Mev/c, s waves are known to be strongly dominant in the $\overline{K}N$ channel. Humphrey and Ross have derived two sets of zero-effective-range parameters which describe all the low-energy data.[6,10] Although the zero-effective-range hypothesis may not be expected a priori to remain valid at 400 Mev/c, and extrapolation to this region should not be too far wrong. Figure 35 shows the extrapolation of the two solutions to the 400-Mev/c region. In both cases sizeable s-wave cross sections are still present.

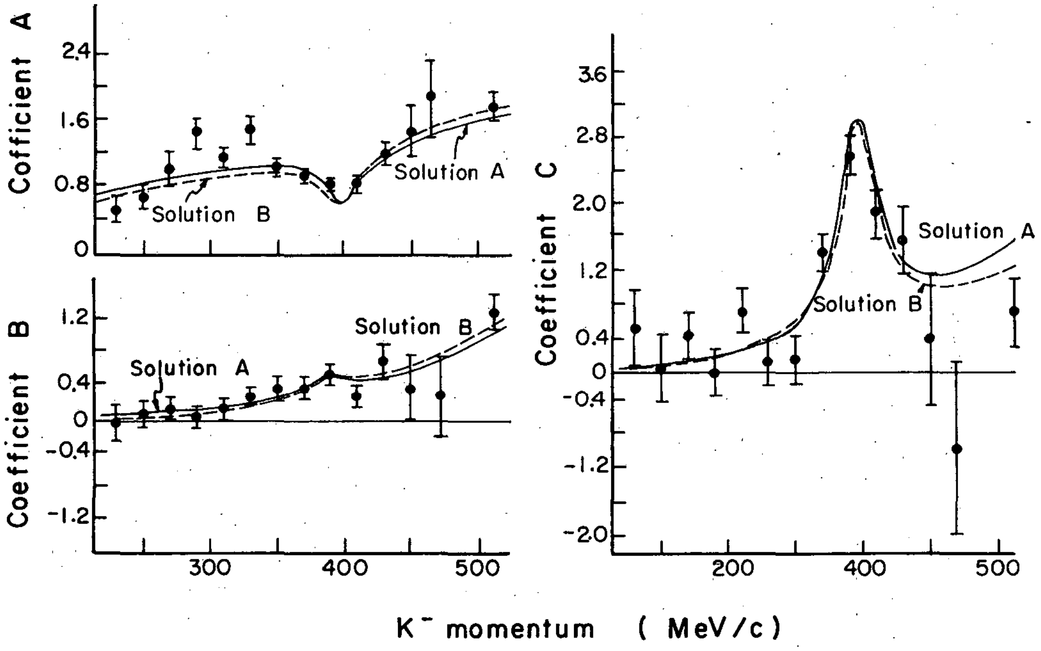

MU-26889

Fig. 33. Momentum dependence of the coefficients A, B, and C for $K^- + p \rightarrow K^- + p$ elastic scattering. Where

$$\frac{d\sigma}{d\Omega} = \frac{\pi \bar{\lambda}^2}{4\pi} [A + B \cos\theta_{KK} + C \cos^2\theta_{KK}] .$$

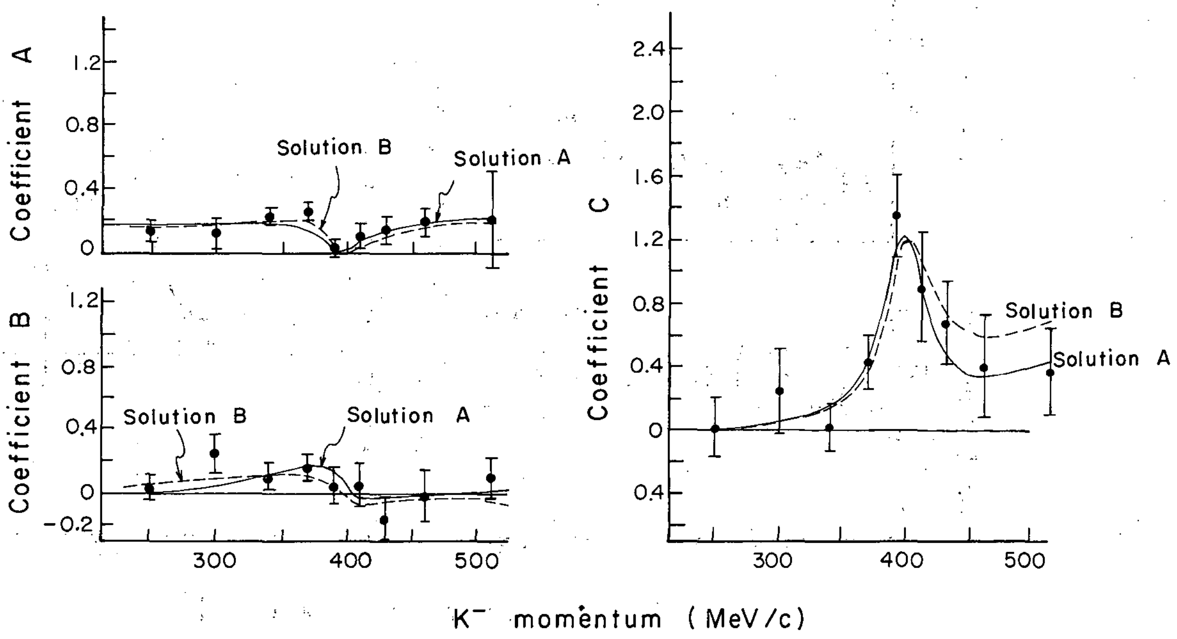

Fig. 34. Momentum dependence of the coefficients A, B, and C for $K^- + p \rightarrow \overline{K^0} + n$ charge-exchange scattering. Where $\frac{d\sigma}{d\Omega} = \frac{\pi \lambda^2}{4\pi}$ $[A + B \cos\theta_{KK} + C \cos^2\theta_{KK}]$.

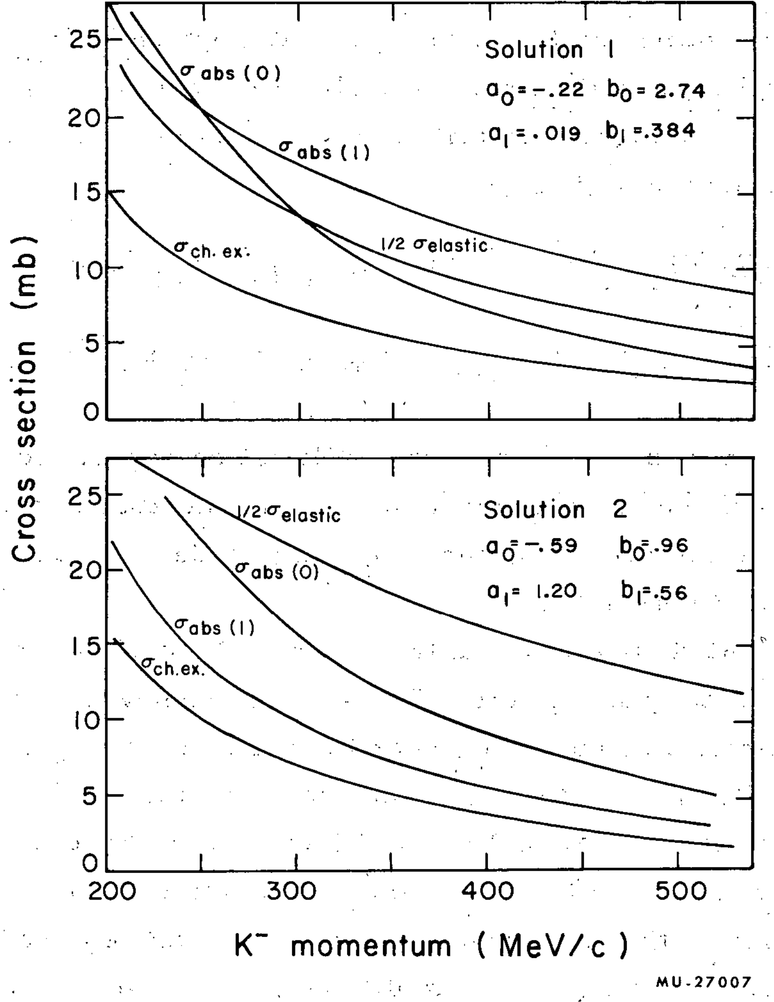

Fig. 35. Extrapolation of the s-wave cross sections using the Humphrey-Ross solutions 1 and 2. Charge-dependent corrections have been ignored. These corrections are negligible near 400 Mev/c.

It seems reasonable, then, to assume that the dominant nonresonant $\overline{K}N$ state at 400 Mev/c is still s wave. The spin of the resonance has been established to be J = 3/2, and we wish to know whether $P_{3/2}$ or $D_{3/2}$ is the proper choice. The angular distributions indicate a resonance with the same parity as the $S_{1/2}$ state, which is $D_{3/2}$. The opposite-parity $P_{3/2}$ and $P_{1/2}$ backgrounds are presumably small.

The angular distribution in terms of all of the amplitudes up to J = 3/2 may be written

$$\frac{d\sigma}{d\Omega} = \frac{\pi \bar{\lambda}^2}{4\pi} \Big\{ [|P_1 - P_3|^2 + |S - D_3|^2] + [2\mathrm{Re}(P_1 - P_3)^*(S + 2D_3) + 6\mathrm{Re}(S - D_3)^* P_3] \cos\theta$$
$$+ [|S + 2D_3|^2 - |S - D_3|^2 + |P_1 + 2P_3|^2 - |P_1 - P_3|^2] \cos^2\theta + [18\,\mathrm{Re}P_3^* D_3] \cos^3\theta$$

Henceforth the $\pi \bar{\lambda}^2/4\pi$ factor will not be expressed although the amplitudes will be in units corresponding to the above equation. Since no $\cos^3\theta$ terms are seen, the $P_{3/2}$ amplitude must be small and will be neglected until later.

At this point a fairly simple picture of the region seems to fit all the data qualitatively. The s waves of lower momenta are still large, with small amounts of $P_{1/2}$ and possibly some $P_{3/2}$ entering slowly. In the $D_{3/2}$, I = 0 state a resonance occurs near 390 Mev/c with components of Kp, $\Sigma\pi$, and $\Lambda\pi\pi$. The mass is about 1520 Mev with a half-width of approx 10 Mev. A more quantitative but preliminary determination of the amplitudes involved was carried out in the following manner.[11] The s-wave amplitudes were first approximated by using the Humphrey-Ross extrapolated values as a guide. In the $D_{3/2}$, I = 0 state a Breit-Wigner form for the resonant amplitude $D = \frac{2x}{\epsilon - i}$ was added, where $x = \frac{\Gamma_{\overline{K}N}}{\Gamma}$, $\epsilon = \frac{2(E_R - E)}{\Gamma}$. Here $\Gamma_{\overline{K}N}$ is the partial width for decay back into the $\overline{K}N$ channel, Γ is the total width $\Gamma = \Gamma_{\overline{K}N} + \Gamma_{\Sigma\pi} + \Gamma_{\Lambda\pi\pi}$, E is the total center-of-mass energy, and E_R is the resonant energy. From the total cross sections all the parameters were determined, thus leaving the angular distributions as a consistency check. Figures 33 and 34, which correspond to Fig. 2a, b of

Reference 11, show the excellent agreement with this simple model. The fitting process in this work was entirely by hand. The curves shown on Figs 33 and 34 are actually the solutions discussed in section IV-C and not the hand-analysis curves. By use of a very informative graphical technique this analysis was extended to the $\Sigma\pi$ channels.[12] Figure 36 shows a typical graphical picture of the s- and d-wave relationships. An angular distribution may be written for s and p waves,

$$\frac{d\sigma}{d\Omega} = \left| S + (2P_3 + P_1) \cos\theta \right|^2 + \left| (P_3 - P_1) \sin\theta \right|^2 .$$

Applying a Minami transformation $S \rightarrow P_1$, $P_1 \rightarrow S$, $P_3 \rightarrow D_3$, one has

$$\frac{d\sigma}{d\Omega} = \left| P + (S + 2D) \cos\theta \right|^2 + \left| (S - D) \sin\theta \right|^2 .$$

The Breit-Wigner d-wave amplitude may easily be shown to be a circle in the complex plane. The quantities $S + 2D$ and $S - D$ may be constructed on the graph, thus yielding the two principal terms in the angular distributions. The positions on the circles are determined by the energy, whereas a clockwise direction of rotation is required by the Wigner theorem.[13] This theorem states that the phase shift must increase with energy when going through a resonance and decrease only in very special circumstances.

The magnitudes for each amplitude were determined from the cross sections observed. There still remains a freedom of orientation for the s-wave amplitude relative to the d-wave amplitude for each absorbtive channel. This orientation was determined solely by the angular distributions, which leaves the polarizations completely predicted.

Measurement of the Σ^+ polarization not only fits the predicted curve extremely well, but also leads to a determination of the $Kp\Sigma$ parity. The arguments leading to this determination are considered in the next section. The results of the hand analysis described (which also introduced small $P_{1/2}$ amplitudes) were so successful that a more elaborate search procedure using the IBM 7090 was undertaken. The formulation of this problem and the results are discussed in Section C.

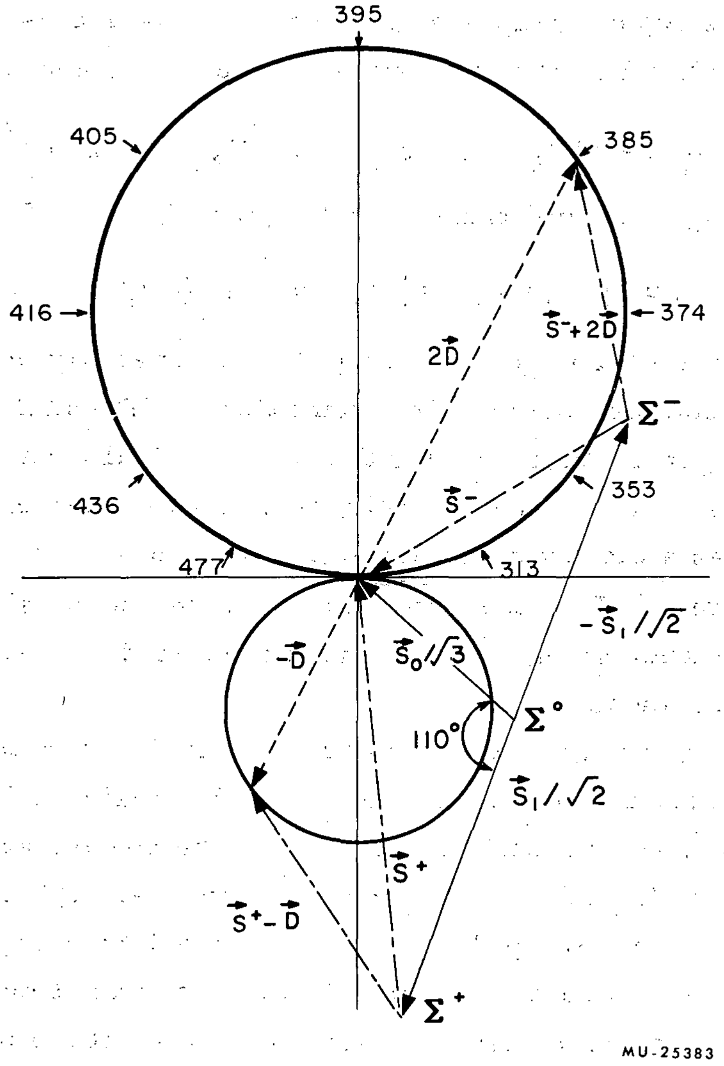

Fig. 36. Graphic construction of the S+2D and S-D amplitudes for the $\Sigma\pi$ channels. The orientation of the amplitude D is indicated for several K^- momenta. The s-wave amplitudes vary in magnitude according to the zero-effective-range prescription. The s-wave phases are assumed constant. The zero-effective-range variation in the s-wave relative phase is less than 5° over the region of the data.

B. The KpΣ Parity

In the preceding section the Σ-π final orbital angular momentum state was assumed to be the same as the initial Kp state feeding it. This, of course, implies that the intrinsic parity of the K^-p system is identical to that of the $\Sigma\pi$ system or odd KpΣ relative parity. To justify this, consider all possibilities open to the $K^- + p \rightarrow \Sigma + \pi$ reaction amplitude M. Specifically consider the $J = 3/2$ case. Both the K^-p and the $\Sigma\pi$ states may be either $P_{3/2}$ or $D_{3/2}$. Depending on the parity, the K^-p, $P_{3/2}$ state may feed either the $\Sigma\pi$ $P_{3/2}$ or $D_{3/2}$, but not both. Similarly, the $D_{3/2}$, K^-p state may go to either the $P_{3/2}$ $\Sigma\pi$ or $D_{3/2}$ $\Sigma\pi$ state. This is a generalized fourfold Minami ambiguity. The operator M may be constructed for each of these cases as follows. Define M for the $P_{3/2}$, $P_{1/2}$, $S_{1/2}$ $\Sigma\pi$ final state by

$$M = A(\theta) + B(\theta)\,\vec{\sigma}\cdot\hat{n},$$

where $\hat{n} = \dfrac{\vec{K}_{in}\times\vec{K}_{out}}{|\vec{K}_{in}\times\vec{K}_{out}|}$ and $\vec{K}_{in}$ and $\vec{K}_{out}$ are unit vectors in incoming K^- and outgoing π^- directions, and

$$A(\theta) = \frac{1}{2K}\left[S + (2P_3 + P_1)\cos\theta\right]\ ;\ B(\theta) = \frac{i}{2K}\left[(P_3 - P_1)\sin\theta\right).$$

To obtain M for the $D_{3/2}$, $S_{1/2}$, $P_{1/2}$ final state, apply the Minami transformation $M \rightarrow \vec{\sigma}\cdot\vec{K}_{out}M$. To change the parity of the initial K^-p state only, use the transformation $M \rightarrow M\vec{\sigma}\cdot\vec{K}_{in}$. To change both parities use $M \rightarrow \vec{\sigma}\cdot\vec{K}_{out}M\vec{\sigma}\cdot\vec{K}_{in}$. Table X lists these possibilities. The angular distributions are derived from M through the relation

$$I'(\theta) = \frac{d\sigma}{d\Omega} = \langle\psi_f|\psi_f\rangle,$$

$$I'(\theta)\vec{P}(\theta) = \langle\psi_f|\vec{\sigma}\ \psi_f\rangle,$$

where

$$\psi_f = M\psi_i .$$

Here ψ_f and ψ_i are the final- and initial-state wave functions including spin. Table X lists the expressions for $I'(\theta)$ in terms of $I(\theta)$ and $\vec{P}_{in}$, where $I(\theta)$ ($I(\theta) = |A|^2 + |B|^2$) is the angular distribution, assuming zero initial proton polarization and $\vec{P}_{in}$ is the initial proton polarization. For the experiment considered here $\vec{P}_{in}$ was zero, hence $I'(\theta) = I(\theta)$. The arguments of Section IV-A utilize the interference with the known s-wave background to restrict the initial $K^- p$ state to $D_{3/2}$. Thus, the knowledge of the background state through its interference with the resonant state reduces the fourfold ambiguity to a twofold ambiguity (lines 2 and 3 are still allowed). The angular distributions are identical for these cases, but the polarizations are of opposite sign. The problem is reduced to determining the absolute sign of the polarization.

To measure the absolute sign of the polarization two things must be determined. First, since the polarization is measured through the asymmetry of the $\Sigma^+ \rightarrow p + \pi^0$ decay, the sign of the decay asymmetry parameter α_0 must be found. This parameter (the proton helicity) has recently been found to be $-0.75 \pm .17$.[7] The second requirement is the phase of A^*B. Only $|A|^2$ and $|B|^2$ can be measured from the angular distributions. However, the expression for $I(\theta)\ P(\theta)$ corresponding to lines 2 and 3 of Table IX are:

line 2: $$I(\theta)\ P(\theta) = [2\mathrm{Im}(S - D_3)^* (P_1 - P_3) \sin\theta] + [6\mathrm{Im}(S^* D_3 - P_1^* P_3) \sin\theta \cos\theta]$$

$P_1SD_3 \rightarrow P_1SD_3$

line 3: $$I(\theta) P(\theta) = -[2\mathrm{Im}(S - D_3)^* (P_1 - P_3) \sin\theta] - [6\mathrm{Im}(S^* D_3 - P_1^* P_3) \sin\theta \cos\theta]$$

$P_1SD_3 \rightarrow SP_1P_3$

The $\sin\theta$ term is generated by both pd and ps interference, both of which are expected to be small. The most striking difference is found in the $\sin\theta \cos\theta$ term, where a marked momentum dependence should be observed. The relative phase of $D_{3/2}$ and S must be determined. It is impossible to determine such a phase by any one observation, but by invoking the Wigner theorem[13] the change in this phase as the momentum increases is determined.

The phase between the s-wave and d-wave amplitudes was determined by examination of the "A" and "C" terms of the angular distributions. The $\sin\theta\cos\theta$ polarization term was then predicted for all energies in the resonance region. The expressions for A anc C show the dependence on this phase:

$$A = |S|^2 + |D_3|^2 - 2\mathrm{Re}S^*D \;\; ; \;\; C = 3|D_3|^2 + 6\,\mathrm{Re}S^*D.$$

Figures 37 and 38 show both the $\sin\theta\cos\theta$ and $\sin\theta$ polarizations versus momentum for the combined data. The curves for even and odd $Kp\Sigma$ parity are essentially reflections of each other. Section C describes two sets of parameters found to fit the data almost equally well assuming odd $Kp\Sigma$ parity. The polarization data were included in the fitting procedure, of course. The even $Kp\Sigma$ parity curve is not a true reflection of either odd parity curve because when the input polarization data were reversed in sign, the final parameterization was altered slightly. Since the data excluding the polarizations are very restrictive, the solutions were altered very little. Odd $Kp\Sigma$ parity is very strongly indicated.

C. Parameter Determination by the Computer

There were several reasons that justified the effort put into a computer analysis in addition to the hand analysis already published. The data upon which the first analysis was based were reanalyzed by use of the beam-averaging feature, which gives a better measure of the incident momenta. Furthermore, the hand analysis did not consider the momentum dependence of the s-wave amplitudes, and introduced p waves only at the end. Of course, the computer approach by its nature must also have a precise quantitative measure of the goodness of fit which the hand analysis lacked.

In order to program such a problem much more attention must be placed on unimportant background than is really justified. An example of this was the $\Lambda\pi^+\pi^-$ nonresonant background. Since this amounted to 1 mb or less, division into s and p waves does not significantly affect the hand-analysis estimate of the nonresonant amplitudes. Of course,

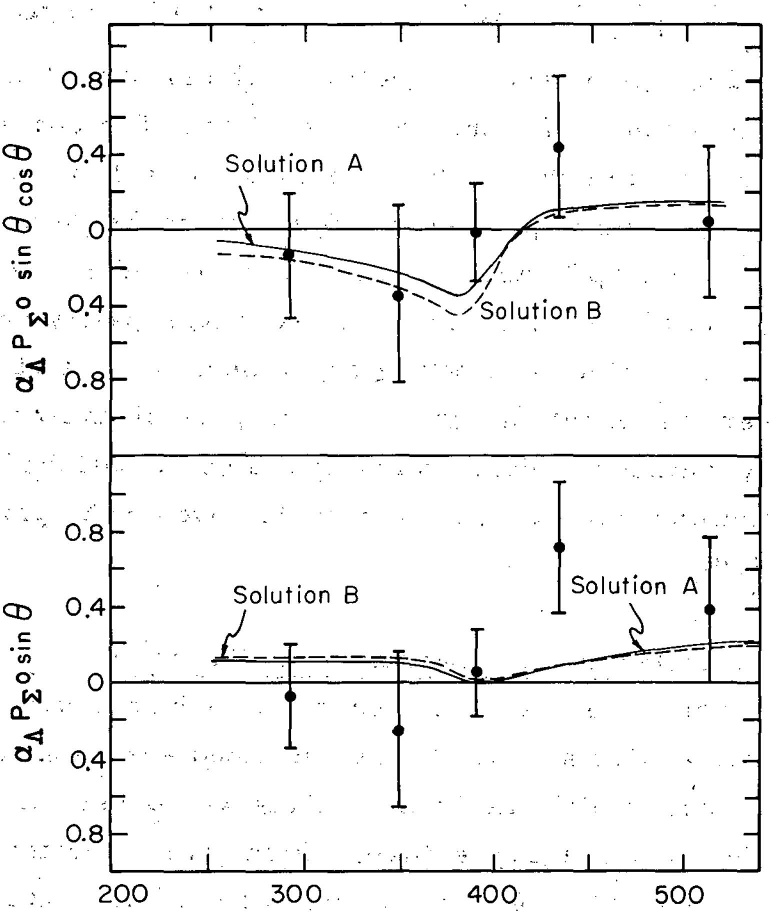

Fig. 37. Momentum dependence of the Σ^0 polarizations from the reaction $K^- + p \rightarrow \Sigma^0 + \pi^0$. The polarization is observed indirectly through the Λ polarization after the decay $\Sigma^0 \rightarrow \Lambda + \gamma$. The Λ^0 polarization is washed out by a factor of 3 and changes sign. The curves are solutions A and B of Section IV-C.

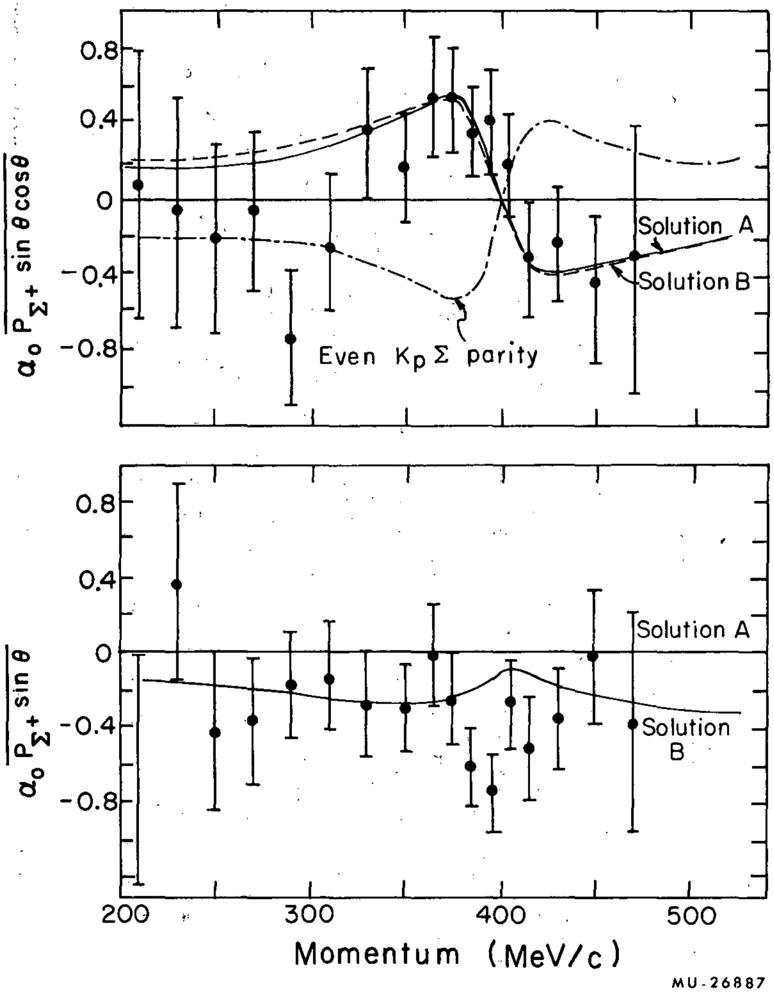

Fig. 38. Momentum dependence of the Σ^+ polarizations from the reaction $K^- + p \rightarrow \Sigma^+ + \pi^-$. The polarization is determined from the decay $\Sigma^+ \rightarrow p + \pi^0$. The decay asymmetry parameter (proton helicity) has been taken as $a_0 = -1.0$. The curves are solutions A and B of Section IV-C.

Table X. The generalized Minami ambiguities

Transition matrix M	Parity of M	Cross section $I^0(\theta)$	$I(\theta)\,\vec{P}(\theta)$	Example		
				Initial	→	Final
$(A + B\,\vec{\sigma}\cdot\hat{n})$	+	$I(\theta) + I(\theta)\vec{P}(\theta)\cdot\vec{P}_{in}$	$2\,\mathrm{Re}(A^*B)\,\hat{n}$	SP_1P_3	→	SP_1P_3
$\vec{\sigma}\cdot\vec{K}_{out}(A+B\vec{\sigma}\cdot\hat{n})\vec{\sigma}\cdot\vec{K}_{in}$	+	$I(\theta)+I(\theta)\vec{P}(\theta)\cdot\vec{P}_{in}$	$-2\,\mathrm{Re}(A^*B)\hat{n}$	P_1SD_3	→	P_1SD_3
$(A + B\vec{\sigma}\cdot\hat{n})\vec{\sigma}\cdot\vec{K}_{in}$	-	$I(\theta)-I(\theta)\vec{P}(\theta)\cdot\vec{P}_{in}$	$2\,\mathrm{Re}\,(A^*B)\,\hat{n}$	P_1SD_3	→	SP_1P_3
$\vec{\sigma}\cdot\vec{K}_{out}(A+B\vec{\sigma}\cdot\hat{n})$	-	$I(\theta)-I(\theta)\vec{P}(\theta)\cdot\vec{P}_{in}$	$-2\,\mathrm{Re}\,(A^*B)\hat{n}$	SP_1D_3	→	P_1SD_3

the computer had to consider this background quantitatively, which required several additional free parameters. The determination of these parameters was as difficult as the determination of the resonant width, resonant energy, and other important quantities.

Several simplifying assumptions were suggested by the data which reduced the number of parameters to be determined. The $\Lambda\pi$ channel was assumed to proceed entirely through the s_1 and P_{11} channels. (Throughout this discussion the subscripts indicate, as usual, I and 2J respectively.) The $\Lambda\pi\pi$ channel was assumed to proceed entirely through P_{01}, and P_{03} with no $I = 1$ contributions. With these assumptions 27 parameters were chosen to represent the model. These 27 parameters along with the final values for the two solutions found are listed in Table XI.

The first five of these parameters are those characteristic of the s-wave zero-effective-range approximation. This approximation consists of assuming that the complex scattering length $A_I = a_I + ib_I$ is energy-independent. The scattering and reaction amplitudes then have a well-defined momentum dependence as a function of the initial-state momentum only. These first five parameters are identical to those discussed by Dalitz and Tuan and measured by Humphrey and Ross.[6, 10, 14] Although Humphrey and Ross have already determined those parameters at lower energies, all five parameters were allowed to vary freely and were in no way constrained to approximate the low-energy values. There were two reasons for this procedure.

Following the notation of Dalitz and Tuan, the relation of the scattering length A_I to the K-matrix elements is

$$A_I \approx \alpha_{I',\ell} - \frac{\beta_{I,\ell}^{2}\,\gamma_{I,\ell}\,q^{4L+2}}{1+q^{4L+2}\,\gamma_{I,\ell}^{2}} + i\,\frac{\beta_{I,\ell}^{2}\,q^{2L+1}}{1+q^{4L+2}\,\gamma_{I,\ell}^{2}}$$

where $\alpha_{I,\ell}$, $\beta_{I,\ell}$, and $\gamma_{I,\ell}$ are the K-matrix elements for I-spin I and $\overline{K}N$ angular momentum ℓ, K and q are the initial- and final-state momenta, and L is the final-state angular momentum. For s waves q is 186 Mev/c at the K^-p threshold and increases to approx 265 Mev/c

Table XI. Parameters with the final values.

Parameter No.	Symbol	Meaning	Solution A	Solution B	Parameter No.	Symbol	Meaning	Solution A	Solution B
1	a_0	s-wave zero-effective range scattering length	-0.90±0.25 fermi	-0.96±0.14 fermi	15	Γ	Full-width	15.4±0.3 Mev	17.7±0.3 Mev
2	b_0	"	2.50±0.20 fermis	1.71±0.17 fermi	16	Γ_K	$\bar{K}$-n partial width	4.71±0.23 Mev	5.26±0.25 Mev
3	a_1	"	-0.03±0.06 fermi	0.14±0.05 fermi	17	Γ_Σ	Σ-π partial width	7.95±0.26 Mev	9.52±0.29 Mev
4	b_1	"	0.41±0.03 fermi	0.42±0.03 fermi	18	ϕ_{SD}	S_1-D relative phase	-1.77±0.06 radians	-1.96±0.07 radians
5	$\epsilon^{\Lambda\pi}_{S_1}$	$\left(\frac{\sigma(\Lambda\pi)}{\sigma(\Lambda\pi)+\sigma(\Sigma\pi)}\right)_{S_1}$	0.31±0.03	0.31±0.03	19	$\phi^{\Lambda\pi}_{SP_1}$	S_1-P_1 phase Λ-π channel	0.11±0.44 radian	0.10±0.43 radian
6	ϕ_S	S_0-S_1 Σ-π angle	-2.08±0.05 radians	-1.94±0.04 radians	20	$\epsilon^{\Sigma\pi}_{P_{01}}$	$\left(\frac{\sigma(\Sigma\pi)}{\sigma(\Sigma\pi)+\sigma(\Lambda\pi\pi)}\right)_{P_{01}}$	0.99±0.13	0.94±0.15
7	a_{01}	p_1-wave zero-effective range scattering length	-0.12±0.02 fermi^3	0.07±0.02 fermi^3	21	a_{03}	p_3-wave zero-effective range scattering length	-0.085±0.013 fermi^3	-0.006±0.011 fermi^3
8	b_{01}	"	0.015±0.005 fermi^3	0.012±0.004 fermi^3	22	b_{03}	"	0.004±0.001 fermi^3	0.0004±0.0003 fermi^3
9	a_{11}	"	-0.05±0.03 fermi^3	0.20±0.02 fermi^3	23	a_{13}	"	-0.016±0.012 fermi^3	0.066±0.011 fermi^3
10	b_{11}	"	0.016±0.003 fermi^3	0.008±0.003 fermi^3	24	b_{13}	"	0.0004±0.0004 fermi^3	0.00003±0.00010 fermi^3
11	$\epsilon^{\Lambda\pi}_{P_{11}}$	$\left(\frac{\sigma(\Lambda\pi)}{\sigma(\Lambda\ )+\sigma(\Sigma\pi)}\right)_{P_{11}}$	0.33±0.11	0.65±0.19	25	$\epsilon^{\Sigma\pi}_{P_{03}}$	$\left(\frac{\sigma(\Sigma\pi)}{\sigma(\Sigma\pi)+\sigma(\Lambda\pi\pi)}\right)_{P_{03}}$	0.97±0.23	0.79±0.67
12	$\phi_{P_{01}}$	P_{01} phase angle	3.11±0.12 radians	-2.63±0.12 radians	26	$\phi_{P_{03}}$	P_{03} phase angle	2.16±0.12 radians	2.92±0.40 radians
13	$\phi_{P_{11}}$	P_{11} phase angle	1.81±0.19 radians	0.80±0.26 radians	27	$\phi_{P_{13}}$	P_{13} phase angle	2.24±0.28 radians	1.49±2.11 radians
14	E_R	Resonant energy	1520.5±0.5 Mev	1520.5±0.5 Mev					

in the 400-Mev/c region. It would be mildly surprising if the Humphrey-Ross low-energy parameters were not altered in going this far up in energy. Since the magnitudes of β and γ are unknown although probably constant, it is impossible to predict the extrapolated values for a_I and b_I.

Most of the well-measured data points fall into the K^- momentum range from 350 to 450 Mev/c. If only these points are considered the approximation that a_I and b_I are constant should be valid, since q varies only from about 250 to 280 Mev/c. The A_I found in this way should then be related but not identical to the Humphrey-Ross values.

The second reason for not correlating the A_I to the Humphrey-Ross values was concerned with the hand-analysis indications of the sixth Humphrey-Ross parameter. The sixth s-wave parameter must relate the S_0 and S_1 relative phase in the $\Sigma\pi$ channel. For both the solutions found by the computer and also for the hand-analysis solution this phase approximates -110 deg. Such a value is not far from that predicted by the second solution of Humphrey and Ross. Both A_0 and A_1 as well as $\epsilon_S^{\Lambda\pi}$ approximate the values of the first solution, where the same phase is approx +90 deg. The s-wave zero-effective-range parameters seem to change sufficiently to prohibit correlating the high- and low-energy values.

The p-wave amplitudes were modeled after the s-wave amplitudes. For p waves, following Dalitz and Tuan, the initial-state momentum dependence is obtained by replacing K by K^3 in the expressions for the scattering and reaction amplitudes. For example, the expressions for the I = 0, $\overline{K}N$ channel S_0 and P_{01} amplitudes are

$$S_0(\overline{K}N) = \frac{2K(a_0+ib_0)}{(1+Kb_0)-i(Ka_0)} \; ; \; P_{01}(\overline{K}N) = \frac{2K^3\,(a_{01}+ib_{01})}{(1+K^3b_{01})-i(K^3a_{01})}$$

Appendix 2 contains the complete expressions for each of the elastic and reaction-channel amplitudes used in the computer program. In addition to the parameters corresponding to the s waves, three additional parameters are needed to specify the phases between the s-wave, the

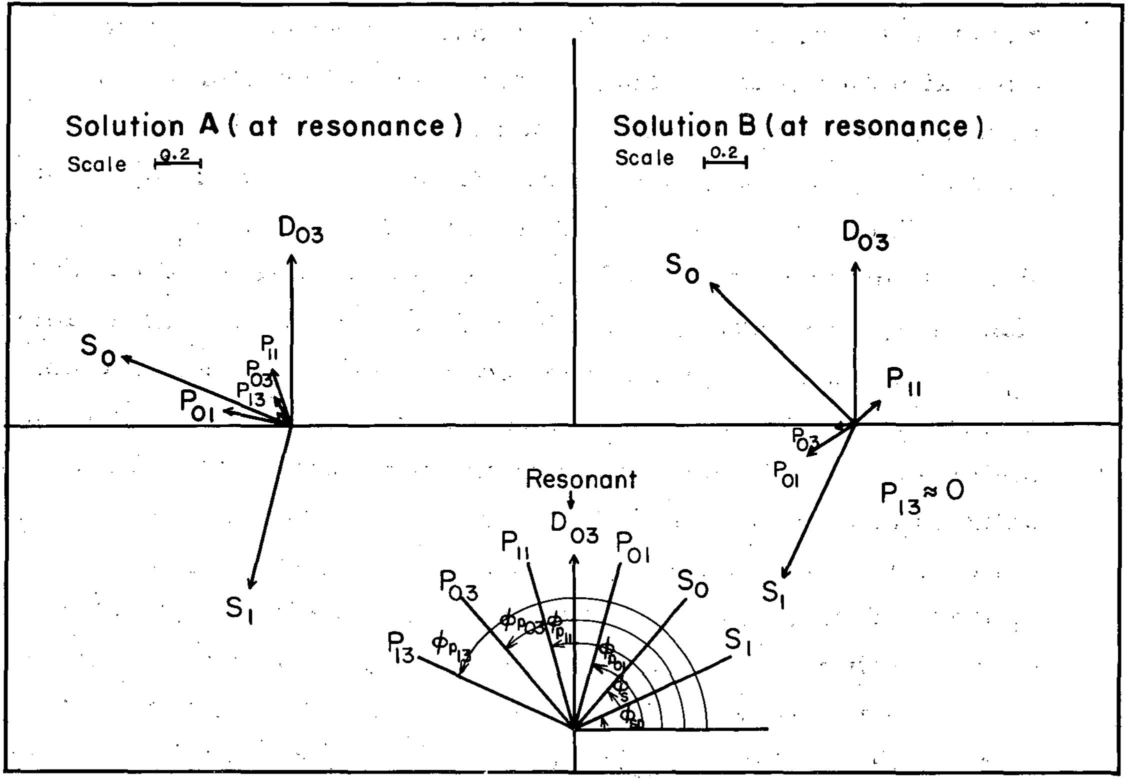

MUB-1139

Fig. 39. Graphic definition of the phases used in the computer fit to the data. Note all phases are defined relative to the resonant d-wave amplitude except for the S_0 amplitude.

$P_{1/2}$, and $P_{3/2}$ amplitudes. Actually, in the $\Sigma\pi$ channel each p-wave amplitude was related directly to the resonant d-wave phase. The s-wave amplitudes differed in that the s_1 phase was defined relative to the d-wave phase and the s_0 phase was defined relative to the s_1 phase. Figure 39 exhibits these phase definitions. Since there was no d wave in the $\Lambda\pi$ channel and only I = 1 amplitudes are involved, a single phase relating p_{11} and s_1 was used.

As in the hand analysis, the d waves were introduced through a Breit-Wigner type of amplitude. No nonresonant d waves were allowed in the I = 0 or I = 1 states. The parameters required in the Breit-Wigner expression are as listed in Table XI.

The angular distribution for each 10- or 20-Mev/c bin (some bins were larger if there were few events) was least-squares fitted to the series

$$\frac{d\sigma}{d\Omega} = A_1 + A_2 \cos\theta + A_3 \cos^2\theta .$$

The values of A_1, A_2, and A_3 along with the complete error matrix served as input for the computer. The cross section at the center of each bin was also read in. The polarization data for $\Sigma^+\pi^-$, $\Sigma^0\pi^0$, and $\Lambda\pi^0$ were introduced through coefficients A_4 and A_5:

$$\frac{d^2\sigma}{d\Omega d\cos\phi} = A_1 + A_2 \cos\theta + A_3\cos^2\theta + A_4\sin\theta\cos\phi + A_5\sin\theta\cos\theta\cos\phi.$$

The errors for A_4 and A_5 were uncorrelated with A_1, A_2, A_3.

As a measure of the goodness of fit a χ^2 function was constructed. The χ^2 function consisted of two parts. The A coefficients were first renormalized to the form

$$\frac{d^2\sigma}{d\Omega d\cos\phi} = \frac{\pi\lambda^2}{4\pi}\,[\,a_1 + a_2\cos\theta + a_3\cos^2\theta + a_4\sin\theta\cos\phi + a_5\sin\theta\cos\theta\cos\phi] ,$$

by using the calculated cross section in the program. The calculated and observed coefficients were compared and the χ^2 contribution was calculated by

$$\chi^2_{\text{shape}} = \sum_{ij} (a_i - a_i^M) M_{ij} (a_j - a_j^M),$$

where a_i^M and M are the measured coefficients and inverted error matrix. Since the integrals of the measured and calculated distributions are related, there were not five independent degress of freedom. The calculated and measured cross sections contributed the second part of the χ^2 function:

$$\chi^2_{\text{cross section}} = \left(\frac{\sigma_M - \sigma_{\text{calc}}}{\delta\sigma_M}\right)^2 .$$

With such a complex function of the unknown parameters an analytic solution was impossible. The method employed was similar to the methods used in phase-shift analyses. A random search in χ^2 space was carried out with the hope that the minimum χ^2 would be found if the search were continued long enough. The search procedure in the 27-dimensional space used the "method of ravines."[15] Briefly, this procedure involves the following steps. Pick a point A and compute the gradient. Move along the gradient direction a predetermined distance to point B. At B move in a direction perpendicular to the original gradient to point C. Using the value at point B, the derivatives at B, and the value at point C, calculate the distance to a minimum, assuming a parabolic dependence of χ^2 as a function of distance along this new direction. Move to this minimum and begin the process again.

This method tends to move rapidly along ravines toward minima rather than spending large amounts of time rattling back and forth between the ravine walls. The program continued to wander in χ^2 space even after a minimum was found. From any starting point the search moves toward the nearest minimum indicated by the gradient, past this minimum, up the far side of the χ^2 well, and--one hopes--into the neighboring well of another minimum. Given enough computer time, such a procedure should locate all minima at one run on the machine.

To begin the search, a point was chosen which was believed to correspond to the final s- and d-wave amplitudes as determined by the hand analysis. During this run several points were detected as possible minima based on rapid changes in the gradient direction. Each of these points was investigated, only to find that each eventually led to the same minimum (solution A). During these runs the search procedure seemed to have a great deal of trouble varying any of the phases by more than 90 deg in either direction. Accordingly, several new starting points were explored. In particular, the region for which both the $\Sigma\pi$ s_0-s_1 relative phase (parameter 6) and the s-d relative phase (parameter 18) were near $+90^{\circ}$ was explored. No new minimum was found.

A set of four starting points was also chosen in which the principal difference was the p-wave orientations. During these runs a second solution (solution B) was found, but each of the other starting points eventually arrived at either solution A or B. The exploration of these regions was greatly impeded by the constraint walls built into the program. These constraints required the set of parameters used at every step of the search be a physically accessible set. No cross sections were allowed to be negative, and no calculated polarization was allowed to exceed unity.

Table XI lists the values for both solution A and solution B. The errors for each of these parameters were determined by inverting the second derivative matrix of the χ^2 function. Let G be the complete error matrix. At the minimum,

$$\chi^2 = \chi^2_{\min} + \frac{1}{2} \sum_{ij} \left(\frac{\partial^2 \chi^2}{\partial a_i \partial a_j} \right)_{\min} \delta a_i \delta a_j + \text{higher derivative terms.}$$

By association we approximate

$$G_{ij} = (M^{-1})_{ij} \; ; \; M_{ij} = \frac{1}{2} \frac{\partial^2 \chi^2}{\partial a_i \partial a_j} .$$

D. Discussion

1. The Solutions

The two solutions A and B are very similar in their gross characteristics. The principal difference is found in the p-wave amplitudes, especially the $P_{1/2}$ amplitudes. The s and d parameters are nearly identical except that the B solution widths are slightly larger and b_0 is slightly smaller. Figures 28 through 32 show the predicted cross sections for both solutions. Figures 38 and 40 through 43 show the coefficients A_i of the angular distributions and the polarizations. The reader should remember that each angular distribution was normalized by the computer to the calculated cross section and not to the measured cross section. The data points shown are normalized to the measured cross sections. By use of the measured value, any error made in the magnitude of the cross section will be reflected in all three of the coefficients. There is actually better agreement between the curves and the data points than the figures show.

Table XII displays the division of the contributions to χ^2 channel by channel. The value of χ^2 for both solutions is higher than was desired. There are several possible reasons for this. The initial assumptions made to reduce the number of parameters required may have been too restrictive. The highest momentum point for the $\Lambda\pi^+\pi^-$ cross section contributed 8 to the χ^2 function out of a total of 13 for all the points in this channel. This data point is quite believable, indicating that the assumption that only the I = 0 p waves contribute to the $\Lambda\pi^+\pi^-$ background is not correct. If this point alone is eliminated the χ^2 values drop to approx 110, where 95 is now the expected value. This is less than 1 standard deviation.

The momentum dependences assumed for each channel may also be somewhat incorrect. Only the initial-state dependence was included. The final-state momentum changes by some 12%. When this change is cubed, as for the p-wave amplitudes, a reasonably large effect may arise in the interference terms, such as the $\cos\theta$ terms of the angular distributions.

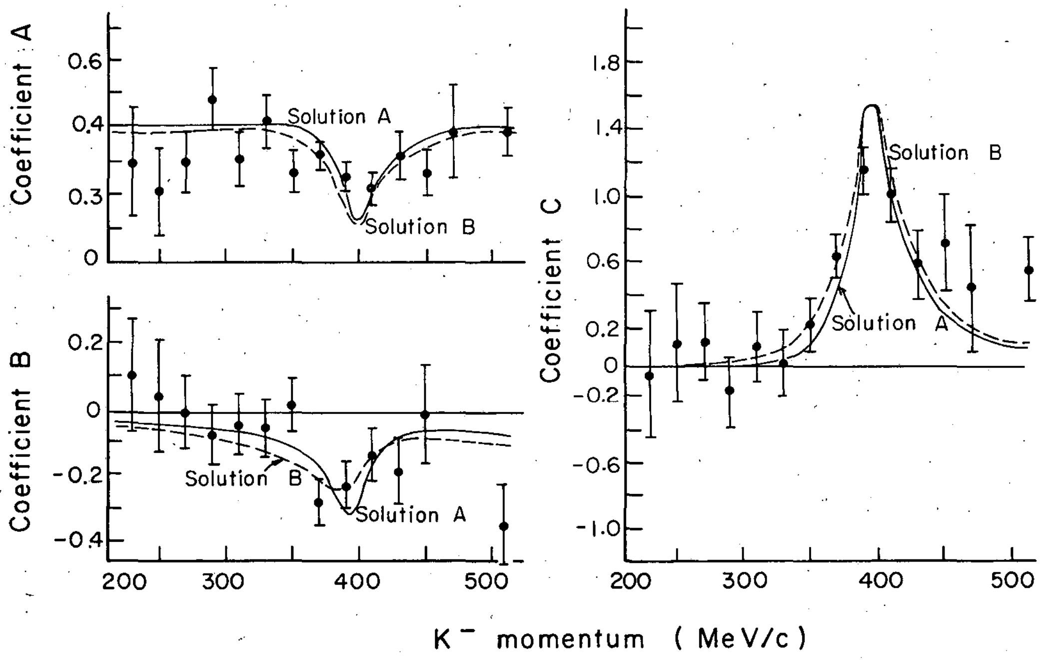

MU-26888

Fig. 40. Momentum dependence of the coefficients A, B, and C for the reaction $K^- + p \rightarrow \Sigma^+ + \pi^-$. $\theta_{K\pi}$ is the center-of-mass angle between incident K^- and outgoing π^-. A, B, and C are the coefficients in $\frac{d\sigma}{d\Omega} = \frac{\pi \lambda\!\!\!^{-2}}{4\pi} [A + B \cos\theta_{K\pi} + C \cos^2\theta_{K\pi}]$.

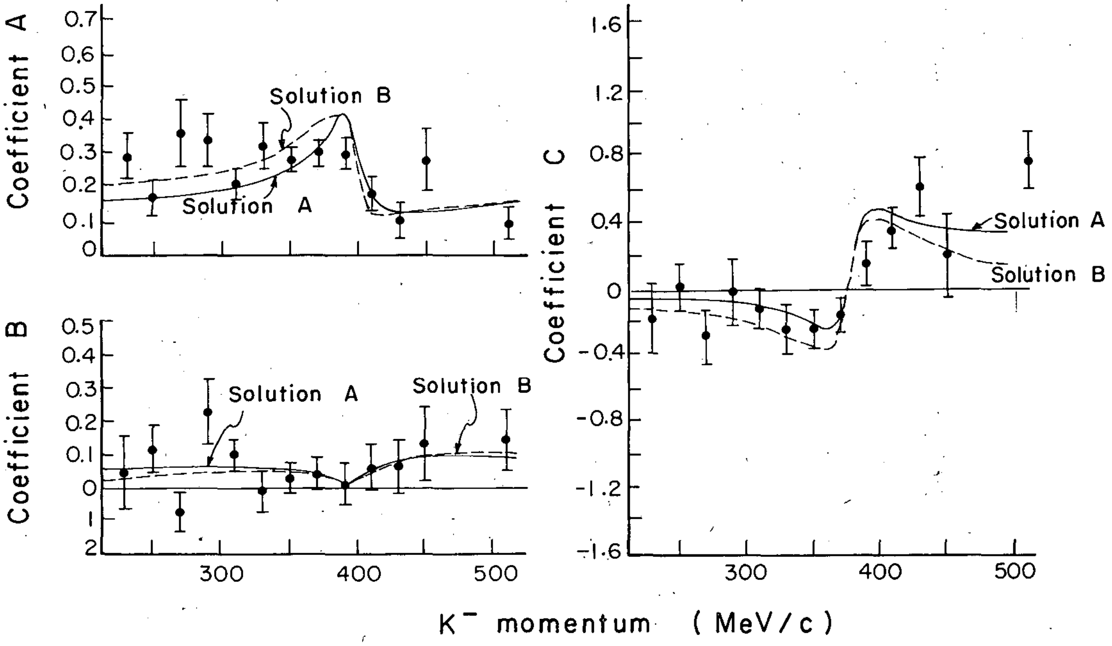

MU-26890

Fig. 41. Momentum dependence of the coefficients A, B, and C for the reaction $K^- + p \rightarrow \Sigma^- + \pi^+$. $\theta_{K\pi}$ is the center-of-mass angle between the incident K^- and outgoing π^+. A, B, and C are the coefficients in $\frac{d\sigma}{d\Omega} = \frac{\pi \lambda^2}{4\pi}$ $[A + B \cos \theta_{K\pi} + C \cos^2 \theta_{K\pi}]$.

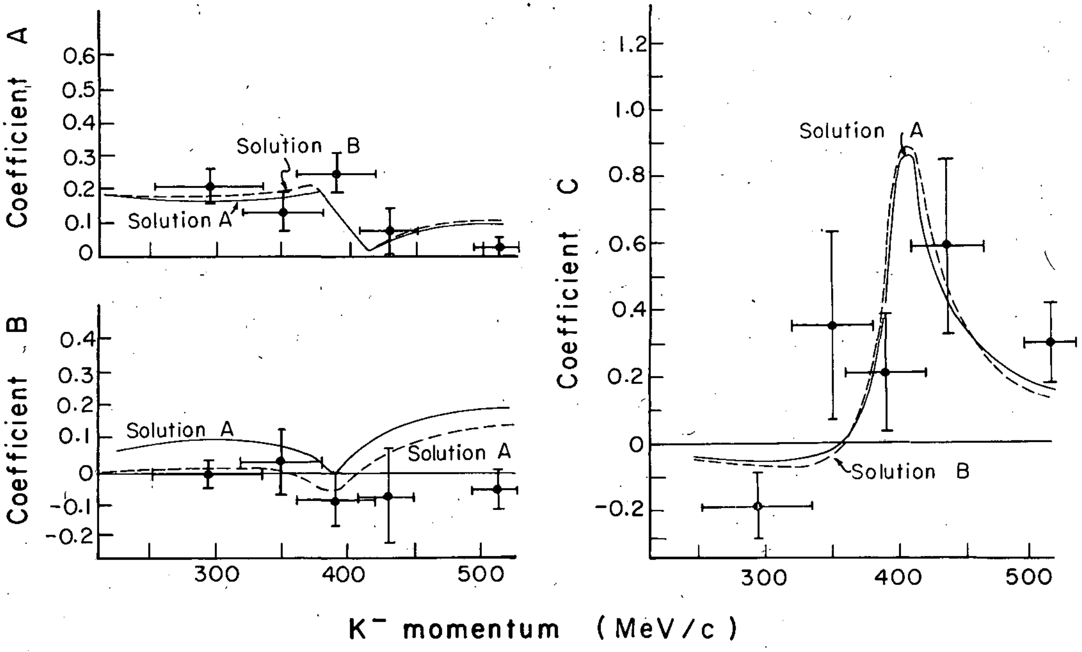

MU-26892

Fig. 42. Momentum dependence of the coefficients A, B, and C for the reaction $K^- + p \to \Sigma^0 + \pi^0$. $\theta_{K\pi}$ is the center-of-mass angle between the incident K^- and outgoing π^0. A, B, and C are the coefficients in $\frac{d\sigma}{d\Omega} = \frac{\pi \bar{\lambda}^2}{4\pi} [A + B \cos \theta_{K\pi} + C \cos^2 \theta_{K\pi}]$.

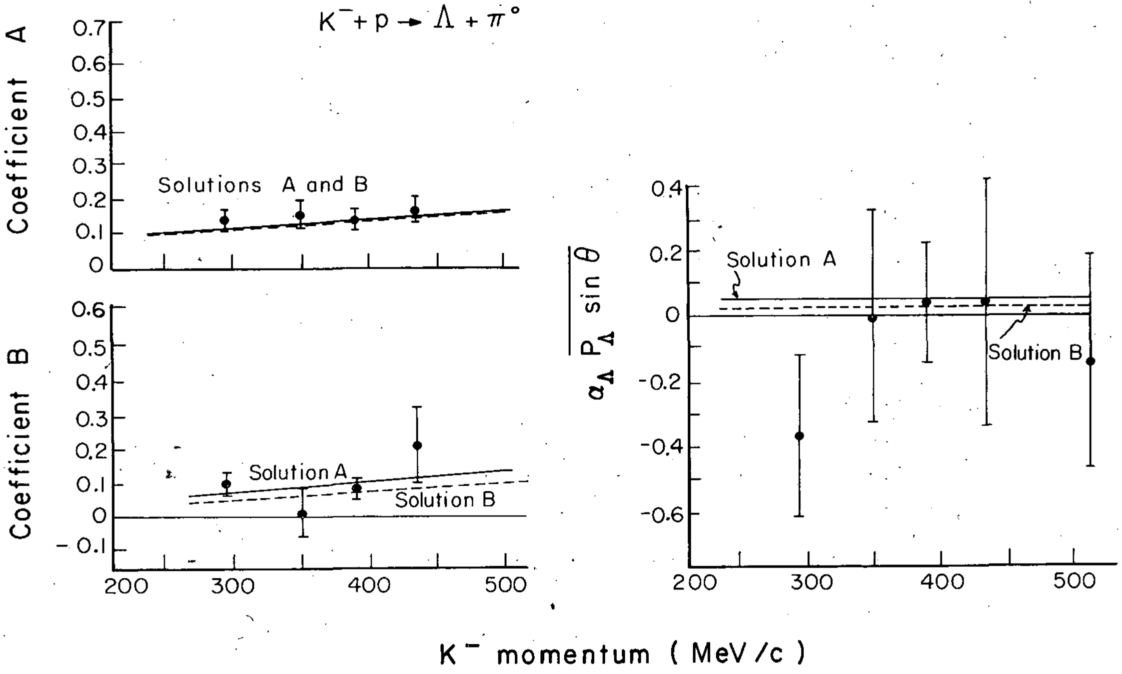

MU-27022

Fig. 43. Momentum dependence of the coefficients A and B and the polarization of the Λ in the reaction $K^- + p \rightarrow \Lambda + \pi^0$. Where $\frac{d\sigma}{d\Omega} = \frac{\pi\lambda\!\!\!^{-2}}{4\pi}$ [A + B cos $\theta_{K\pi}$]. $\theta_{K\pi}$ is the center-of-mass angle between the incident K^- and outgoing π^0. Since no $P_{3/2}$ or $D_{3/2}$ contributions were allowed by the $\Lambda\pi^0$ channel, there is no $\cos^2\theta_{K\pi}$ angular distribution coefficient or $\sin\theta\cos\theta$ polarization. The $\sin\theta\cos\theta$ polarization was experimentally consistent with zero.

Table XII

SOLUTION A					SOLUTION B				
Region	χ^2	Expected χ^2	Standard deviations	% level	Region	χ^2	Expected χ^2	Standard deviations	% level
Fitted region only 350 to 450 Mev/c	118.2	96	1.6	7	Fitted region only 350 to 450 Mev/c	117.8	96	1.6	7
Merged 293- to 434-Mev/c Runs (210 to 470 Mev/c)	313.7	196	6.0	<0.1	Merged 293- to 434-Mev/c Runs (210 to 470 Mev/c)	300.6	196	5.2	<0.1
Σ Polarization reversed (even KPΣ parity) 350 to 450 Mev/c	190.8	96	7.0	<0.1	Σ Polarization reversed (even KPΣ parity) 350 to 450 Mev/c	189.3	96	7.0	<0.1
Σ Polarization reversed, parameters readjusted to nearest minimum	188.1	96	7.0	<0.1	Σ Polarization reversed Parameters readjusted to nearest minimum	181.0	96	6.3	<0.1

Channel	χ^2shape	# Data points	χ^2cross sec.	# Data points	χ^2	# Data points	Channel	χ^2shape	# Data points	χ^2 cross sec.	# Data points	χ^2	# Data points
$K^- + p \rightarrow K^- + p$	7.9	12	7.7	6	15.6	18	$K^- p \rightarrow K^- p$	8.8	12	7.9	6	16.7	18
$K^- + p \rightarrow \bar{K}^0 + n$	4.7	5	9.0	12	13.7	17	$K^- p \rightarrow \bar{K}^0 n$	4.6	5	6.7	12	11.3	17
$K^- + p \rightarrow \Sigma^+ + \pi^-$	23.8	30	5.5	6	29.3	36	$K^- p \rightarrow \Sigma^+ \pi^-$	25.9	30	5.3	6	31.2	36
$K^- + p \rightarrow \Sigma^- + \pi^+$	8.1	12	11.2	6	19.3	18	$K^- p \rightarrow \Sigma^- \pi^+$	12.4	12	11.9	6	24.3	18
$K^- + p \rightarrow \Sigma^0 + \pi^0$	20.6	15	3.7	3	24.3	18	$K^- p \rightarrow \Sigma^0 \pi^0$	15.0	15	3.2	3	18.2	18
$K^- + p \rightarrow \Lambda + \pi^0$	1.6	3	1.1	3	2.7	6	$K^- p \rightarrow \Lambda \pi^0$	1.6	3	1.1	3	2.7	6
$K^- + p \rightarrow \Lambda \pi^+ + \pi^-$	0	0	13.2	10	13.2	10	$K^- p \rightarrow \Lambda \pi^+ \pi^-$	0	0	13.2	10	13.2	10

Also listed in Table XII are the χ^2 values obtained when the polarizations are reversed, corresponding to the even KpΣ parity assignment. After the polarization signs were reversed the program was allowed to reconverge to a new minimum. In neither case did the χ^2 values decrease significantly. The odd parity solutions are very strongly required.

Obviously, neither of the two odd parity solutions can be chosen as the correct one to the exclusion of the other on the basis of the data between 350 and 450 Mev/c. Both solutions A and B give almost identically good fits to these data. Both solutions were extrapolated to fit all the data between 210 and 513 Mev/c. Even after this extrapolation no preference for one solution seems warranted. Of course, in this extrapolation the final-state momentum dependence must become quite significant. Further analysis, using a wider momentum interval for fitting, is being carried out.

Finally, the similarity to the Humphrey-Ross solutions should be mentioned. Table XIII lists the corresponding s-wave parameters. The first five parameters of solutions A and B are very similar to solution 1 of Humphrey and Ross. The complete reversal in sign for the sixth parameter is quite puzzling.

The possibility that a completely different assignment of partial waves can be made seems to be very remote. Of course, there is always the possibility that some peculiar and unnatural behavior may be present or that some complex combination of J = 5/2 or higher angular momentum states is the correct solution. Other partial-wave possibilities with J = 3/2 have been painfully examined,[1] only to be discarded.

2. Yang Ambiguities

In addition to the Minami ambiguities which the preceding sections have "resolved" as $D_{3/2} \rightarrow D_{3/2}$ for the resonant channel, there are several other ambiguities or possible alternatives. One is a generalized Yang ambiguity which has been discussed by R. H. Capps in this particular context.[16] All angular distributions and polarizations are unchanged if the transformation $A \rightarrow A^*$, $B \rightarrow -B^*$ is applied to the transition operator

Table XIII. Comparison of the s-wave parameters with the Humphrey-Ross values.

Humphrey-Ross solutions			400-Mev/c Region Values	
Solution 1	Solution 2	Symbols	Solution A	Solution B
-0.22 ± 1.07	-0.59 ± .46	a_0	-0.90 ± 0.25	-0.96 ± 0.14
2.74 ± .31	0.96 ± .17	b_0	2.50 ± 0.20	1.71 ± 0.17
0.02 ± .33	1.20 ± .06	a_1	-0.03 ± 0.06	0.14 ± 0.05
0.38 ± .08	0.56 ± .15	b_1	0.41 ± 0.03	0.42 ± 0.03
0.40 ± .03	0.39 ± .02	$\epsilon_S^{\Lambda\pi}$	0.31 ± 0.03	0.31 ± 0.03
≈ 90	≈ -90	ϕ_S^a (deg)	-119 ± 3	-109 ± 2

[a] This angle was not actually used as the 6th parameter by Humphrey and Ross. The values shown are rough predicted extrapolations for this phase based on their solutions.

$M = A + B\ \vec{\sigma} \cdot \hat{n}$. In terms of the amplitudes discussed above such a transformation is

$$D_{3/2} \rightleftarrows \frac{1}{3}\left[D^*_{3/2} + 2S^*_{1/2}\right]$$

$$S_{1/2} \rightleftarrows \frac{1}{3}\left[4D^*_{3/2} - S^*_{1/2}\right]$$

$$P_{3/2} \rightleftarrows \frac{1}{3}\left[P^*_{3/2} + 2\,P^*_{1/2}\right]$$

$$P_{1/2} \rightleftarrows \frac{1}{3}\left[4P^*_{3/2} - P^*_{1/2}\right] .$$

The Yang solutions for this case would imply a resonance in both the $S_{1/2}$ and $D_{3/2}$ states. This solution would give identical angular distributions and polarizations at some momentum but would imply a different momentum dependence because of the different centrifugal barriers. The best handles for resolving this ambiguity are the interference terms with the p-wave amplitudes at energies surrounding the resonance. Since the p-wave amplitudes are small, it is very hard to measure any difference in the two solutions because the total effect is so small. No convincing argument based on the data has been found to resolve this ambiguity. However, simultaneous resonances in two angular momentum states are very unappealing.

3. The J = 5/2 Possibility

Since d waves have been accepted as the angular momentum state involved with J = 3/2, there is no reason to discriminate against d waves with J = 5/2 because of energy considerations. Furthermore, if the $K p \Sigma$ parity is odd the $K^- p \rightarrow \Sigma\pi$ is $D_{5/2} \rightarrow D_{5/2}$ and no F waves are required. If the resonant state were J = 5/2, however, $\cos^3\theta$ and $\cos^4\theta$ terms would be expected to show up in at least one of the angular distributions. None of the $\Sigma\pi$ distributions indicates any need for such terms. These distributions contain only a few hundred events each, however, and such terms might not express themselves forcefully enough to be detected. Indeed, the pure J = 5/2 angular distribution is $(1 - 2\cos^2\theta + 5\cos^4\theta)$, which is only slightly different from the pure J = 3/2 distribution $(1 + 3\cos^2\theta)$. This situation is worse than the actual case, since there is 100% certainty that more than one partial wave is present in significant amounts.

None of the elastic scattering distributions indicates any terms higher than $\cos^2\theta$ (see Table III). Although it is conceivable such terms are present, any justification would have to come from another source.

There is one additional handle which seems to rule out $J = 5/2$. This handle comes from the restrictions of unitarity. Perhaps the easiest way to see how this restriction applies is on the familiar bell-shaped curve relating the elastic and reaction cross sections for the resonant channel. Figure 44 shows two such curves for the $J = 3/2$ and $J = 5/2$ cases. At resonance the points actually on the curve apply.

Limits may be placed on both the elastic and reaction amplitudes from the data. These limits are

$$0.3 \leqslant \sigma_{\text{elastic}}/\pi\lambda\!\!\!^{-2} \leqslant 0.5,$$

$$0.3 \leqslant \sigma_{\text{reaction}}/\pi\lambda\!\!\!^{-2} \leqslant 0.9.$$

The shaded area represents those points that satisfy both of these restrictions. Only the $J = 3/2$ curve cuts through the allowed region. Within the statistical uncertainties, this argument seems more convincing than the absence of $\cos^3\theta$ or $\cos^4\theta$ terms in the angular distributions.

4. The Y_1^* Cusp Explanation

There has been some speculation that the 1520-Mev phenomena are not due to a resonance at all, but rather are cusp effects at the Y_1^* threshold. Whether or not the observed effects can be reproduced as a result of this new channel's opening up is of no concern here. Such an explanation seems to be doubtful for two reasons. First, the width associated with the 1520-Mev bumps is only 15 Mev, whereas the Y_1^* width is closer to 20 Mev. It is very unlikely that the threshold for producing a resonance of 20 Mev width would produce the much narrower 1520-Mev phenomena of only 15 Mev width.

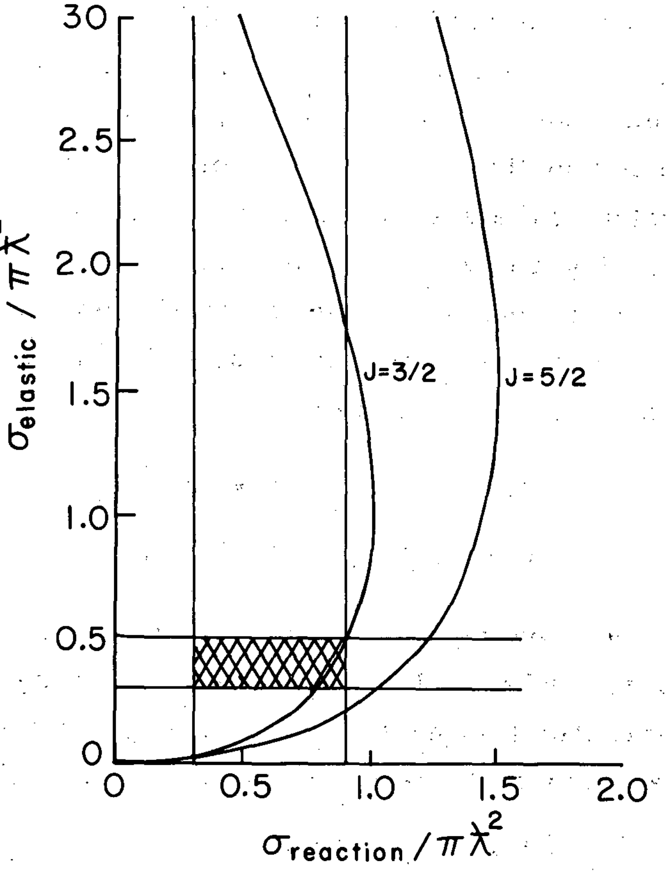

MU-27010

Fig. 44. Relation of $\sigma_{reaction}$ and $\sigma_{elastic}$ for J = 3/2 and J = 5/2 resonant spin assignments. At resonance the cross sections are related by the points actually on the curves.

Secondly, the 1520-Mev resonance has also appeared in other reactions at different energies. One such reaction is the $\Sigma\pi\pi$ production by K^- mesons on protons at 850 Mev/c.[17] A group of these events, reasonably interpreted as $\Sigma\pi$ decays of Y_1^*, led to an anomalously high branching ratio for such decays. However, the 1520-Mev resonance allows these events to be reinterpreted, eliminating all inconsistencies.

There are other indications of the 1520-Mev resonance as yet unpublished. One such example is the reaction $K^- + p \rightarrow K^- + p + \pi^0$, in which the K^- and p effective mass peaks near 1520 Mev.[18] These data, further establishing the 1520-Mev phenomena as resonance rather than cusp, should be published shortly.

V. ACKNOWLEDGMENTS

In any experiment involving use of such tools as the Bevatron, Alvarez 15-inch hydrogen bubble chamber, and IBM 7090, many cooperative efforts are required. It is the pleasure that I acknowledge the support of Professor Luis W. Alvarez and the invaluable guidance of Professor Robert D. Tripp. I would also like to thank Dr. Joseph J. Murray, who supervised the design and construction of the beam. I am greatly indebted to Dr. Massimiliano Ferro-Luzzi, who performed the analysis on some of the data discussed, and to Dr. William E. Humphrey, who wrote the computer search routine.

There are many scanners and technicians who deserve thanks, especially Mr. Michael Kelley and Mr. Roger Griswold.

Finally, I would like to thank Dr. Ronald Ross, not only for many helpful discussions concerning this experiment, but also for his help throughout my graduate training.

This work was done under the auspices of the U. S. Atomic Energy Commission.

APPENDICES

I. Distribution of χ^2 and the "Pull" Quantities for Event Reconstruction

Each event reconstructed by the IBM 7090 program PACKAGE was subjected to the constraints of momentum and energy conservation. A χ^2 function measuring the goodness of fit to these constraints was minimized in each case. The assignment of errors to each of the measured quantities is a nontrivial task with some arbitrariness involved. The variables chosen to represent the measurements in the fitting procedure were

ϕ_i = azimuth angle for the ith track,
S_i = tan λ_i or the tangent of the dip angle,
K_i = "projected curvature" of the ith track.

In this appendix the distribution of the χ^2 function and the distribution of the "pull" quantities on the above variables will be examined.

To study the χ^2 distribution a large group of elastic scatterings was chosen randomly. Since usually all tracks are measurable in such events, the constraints of momentum and energy conservation left the "fit" four times overdetermined. The χ^2 for such a case should have a mean of 4. Figure 45 shows the observed χ^2 distribution and a theoretical curve normalized to the correct number of events for four degrees of freedom (solid curve). The observed distribution is seen to be too spread out. The dashed curve corresponds to the case in which the error assignments are about 20% underestimated. This fit is quite good, indicating that no serious distortions exist but only a misassignment of error magnitudes.

As a measure of the contribution to the χ^2 discrepancy by each measured variable, the "pull" quantities $P_i(x)$ were examined. The $P_i(x)$ are defined by

$$P_i(x^*) = x_i^* - x_i^{\text{meas}} / \sqrt{\langle (x_i^* - x_i^{\text{meas}})^2 \rangle},$$

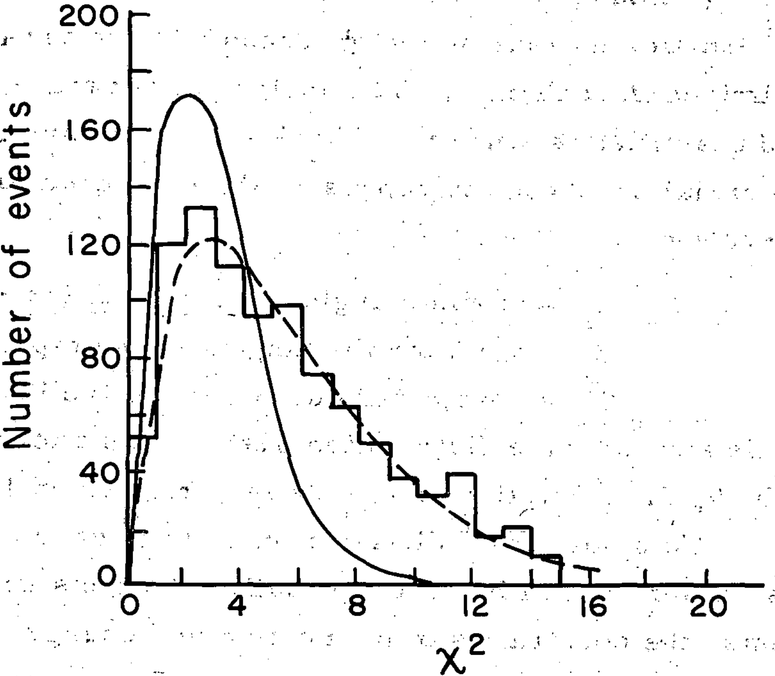

MU-27003

Fig. 45. Distribution of the χ^2 function for 948 elastic scatterings.

where x_i^* is the adjusted value of a variable corresponding to the measured value x_i^{meas}. The pull quantities should have a mean value of 0 and a standard deviation of 1 if no systematic errors are made and if the measurement errors are correctly assigned. These quantities are discussed in detail in connection with the predecessor program to PACKAGE called KICK.[19] Figures 46 through 48 display the distributions of the pull quantities corresponding to ϕ, S, and K for the incident and scattered K^- tracks and the recoil protons. The curves shown are normal distributions with the standard deviations approximating those of the histograms. In each case the mean is slightly shifted, but in no case is this shift alarmingly large. The widths of all of the distributions indicate a slight underestimate of the measurement errors by about 20%. On the basis of these curves it would be possible to readjust the error assignments for each measured variable. However, since none of the curves indicates any serious trouble with the existing assignment, such a procedure would probably gain nothing of real value. At no point in the experiment was a major dependence placed on the proper distribution of χ^2, only on relative values. The errors introduced by deviations in the distribution of the χ^2 function and the pull quantities were believed to be negligible compared with the statistical uncertainties inherent in the data.

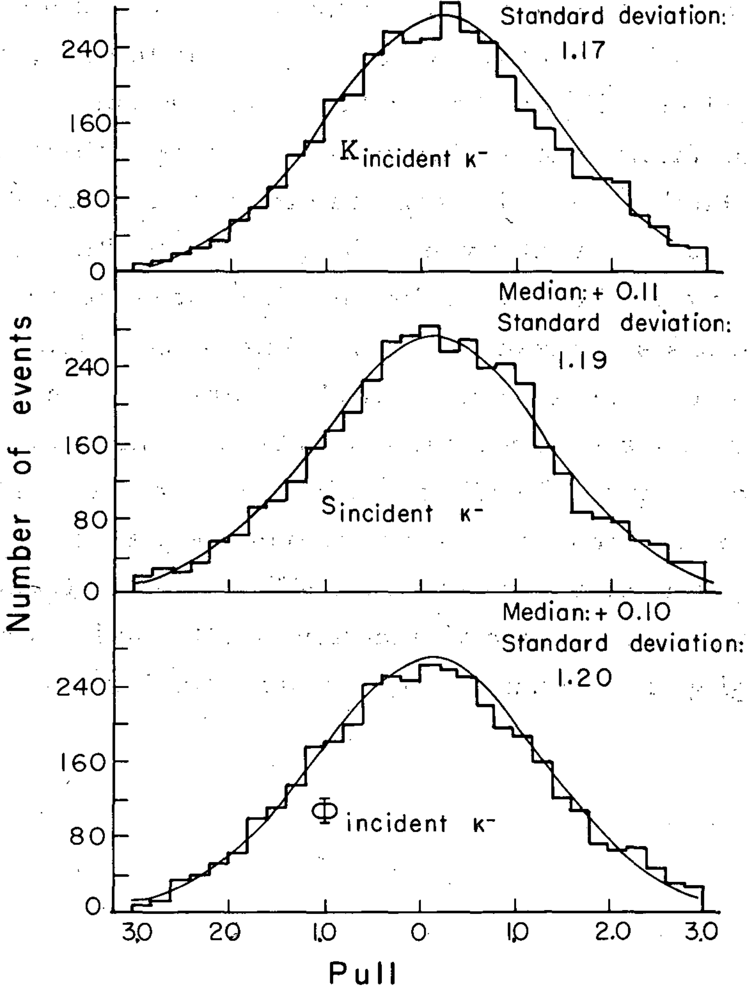

Fig. 46. Pull quantities for the incident K^- tracks in elastic scattering.

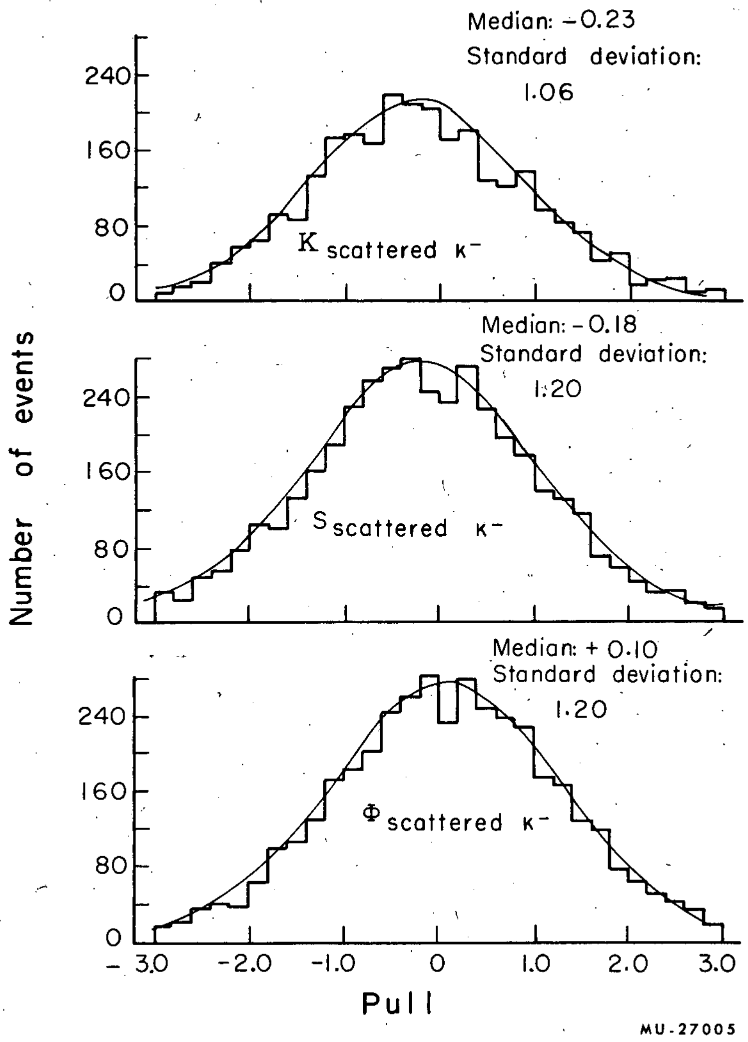

Fig. 47. Pull quantities for the scattered K^- tracks in elastic scattering.

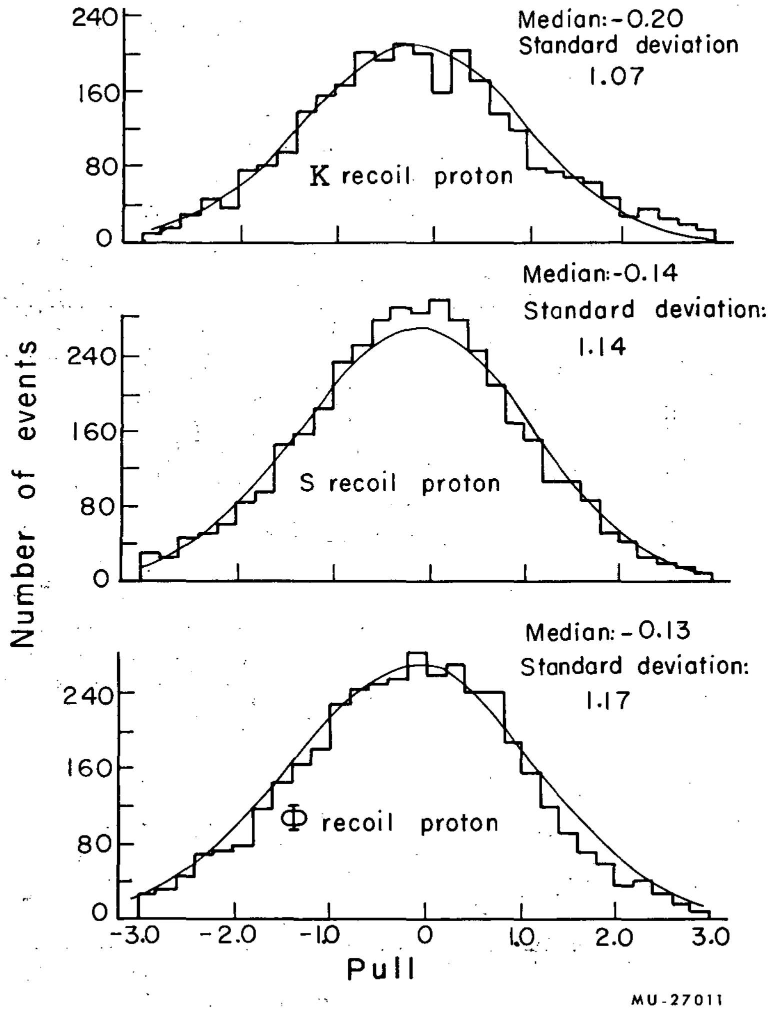

Fig. 48. Pull quantities for the recoil protons in elastic scattering.

$$|S_1^{\Lambda\pi}|^2 = \frac{4Kb_1\,\epsilon_S^{\Lambda\pi}}{(1+Kb_1)^2+(Ka_1)^2} \; ; \quad |P_{1,1}^{\Lambda\pi}|^2 = \frac{4K^3b_{1,1}\,\epsilon_{P_{1,1}}^{\Lambda\pi}}{(1+K^3b_{1,1})^2+(K^3a_{1,1})^2};$$

$$|P_{1,3}^{\Lambda\pi}|^2 = 0 \; ; \quad |S_I^{\Lambda\pi\pi}|^2 = 0 \; ; \quad |P_{1,2J}^{\Lambda\pi\pi}|^2 = 0 \; ;$$

$$|P_{0,2J}^{\Lambda\pi\pi}|^2 = \frac{4K^3b_{0,2J}(1-\epsilon_{P_{0,2J}}^{\Sigma\pi})}{(1+K^3b_{0,2J})^2+(K^3a_{0,2J})^2} \; ; \quad |D_{0,3}^{\Lambda\pi\pi}|^2 = \frac{\Gamma_K(\Gamma-\Gamma_K-\Gamma_\Sigma)}{(E_R-E)^2+(\frac{\Gamma}{2})^2} .$$

Once these amplitudes were calculated the proper Clebsch-Gordan coefficients were used to calculate the complete s, p_1, p_3, and d_3 amplitudes. For example:

$$\begin{aligned}
S_{K^-p} &= \frac{1}{2}(S_0^{\bar{K}N} + S_1^{\bar{K}N}), \\
S_{\bar{K}^0N} &= \frac{1}{2}(S_0^{\bar{K}N} - S_1^{\bar{K}N}), \\
S_{\Sigma^+\pi^-} &= \frac{1}{\sqrt{2}}\left(\frac{1}{\sqrt{3}}\,S_0^{\Sigma\pi} - \frac{1}{\sqrt{2}}\,S_1^{\Sigma\pi}\right), \\
S_{\Sigma^-\pi^+} &= \frac{1}{\sqrt{2}}\left(\frac{1}{\sqrt{3}}\,S_0^{\Sigma\pi} + \frac{1}{\sqrt{2}}\,S_1^{\Sigma\pi}\right), \\
S_{\Sigma^0\pi^0} &= \frac{1}{\sqrt{2}}\left(\frac{1}{\sqrt{3}}\,S_0^{\Sigma\pi}\right), \\
S_{\Lambda\pi^+\pi^-} &= \frac{1}{\sqrt{2}}\left(\sqrt{\frac{2}{3}}\,S_0^{\Lambda\pi\pi}\right), \\
S_{\Lambda\pi^0} &= \frac{1}{\sqrt{2}}\left(S_1^{\Lambda\pi}\right).
\end{aligned}$$

II. Equations for GENERAL DUKE

The equations used by the computer program called GENERAL DUKE which determined the parameters of solutions A and B were as follows. Denote the amplitudes by the usual symbol s, p, or d subscripted by I and 2 J respectively. The parameters used to construct these amplitudes were those of Table XI.

For the $\overline{K}N$ channel the amplitudes were

$$S_I^{\overline{K}N} = \frac{2K(a_I + ib_I)}{(1+Kb_I) - i(Ka_I)} \quad ; \quad P_{I,\,2J}^{\overline{K}N} = \frac{2K^3(a_{I,\,2J} + ib_{I,\,2J})}{(1+K^3 b_{I,\,2J}) - i(Ka_{I,\,2J})}$$

$$D_{03}^{\overline{K}N} = \frac{\Gamma_K}{E_R - E - i\,\frac{\Gamma}{2}} \quad ; \quad D_{13}^{\overline{K}N} = 0$$

For the absorption channels the squares of the amplitudes were calculated by using

$$|S_0^{\Sigma\pi}|^2 = \frac{4Kb_0}{(1+Kb_0)^2 + (Ka_0)^2} \; ; \; |S_1^{\Sigma\pi}|^2 = \frac{4Kb_1(1-\epsilon_S^{\Lambda\pi})}{(1+Kb_1)^2 + (Ka_1)^2} \; ;$$

$$|P_{0,\,2J}^{\Sigma\pi}|^2 = \frac{4K^3 b_{0,\,2J}\, \epsilon_{P_{0,\,2J}}^{\Sigma\pi}}{(1+K^3 b_{0,\,2J})^2 + (K^3 a_{0,\,2J})^2} \; ; \; |P_{1,2J}^{\Sigma\pi}|^2 = \frac{4K^3 b_{1,2J}(1-\epsilon_{P_{1,\,2J}}^{\Lambda\pi})}{(1+K^3 b_{1,\,2J})^2 + (K^3 a_{1,2J})^2} \; ;$$

$$|D_{0,\,3}^{\Sigma\pi}|^2 = \frac{\Gamma_K \Gamma_\Sigma}{(E_R - E)^2 + (\frac{\Gamma}{2})^2} \; ; \; |D_{1,\,3}^{\Sigma\pi}|^2 = 0 \; ;$$

The coefficients A_1, A_2, A_3, A_4, and A_5 then used these amplitudes:

$$A_1 = |S - D_3|^2 + |P_1 - P_3|^2$$

$$A_2 = 2\mathrm{Re}\,[(S+2D_3)^* (P_1-P_3) + 3(S-D_3)^* P_3]$$

$$A_3 = |S+2D_3|^2 - |S-D_3|^2 + |P_1+2P_3|^2 - |P_1-P_3|^2$$

$$A_4 = 2\mathrm{Im}\,[(P_1-P_3)^* (S-D_3)]$$

$$A_5 = 6\mathrm{Im}\,[D_3^* S - P_3^* P_1]$$

The real and imaginary parts of s, p_1, p_3, and d_3 in the absorption channels were obtained by using the phases described in the text (Section IV-C).

REFERENCES

1. L. W. Alvarez, in Proceedings of Ninth International Annual Conference on High-Energy Physics, Kiev, 1959 [Academy of Sciences (UPAP), Moscow, Russia, 1960], and The Interactions of Strange Particles, Lawrence Radiation Laboratory Report UCRL-9354, Aug. 1960 (unpublished); also P. Nordin, Phys. Rev. 123, 2168 (1961).
2. Pierre Bastien, Orin Dahl, Joe Murray, Mason Watson, R. G. Ammar, and Peter Schlein, in Proceedings of the International Conference in Instrumentation for High-Energy Physics at Berkeley, 1960, (Interscience Publishers, Inc., New York, 1961), pp. 299-301.
3. Joseph J. Murray, in Proceedings of the International Conference in Instrumentation for High-Energy Physics at Berkeley, 1960 (Interscience Publishers, Inc., New York, 1961), pp. 25-33.
4. See, for example, A. H. Rosenfeld, in Proceedings of the International Conference on High-Energy Accelerators and Instrumentation, CERN, Geneva, 1959, pp. 533-541. This describes the separate PANG-KICK system. For more details see Reference Manual for KICK IBM Program, Lawrence Radiation Laboratory Report UCRL-9099, May, 1961.
5. Walter H. Barkas and Arthur H. Rosenfeld, Data for Elementary Particle Physics, Lawrence Radiation Laboratory Report UCRL-8030, October 1, 1961, and M. Gell-Mann and A. H. Rosenfeld, Ann. Rev. Nuclear Sci. 1, 407 (1957).
6. W. E. Humphrey, Hyperon Interactions By K^- Mesons Incident on Hydrogen, Lawrence Radiation Laboratory Report UCRL-9752, June 1961 (unpublished).
7. E. F. Beall, B. Cork, D. Keefe, P. G. Murphy, and W. A. Wenzel, Phys. Rev. Letters 1, 285 (1961).
8. Janos Kirz, Joseph Swartz, and Robert D. Tripp (Lawrence Radiation Laboratory), private communication. The analysis of the data showing this effect is not yet completed.

9. J. Peter Berge (Lawrence Radiation Laboratory), unpublished work to be reported in Ph. D. Thesis.

10. Ronald R. Ross, Elastic and Charge Exchange Scattering of K^- Mesons in Hydrogen, Lawrence Radiation Laboratory Report UCRL-9749, June 1961 (unpublished).

11. Massimiliano Ferro-Luzzi, Robert D. Tripp, and Mason B. Watson, Phys. Rev. Letters 8, 28 (1962).

12. Robert D. Tripp, Mason B. Watson, and Massimiliano Ferro-Luzzi, Phys. Rev. Letters 8, 175 (1962).

13. E. P. Wigner, Phys. Rev. 98, 145 (1955). Wigner has proven the theorem for the one-channel case. In the multichannel generalization the theorem applies to the eigenphases.

14. R. H. Dalitz and S. F. Tuan, Ann. Phys. 3, 307 (1960).

15. I am unaware of any published report of this method. I am very grateful to Dr. Henry M. Stapp for a note on the general method and to William E. Humphrey for many discussions.

16. R. H. Capps, Resonance Interference Method for Determining $K\Sigma N$ Parity, (to be published in the Physical Review, May, 1962).

17. P. Bastien, M. Ferro-Luzzi, and A. H. Rosenfeld, Phys. Rev. Letters 6, 702 (1961).

18. Pierre L. Bastien (Lawrence Radiation Laboratory), private communication.

19. J. P. Berge, F. T. Solmitz, and H. D. Taft, Rev. Sci. Instr. 32, 538 (1961).